Doctoral Dissertation

Exoplanet Search toward the Inner Bulge of the Milky Way via Gravitational Microlensing

重力マイクロレンズ法を用いた 天の川銀河中心領域における 太陽系外惑星探査

Iona Kondo

Department of Earth and Space Science,
Graduate School of Science,
Osaka University

Supervisor: Professor Takahiro Sumi

February 2023

Abstract

To date, more than 5,200 exoplanets have been discovered, most of which have distances and masses different from those of the planets in our solar system. To understand the diversity of planetary systems, it is necessary to elucidate the formation and evolution processes of planetary systems. In addition, almost all of the exoplanets discovered are high-mass planets with orbits close to the host star. On the other hand, the microlensing method can discover planets far from the host star. However, the number of planets detected by the microlensing method is only ~ 140 because the microlensing phenomenon is probabilistic.

Suzuki et al. (2016) conducted the most comprehensive systematic statistical analysis and used 29 planets detected by the microlensing method. They found that planets with the Neptune mass ratio are likely to be common beyond the snow line for the first time. However, there is still a large degree of uncertainty in the location of the break (or peak) in the planet mass-ratio distribution and the slope of low mass ratio distribution owing to the lack of low-mass planets in their analysis.

Therefore, in this study, the following two studies were conducted to increase the number of planet samples including low-mass planets for future statistical analysis by the microlensing planets.

First, I report the analysis of the microlensing event OGLE-2018-BLG-1185, which was simultaneously observed from the ground telescopes and the *Spitzer* space telescope. The ground-based light-curve modeling shows that the finite source effects are detected clearly and that the planet-host mass ratio is a very small value, $q \sim 6.9 \times 10^{-5}$. Although the observed signals were small by *Spitzer*, I could obtain space parallax likelihood distribution, which has the potential to constrain the lens mass and distance. So I conducted a Bayesian analysis with and without the space parallax constraint by *Spitzer* to estimate the probability distribution of the lens properties. As the result of the Bayesian analysis with only ground-based constraint, the lens system is likely a super-earth with a mass of $m_p \sim 8.4 M_\oplus$ orbiting a late M-dwarf with a mass of $M_{\rm host} \sim 0.37 M_\odot$. On the other hand, the Bayesian analysis with space parallax constraint by *Spitzer* shows that the lens system is likely a super-earth with a mass of $m_p \sim 2.1 M_\oplus$ orbiting a low-mass star with a mass of $M_{\rm host} \sim 0.09 M_\odot$. Future high-resolution imaging observations with *Hubble Space Telescope* or Extremely Large Telescope could distinguish between these two scenarios and help reveal the planetary system properties in more detail.

Second, I present the results of our estimation of planet yields and the optimal survey strategy by a new near-infrared telescope. In 2023, the PRime-focus Infrared Microlensing Experiment (PRIME) will start a near-infrared (NIR) microlensing survey toward the Galactic Center, which cannot be seen by conventional visible observations due to high dust extinction. The major goals of the PRIME microlensing survey are to measure the microlensing event rate in the inner

Galactic bulge to help design the observing strategy for the exoplanet microlensing survey by the *Nancy Grace Roman Space Telescope* and to make a first statistical measurement of exoplanet demographics in the central bulge fields where optical observations are challenging owing to the high extinction in these fields. Here I conduct a simulation of the PRIME microlensing survey to estimate its planet yields and determine the optimal survey strategy, using a Galactic model optimized for the inner Galactic bulge. To maximize the number of planet detections and the range of planet mass, I compare the planet yields among four observation strategies. I predict that PRIME will detect planetary signals for $42 - 52$ planets ($1 - 2$ planets with $M_p \leq 1M_\oplus$, $22 - 25$ planets with mass $1M_\oplus < M_p \leq 100M_\oplus$, $19 - 25$ planets $100M_\oplus < M_p \leq 10000M_\oplus$), per year depending on the chosen observation strategy. Besides, the spatially uniform survey not only allowed us to detect more planetary signals than that detected by the conventional optical survey, including low-mass planets but also to measure event rates over a wide range toward the Galactic inner bulge.

The first study found very low mass ratio planets and is an important sample for measuring the mass ratio function of planets on the low mass side in future statistical analyses. The second study was able to propose observational strategies that would allow the discovery of more than 10 times as many planets as conventional visible light observations, including the discovery of lower-mass planets. Both studies are expected to contribute not only to future microlensing statistical analysis, but also to future microlensing surveys with the *Roman* by understanding how to analyze space parallax and how to consider systematic errors on it, and by modifying the Galactic models.

List of Contents

List of Figures

List of Tables

Chapter 1

Introduction

1.1 Exoplanets

More than 5,200[1] exoplanets have been discovered since the first discovery of an exoplanet orbiting a main-sequence star in 1995 (Mayor & Queloz, 1995), including various planetary systems, such as hot Jupiters and super-Earths. Many of the planets discovered had properties, such as mass, radius, and semi-major axis, very different from those of the planets in our solar system. Figure 1.1 shows the distribution of the detected planetary systems. To explain the diversity of these planetary systems, it is necessary to understand their formation and evolutionary processes. Efforts have been made to understand the whole landscape of planets by comparing the distribution of planets discovered by various methods with different planetary sensitivities to a variety of planet formation and evolution theories. By achieving the above goals, we will be able to answer questions such as how many Earth-like planets exist, whether there is life elsewhere, and so on.

1.1.1 Detection Method

Almost all exoplanets have been detected via the radial velocity and transit methods, which are most sensitive to massive planets in close orbits. Here I review the characteristics of five major detection methods: Astrometry, Radial Velocity, Transit, Direct Imaging, and Microlensing. Each method has a different sensitivity to planets with masses and semi-major axes and is complementary to other methods.

Radial Velocity

Since the first exoplanet, 51 Pegasi b, hosted by a Sun-like star was discovered via the radial velocity measurement in 1995 (Mayor & Queloz, 1995), more than one thousand planets have been discovered by the radial velocity method. A star with a planet orbits in an elliptical orbit with its barycenter (common center of mass)

[1] as of 2022 December 19 from http://exoplanetarchive.ipac.caltech.edu

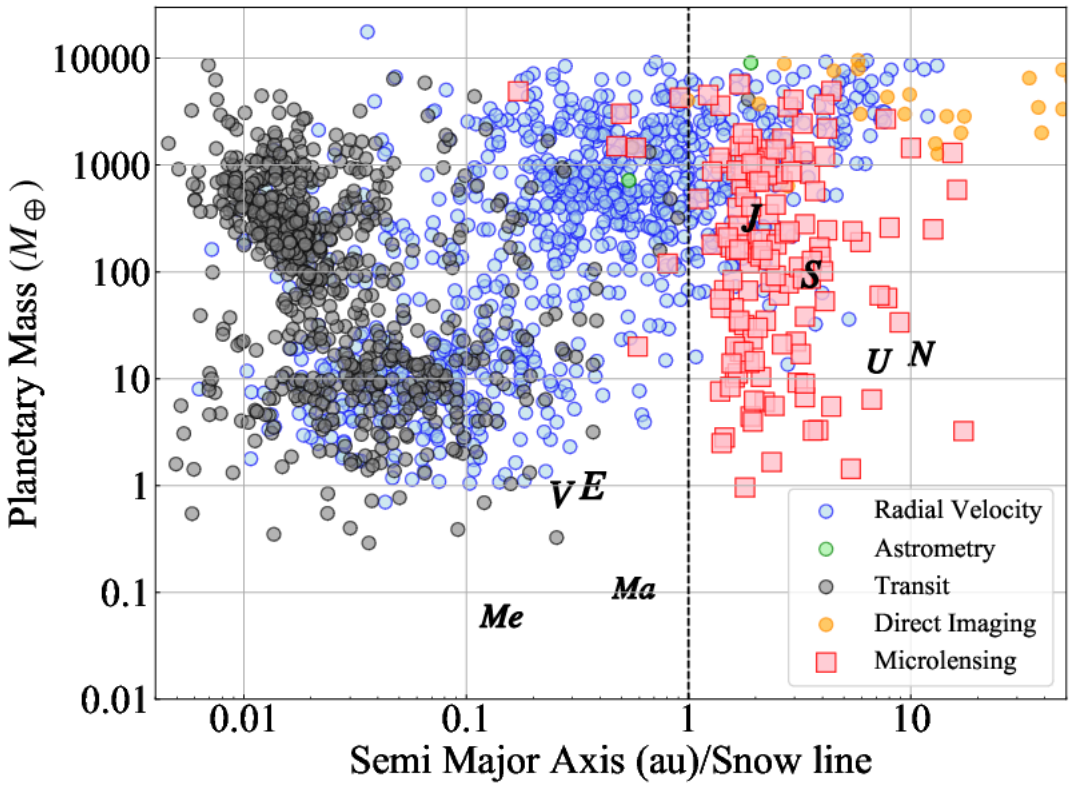

Figure 1.1: The distribution of detected planetary systems from https://exoplanetarchive.ipac.caltech.edu as of 2022 December 19. The green, blue, black, yellow, and red show planets discovered by astrometry, radial velocity, transit, direct imaging, and microlensing, respectively. For the planets detected by the radial velocity, $m_p \sin i$ is plotted. The black dashed line shows the snow line. The black letters indicate planets in the solar system.

due to the universal gravitation of the planet. This technique detects the motion of the host star caused by the orbit of the planet through the shift in the central wavelengths (Doppler precession) of absorption lines of atoms and molecules that exist in the stellar spectrum. By solving the two-body problem, the periodic radial velocity is given by,

$$V = K\{\cos(f + \omega) + e\cos\omega\}, \tag{1.1}$$

where K is the radial velocity semi-amplitude, f is the true anomaly, ω is the longitude of periastron, and e is the eccentricity of the orbit. K is defined as

follows,

$$K = m_p \sin i \sqrt{\frac{G}{(m_p + M_h)a}} = \left(\frac{2\pi G}{P}\right)^{1/3} \frac{1}{\sqrt{1-e^2}} \frac{m_p \sin i}{(m_p + M_h)^{2/3}}, \quad (1.2)$$

$$\sim 0.09 \left(\frac{m_p \sin i}{m_\oplus}\right) \sqrt{\frac{1}{M_h/M_\odot}} \sqrt{\frac{1}{a/1 \text{ au}}} \text{ m/s}, \quad (1.3)$$

$$\sim 12.5 \left(\frac{m_p \sin i}{m_{\text{Jup}}}\right) \sqrt{\frac{1}{M_h/M_\odot}} \sqrt{\frac{1}{a/5.2 \text{ au}}} \text{ m/s}, \quad (1.4)$$

$$\sim 130 \left(\frac{m_p \sin i}{m_{\text{Jup}}}\right) \sqrt{\frac{1}{M_h/M_\odot}} \sqrt{\frac{1}{a/0.05 \text{ au}}} \text{ m/s}, \quad (1.5)$$

where a is the semi-major axis, P is the orbital period, i is the inclination of the orbit, and M_h and m_p are the mass of the star and the planet, respectively. For the Earth and Jupiter around the Sun star, the value of K is 0.09 m/s and 12.5 m/s, respectively. For the hot Jupiter with $a = 0.05$ au, the value of K is 130 m/s. The radial velocity method provides us with the orbital period, P, the semi-major axis, a, the eccentricity, e, and the minimum mass of the planet, $m_p \sin i$. It is important to note that only the minimum mass can be determined because the indefiniteness of i remains. According to Equation (1.2), the radial velocity method is more sensitive to massive planets with an inner orbit close to host stars, which causes the large radial velocity semi-amplitude. When measuring the central wavelengths of absorption lines, it is difficult to measure K on stars such as distant stars and stars with low surface temperatures that do not have sufficient light intensity. It is also difficult to measure K on stars with high surface temperatures because of the small number of absorption lines. Moreover, young stars spinning at high speeds will cause less accuracy in determining the central wavelength of absorption lines.

Transit

The first planet for which a transit was detected was HD 209458b[2] in 2000 (Charbonneau et al., 2000; Henry et al., 2000). Planet search via transit method is conducted by monitoring a large number of target stars within a given time period. The *Kepler* satellite, which operated from 2009 to 2018, contributed to the discovery of more than 2,600 transit planets through its high-precision photometric observations. Assuming $R_h \gg r_p$ and a circular orbit, the geometric probability to observe a transiting planet is given by,

$$p_{\text{transit}} = \sin\left(\frac{R_h}{a}\right) \sim \frac{R_h}{a}, \quad (1.6)$$

$$\sim 0.005 \left(\frac{R_h}{R_\oplus}\right) \left(\frac{a}{1\text{au}}\right)^{-1}. \quad (1.7)$$

[2]The first detection of HD 209458b was made by the radial velocity measurement. The first exoplanet discovered via the transit method is OGLE-TR-56b (Konacki et al., 2003).

For the Earth around the Sun, the probability of transit is $\sim 0.5\%$. When a planet passes in front of a star, the flux of the star diminishes by a fractional ΔF,

$$\Delta F \simeq \left(\frac{r_p}{R_h}\right)^2 = k^2, \tag{1.8}$$

$$= 0.8 \times 10^{-4} \left(\frac{r_p}{r_\oplus}\right)^2 \left(\frac{R_h}{R_\odot}\right)^{-2}, \tag{1.9}$$

$$= 1.1 \times 10^{-2} \left(\frac{r_p}{r_{\rm Jup}}\right)^2 \left(\frac{R_h}{R_\odot}\right)^{-2}, \tag{1.10}$$

where R_h and r_p are the radii of the star and the planet, respectively, and k is the radius ratio. For the Earth and Jupiter around the Sun, the value of ΔF is 0.8×10^{-4} and 1.1×10^{-2}, respectively. The transit light curve provides us with the orbital period, P, the radius ratio, k, the orbital inclination, i, and so on. Combining the observation of the radial velocity method, we can estimate the mass of the planet and the average density of the planet. According to Equation (1.6), the transit method is sensitive to planets in close orbits, which have a higher probability of transit. Then according to Equation(1.8), it is sensitive to planets with a larger radius, which causes deeper transit depth. We cannot determine the planet's mass only by the transit method, but it can provide accurate constraints on the radius size of planets.

Astrometry

To date, only two planets have been discovered via astrometry: DENIS-P J082303.1-491201 b (Sahlmann et al., 2013) and GJ 896 A b (Curiel et al., 2022), and both are a few to several tens of Jupiter masses. ESA's Gaia mission is expected to lead to the discovery of many more planets via the astrometry method due to its stable measurements and high precision in the long baseline. As mentioned above, a star with a planet orbits its common center of mass, so the position of the star in the sky changes with time. The astrometry method measures the proper motion of stars and the parallax due to the Earth's motion around the Sun. The astrometric amplitude of the wobble of a host star induced by its companion in au is derived straightforwardly from a balance of the star/planet system about its center of mass. The distance to the system then determines the angular size of the projected motion on the sky. Assuming a circular face-on orbit, the host star describes an ellipse on the sky whose semi-amplitude of the astrometric offset, $\Delta\theta$, is given by,

$$\Delta\theta \equiv \frac{m_p}{M_h} \cdot \frac{a}{d}, \tag{1.11}$$

$$\sim 0.33 \, \frac{m_p/m_\oplus}{M_h/M_\odot} \cdot \frac{a/1 \text{ au}}{d/10 \text{ pc}} \, \mu\text{as}, \tag{1.12}$$

$$\sim 0.52 \, \frac{m_p/m_{\rm Jup}}{M_h/M_\odot} \cdot \frac{a/5.2 \text{ au}}{d/10 \text{ pc}} \, \text{mas}, \tag{1.13}$$

where we assume $m_p \ll M_h$. For the Earth and the Jupiter around Sun at a distance of 10 pc, the magnitude of the astrometric signal $\Delta\theta$ is ~ 0.33 μas and ~ 0.52 mas, respectively. So $\Delta\theta$ decreases with increasing the host star mass and the distance, but increases with the increase of the planet mass and longer orbital period. According to Equation (1.11), the astrometry method is more sensitive to massive planets with wide orbits, which cause the large astrometric semi-amplitude. The typically detectable orbital periods are several years. The detection probability is high because it does not depend on planets being in straight alignment with the line of sight from the Earth. Astrometric amplitude provides an accurate estimate of a planet's mass.

Direct Imaging

Direct imaging is to detect a planet as a point source of light. The light from a planet is divided into two: a reflected light from the host star by visible or the planet's own thermal emission by infrared. However, in both cases, the reflection or the emission of the planets is quite faint compared to the light of the host stars. It is easier to detect planets with lower flux contrast and larger angular separation between the planet and the host star. The reflected light is in the shape of the blackbody radiation spectrum of the stellar temperature and the emission light is in the shape of the blackbody radiation spectrum of the planetary temperature. When there is a temperature difference between the host star and the planet, reflected light and emission light is observed separated in the wavelength direction.

The flux contrast between the planet and the host star for the reflected light is given by,

$$f_{\mathrm{ref},\lambda} = \frac{2\phi(\beta)}{3} A_{g,\lambda} \left(\frac{r_p}{a}\right)^2, \tag{1.14}$$

$$\sim 1.1 \times 10^{-10} \left(\frac{A_{g,\lambda}}{0.3}\right) \left(\frac{r_p}{r_\oplus}\right)^2 \left(\frac{a}{1\mathrm{au}}\right)^{-2}, \tag{1.15}$$

$$\sim 0.8 \times 10^{-9} \left(\frac{A_{g,\lambda}}{0.5}\right) \left(\frac{r_p}{r_{\mathrm{Jup}}}\right)^2 \left(\frac{a}{5\mathrm{au}}\right)^{-2}, \tag{1.16}$$

where $A_{g,\lambda}$ is the geometric albedo, $\phi(\beta)$ is the phase function which depends on the planetary phase angle β, a is the semi-major axis, r_p is the planetary radius. Assuming a half-planet $\phi(\beta = 90^\circ) = 0.3$, for the Earth and the Jupiter around the Sun at a distance of 10 pc, the value of the flux contrast $f_{\mathrm{ref},\lambda}$ is $\sim 10^{-10}$ and $\sim 10^{-9}$, respectively.

The flux contrast between the planet and the host star for the thermal emission

is given by,

$$f_{\mathrm{therm},\lambda} = \left(\frac{r_p}{R_h}\right)^2 \frac{t_p}{T_h} g(\alpha), \tag{1.17}$$

$$\sim 4.2 \times 10^{-6} \left(\frac{r_p}{r_\oplus}\right)^2 \left(\frac{R_h}{R_\odot}\right)^{-2} \left(\frac{t_p}{300\mathrm{K}}\right) \left(\frac{T_h}{6000\mathrm{K}}\right)^{-1}, \tag{1.18}$$

$$\sim 2.1 \times 10^{-4} \left(\frac{r_{\mathrm{Jup}}}{r_\oplus}\right)^2 \left(\frac{R_h}{R_\odot}\right)^{-2} \left(\frac{t_p}{120\mathrm{K}}\right) \left(\frac{T_h}{6000\mathrm{K}}\right)^{-1}, \tag{1.19}$$

$$\sim 1.8 \times 10^{-3} \left(\frac{r_{\mathrm{Jup}}}{r_\oplus}\right)^2 \left(\frac{R_h}{R_\odot}\right)^{-2} \left(\frac{t_p}{1000\mathrm{K}}\right) \left(\frac{T_h}{6000\mathrm{K}}\right)^{-1}, \tag{1.20}$$

where R_h is the radius, t_p and T_h is the surface temperature of the planet and the host star, respectively. The thermal emission of the planet is assumed to be sufficiently redder wavelength. For the Earth and the Jupiter around Sun, the value of the flux contrast $f_{\mathrm{therm},\lambda}$ is $\sim 10^{-6}$ and $\sim 10^{-4}$, respectively. For a self-luminous planet, which is a young planetary system, less than 0.1 Gyr at the most, and in the process of cooling down from a planet that was hot when it formed, the flux contrast of thermal emission is $\sim 10^{-3}$.

Direct imaging of the planets is difficult, but currently, it has been achieved for young self-luminous planets using large telescopes with Adaptive optics, coronagraphs, or interferometers, in order to reduce the impact of the host star. By the direct imaging of the planets, we can obtain the spectra, and thus characterize the atmospheric components. It can measure the spectrum information of planets directly. It is primarily sensitive to planets in wide orbits $a > 10$ au or in eccentric orbits due to the large projected separations on the sky. It is sensitive to gas-giant plants with higher surface temperatures in the young systems because they are bright in the infrared wavelength region. When a host star is faint, it is easy to separate a planet from a host star.

Microlensing

When a foreground lens star passes the line of sight between an observer and a background source star, the gravity of the lens star bends the light from the source star and magnifies its brightness. This phenomenon is called the "Gravitational microlensing phenomenon". If the lens star has a planet, its gravity affects the magnification of the source star. So the characteristic light curve is obtained. By light curve modeling, we can get some parameters of the planetary system. Although the details are reviewed in Chapter 2, the typical value of an Einstein radius, R_{E} is,

$$R_E \simeq 2.6\,\mathrm{au} \left(\frac{M_h}{0.5 M_\odot}\right)^{1/2} \left(\frac{D_S}{8\,\mathrm{kpc}}\right)^{1/2} \left(\frac{x\,(1-x)}{0.2}\right)^{1/2} \tag{1.21}$$

where $x \equiv D_L/D_S$, and, D_L and D_S are the distance to a lens and a source from the observer, respectively. Equation (1.21) shows that the microlensing method is relatively sensitive to the outer planets. The characteristics of the microlensing

method are summarized below. The microlensing method is the only way to detect planets down to the mass of Mercury beyond the snow line ($\sim 2-10$ au). Because the brightness of the host star is irrelevant, it can find planets around brown dwarfs, main-sequence stars, and stellar remnants. Planets around M-dwarfs account for a large percentage of detected planets by microlensing method because M-dwarfs are most common in our Galaxy. It can also detect free-floating planets, which have the planetary mass but are not bound by the planetary system. It is the only technique that probes planets in the wide range of Galactocentric distances from the disk to the bulge. The probability of observing a single stellar microlensing event is low, of an order of 10^{-6}. Furthermore, the probability of observing a planetary microlensing event is of an order of 10^{-8} merely. The follow-up observation is difficult because the planetary system detected by the microlensing method is usually far from the solar system and has a faint host star. From the light-curve modeling, we cannot get the physical parameters of planetary systems, such as mass and distance, but the mass ratio and standardized separation between the star and the planet. We can determine lens physical parameters only if some higher-order effects are detected.

1.1.2 Formation theory

The current standard theory of planet formation, the core accretion model, is intended to explain the formation of our Solar system. In addition to the core accretion theory, the pebble accretion process (Ormel & Klahr, 2010), which explains the formation of terrestrial planets, and the gravitational disk instability (Boss, 1997, 2006), which explains the formation of gas planets, have been proposed.

In the core accretion theory, when a planet forms, a "core" with a small mass forms first, on top of which gas collects to complete the planet (Safronov, 1972; Hayashi et al., 1985; Lissauer, 1993). The planet's formation starts when the star has a protoplanetary disk. Since the star is still on the way to evolution, there is so much dust in collapsing molecular clouds. The scenario of the planet formation is described below,

1. Dust as small as $\sim 0.1\mu$m falls on the central plane of the protoplanetary disk. Dust consists of rock inside the snow line and ice outside the snow line.

2. Larger masses of a few km in size, or planetesimals, are formed by collisional processes or gravitational instabilities in the protoplanetary disk.

3. Terrestrial planets or more massive ice cores of giant planets are formed by the collection of planetesimals.

4. The accretion of gas onto the cores forms the giant planets.

Here the main components of dust are dust depending on whether the dust is inside the snow line or outside the snow line. The snow line is the boundary where water sublimates and condenses. In typical protoplanetary disks, the snow line is located where the gas temperature is $\sim 160-170$ K (Hayashi, 1981). When we

assume that the disk is optically thin and its internal temperature is determined by direct stellar irradiation only, the snow line distance is

$$a_{\rm snow} = 2.7 \left(\frac{L_h}{L_\odot} \right)^{1/2} \quad {\rm au}, \tag{1.22}$$

where L_h is the luminosity of the host star. Considering the mass-luminosity relation for main-sequence stars, $L_h \propto M_h^4$, the location of the snow line is rewritten as $a_{\rm snow} = 2.7(M_h/M_\odot)^2$ (Ida & Lin, 2004; Kennedy & Kenyon, 2008).

According to the core accretion model, the terrestrial planets are formed prior to the giant planet and it takes a longer time to form planets with wider orbits. However, there are some problems in the core accretion model. The main problem is that the time it takes to form the giant planets is almost the same as the time for the depletion of the gas in the disk. By observation, some giant planets in wide orbits (> 30 au) are found, which the core accretion theory cannot explain how to form. Ida & Lin (2005) shows that the formation probability of gas giants around low-mass host stars such as M-dwarfs and K-dwarfs is much low because the gaseous disk lifetimes (> 10 Myr) are shorter than the timescales of the formation of gas giants.

1.2 Milky Way Galaxy

1.2.1 Galactic structure

First, let me explain the structure of our Galaxy. Our Galaxy consists of an elliptical bulge/bar near the Galactic center, thin and thick lens-like disks, and a spherical halo surrounding the bulge and disk. Here is a brief introduction to these properties. Figure 1.2 shows the schematic view of the Galaxy.

Bulge/Bar

There is an ellipsoid component called the bulge in the center of the Galaxy. Observation in the Galactic center is difficult because the interstellar dust attenuates the light by about 30 mag in visible light. However, by observing the baade window region, where the attenuation is as low as 2 mag, we were able to identify the stellar population in the bulge. Color Magnitude Diagram (CMD) suggests that the main-sequence star in the bulge is more than 10 billion years (Ortolani et al., 1995; Clarkson et al., 2008). It is known that there is a triaxial bar with the semi-major axis $\sim 3 - 4$ kpc and tilted by $\sim 20^\circ - 30^\circ$ toward the Sun by measurements of the three-dimensional density distribution of the bulge red clump giants (i.e, Stanek et al., 1997).

Disk

The disk component, which has a radius of up to 10 kpc, is divided into a thin disk with a thickness of about $0.3 - 0.4$ kpc and a thick disk with a thickness of

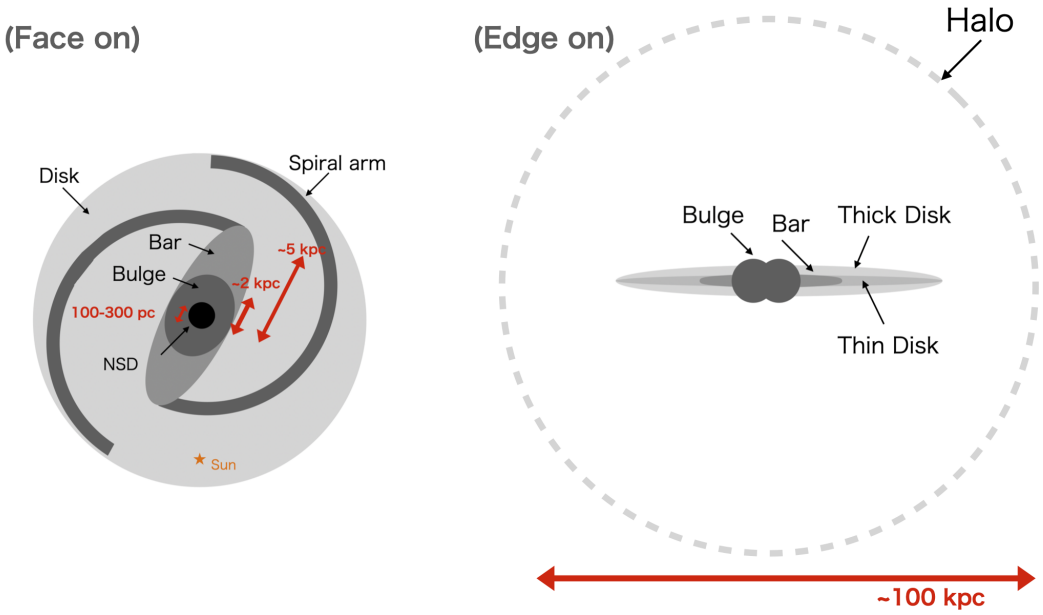

Figure 1.2: The schematic view of the Galaxy. The Galaxy consists of an elliptical bulge/bar near the Galactic center, thin and thick lens-like disks, and a spherical halo. The bar tilted by $\sim 20^\circ - 30^\circ$ toward the Sun. Sun's distance from the Galactic center is ~ 8.2 kpc.

about $1-1.5$ kpc. They differ in age, scale height, and chemical properties. Stars in thick disks have [Fe/H] less than -0.4 and have smaller metallicity than stars in thin disks. Metal abundances indicate the age of stars, and the age of stars in thick disks is estimated to be more than 10 Gyr. On the other hand, in thin disks, the metallicity is high and many of the stars are younger than 10 Gyr.

Halo

The halo is the spherical component surrounding the disk. Halos, like stars in globular clusters, were first identified as an old, fast-moving, metal-poor population of stars near the Sun. Halo stars have large random motions and little rotation. The estimated mass distribution from the rotational velocity of the Galaxy is much larger than the estimated mass of the stars and gas combined. This suggests that the halo is filled with dark matter.

1.2.2 Galactic center

At the Galactic center, there are the supermassive black hole Sagittarius A* (Sgr A*), the nuclear star cluster (NSC), and the nuclear stellar disc (NSD). The gravitational field of Sgr A* black affects the $\sim 1-2$ pc around the Galactic center (i.e, Feldmeier et al., 2014). NSC is a massive stellar cluster with a dynamical mass of $\sim 1.8 \times 10^7 M_\odot$ and an effective radius of $\sim 4-5$ pc (Bland-Hawthorn & Gerhard, 2016). NSD is a disc-like structure with a dynamical mass of $\sim 10.5 \times 10^8 M_\odot$, a

radius of $\sim$ 230 pc, and a thickness of $\sim$ 45 pc (i.e, Sormani et al., 2022). Because observations of them are difficult due to the extreme star crowding and high extinction, their relation and formation process are not well understood yet.

1.2.3 Galactic formation and evolution

The exploration of halo regions containing many old-age stars has provided insight into the formation of the Galaxy. Eggen et al. (1962) studied a large number of high-velocity stars in the solar neighborhood and found a correlation between the orbital kinetic energy and orbital eccentricity of stars increasing with decreasing metallicity. This led them to propose a theory that the protogalactic gas in the Milky Way underwent a free-fall-like contraction within a dynamical time of about 100 million years, in which stars were born and chemical evolution proceeded (ELS scenario, or rapid collapse model). On the other hand, Searle & Zinn (1978) found that the metallicity of globular clusters in the galactic halo is independent of distance from the galactic center. This led him to propose a theory that the formation of galaxies is not a single contraction, but rather the random merging of individual independent stellar clumps over a period of about one billion years (SZ scenario, or slow collapse model). Although a number of papers have been published on the above scenario, it has been difficult to conclude which scenario is more plausible because the conclusions may be influenced by the sampling method of halo stars and the derivation of physical quantities such as metallicities. Astrometric observations with the HIgh Precision PARallax COllecting Satellite (Hipparcos) have advanced stellar kinematics studies, and multiple observations have recently provided evidence for galaxy mergers. It has become clear that, in addition to the accretion-merger process of dwarf galaxies, the contraction process of protogalactic clouds with the energy dissipation of interstellar gas must also be taken into account.

1.3 Applications of Microlensing

1.3.1 Planet/Star Mass ratio function

The frequency of cold planets has been estimated by a number of statistical analyses using microlensing planets (Gould et al., 2010; Sumi et al., 2010; Cassan et al., 2012; Shvartzvald et al., 2016; Suzuki et al., 2016; Poleski et al., 2021; Udalski et al., 2018; Jung et al., 2019a; Zang et al., 2022a). Suzuki et al. (2016) conducted the most comprehensive systematic statistical analysis and used 29 planets found by MOA-II microlensing survey from 2007 to 2012. For the first time, they found that the mass-ratio function is well fit by a broken power-law model and that there is a likely peak in the mass-ratio function near a Neptune mass,

$$f(s,q;A,n,m,p) = \frac{d^2N_{\rm pl}}{d\log q d\log s} = A\left(\frac{q}{q_{\rm br}}\right)^n s^m \quad \text{for } q > q_{\rm br} \tag{1.23}$$

$$= A\left(\frac{q}{q_{\rm br}}\right)^p s^m \quad \text{for } q < q_{\rm br}, \tag{1.24}$$

where q is a planet–star mass ratio, and s is projected planet–star separation in Einstein radius units, and $q_{\rm br} \equiv 1.7 \times 10^{-4}$ is the mass ratio of the break. Their analysis yields $A = 0.61^{+0.21}_{-0.16}$, $n = -0.93 \pm 0.13$, $m = 0.49^{+0.47}_{-0.49}$, and $p = 0.6^{+0.5}_{-0.4}$. However, there is still a large degree of uncertainty in the location of the break (or peak) in the planet mass-ratio distribution owing to the lack of low-mass planets in their analysis. The total number of planets per star estimated from the equation (1.23) is $N_{\rm total} \sim 0.41$, which is calculated in Poleski et al. (2021). Recently, Zang et al. (2022a) have suggested a possibility that planets with lower mass-ratio than the mass-ratio break ($q_{\rm br} \equiv 1.7 \times 10^{-4}$) are more abundant than previous results. Their analysis used 13 planets including lower mass-ratio planets with $q \sim 10^{-5}$ detected by KMTNet but did not correct for detection efficiencies. Poleski et al. (2021) conducted a systematic search for wide-orbit planets with separations of $5 - 15$ au in 20 years of OGLE data and found that the total number of ice giant planets per star is $N_{\rm total} = 1.4^{+0.9}_{-0.6}$.

Suzuki et al. (2018) compared the cold-planet mass-ratio function derived by Suzuki et al. (2016) to predictions by population synthesis models based on the core accretion theory (e.q. Ida & Lin, 2004). Core accretion model with the planetary migration effect predicts that the planetary occurrence rate is a factor of $10 - 25$ less with lower mass-ratios, $10^{-4} \leq q \leq 10^{-3}$, and it is a factor of about 5 less with higher mass-ratios, $10^{-3} < q \leq 0.03$ than inferred from microlensing observations. Even without including the effects of planetary migration, the planet occurrence rate is about a factor of ~ 10 less with mass-ratios, $1 \times 10^{-4} \leq q \leq 4 \times 10^{-4}$ than estimated from microlensing observations. Therefore, microlensing results suggest the need for modifications of the planet formation theory.

The next goal of planetary search with microlensing is to extend the above analysis to elucidate not the mass ratio function of planets beyond the snow line, but their mass distribution down to low masses and dependence on the mass of the host star and its location in the Galaxy.

1.3.2 Dependency of Planet frequency on the Galactic location

Statistical analysis using microlensing planets provides constraints on the dependence of cold planet frequency on the Galactic components and location by using the Galactic models (Penny et al., 2016; Koshimoto et al., 2021b). Penny et al. (2016) investigated whether the estimated distances to 31 planetary systems are consistent with the distribution of planets expected from the Galactic model. Although they did not correct for the detection efficiency of planets, they found that the relative frequency of planets in the bulge to that in the disk is $f_{\rm bulge} < 0.54$, which means that the bulge could be devoid of planets compared to the disk. Koshimoto et al. (2021b) used the statistical samples in Suzuki et al. (2016) and measured the planet-hosting probability,

$$P_{\rm host} \propto M_L^m R_L^r, \tag{1.25}$$

where M_L is the host star mass and R_L is the Galactocentric distance. They estimated $r = 0.2 \pm 0.4$ under a plausible uniform prior for $0 < m < 2$, which

means that there is no significant dependence of the cold planet frequency on the Galactocentric distance.

1.3.3 Probe of Galactic Structure

Constraints on the bar structure

Microlensing optical depth, τ, and event timescale, $t_{\rm E}$, provides a probe of the density distribution of the Galaxy, allowing us to know the structure of the Galaxy, as discussed later in Section 2.1.5. In particular, early measurements of optical depth by OGLE (Udalski et al., 1994b) and MACHO (Alcock et al., 1997) provided independent evidence for the presence of the bar tilted by $\sim 20^\circ$ toward the Sun in the Galactic bulge. Wyrzykowski et al. (2015) compared the optical depth and timescale distributions of the ~ 3700 microlensing events observed by OGLE with the predictions from the Besançon Galactic model (Kerins et al., 2009). They found that the asymmetry of the observed timescales increased more steeply than predicted, indicating that the orientation of the bars was different[3] or that the bars were wider.

Constraints on mass function

The event timescale distribution provides a probe of the kinematics and the mass function of stars in the bulge, because the event timescale contains the information on the masses and velocities of lenses, as discussed later in Section 2.1.2. Although the mass and velocity are degenerate in the information of the timescale distribution, the Galactic model together with a parametric initial mass function (IMF) allows a statistical discussion of the expected mass and velocity of the microlensing events. Thereby, the mass distribution of the lens and the IMF slope of planetary mass objects (or free-floating planets), stars, brown dwarfs, and stellar remnants, can be measured from the timescale distribution of the microlensing events (i.e, Wegg et al., 2017; Sumi et al., 2011).

Spectroscopic observation of microlensing events

There are two methods for determining the metallicity distribution of the bulge: photometric metallicity and spectroscopic metallicity. The former is obtained by comparing isochrones obtained from stellar evolution models with observed CMD. The latter is obtained by direct spectroscopic observations. However, both observations require bright stars. On the other hand, spectroscopic observations of faint dwarfs are possible by taking advantage of the magnification of microlensing events (i.e, Bensby et al., 2013, 2017).

[3]Besançon Galactic model in that version assumes that the angle of the bar is 11.3° and that the triaxial scalelengths are 1.590, 0.424 and 0.424 kpc.

1.4 Purpose of this thesis

The gravitational microlensing method can detect low-mass planets beyond the snow-line that are not found by other planet detection methods. Therefore, the detection of more exoplanets by the gravitational microlensing method will provide an overall picture of the distribution of planets and lead to the elucidation of planet formation models.

However, there are several problems with a planetary search using the microlensing method. First, the number of planets discovered using the microlensing method is small (~ 140) because of the low probability of the microlensing phenomenon. Second, there is still a large degree of uncertainty in the location of the break (or peak) in the planet mass-ratio distribution and the slope of low mass ratio distribution owing to the lack of low-mass planets in microlensing statistical analysis.

Therefore, the purpose of this thesis is to increase the number of planet samples including low-mass planets for future statistical analysis by the microlensing planets. It would be useful to clarify the overall picture of planetary distribution beyond the snow line and provide new constraints on planet formation models. It would also be useful in elucidating the dependency of planet frequency on the Galactic location in more detail.

This paper summarizes the results of two studies. The first is an analysis of a microlensing event, OGLE-2018-BLG-1185 using space parallax effects. The observable "space parallax" can be measured by simultaneously observing microlensing events on the ground and in space, using the difference in their viewpoints. Space parallax is an important observable that provides information on the mass and distance of a lensing system. In order to measure this observable on a large number of planets, simultaneous observations with ground-based telescopes and the *Spitzer* Space Telescope by the *Spitzer* microlensing campaign were conducted in $2014-2019$. Although the *Spitzer* Space Telescope has been able to detect the space parallax effect in only a dozen or so planetary events, it is expected that in the future the *Nancy Grace Roman Space Telescope* and ground-based telescopes can be used to directly determine masses and distances for many planetary events using this effect. Therefore, it is important to gain more knowledge of modeling, including space parallax effects, to conduct future microlensing surveys.

The second is an estimation of the planet and microlensing yields by the new near-infrared telescope. In 2023, the PRime-focus Infrared Microlensing Experiment (PRIME) will start a near-infrared (NIR) microlensing survey toward the inner Galactic bulge, which cannot be seen by conventional visible observations due to high dust extinction. The major goals of the PRIME microlensing survey are to measure the microlensing event rate in the inner Galactic bulge to help design the observing strategy for the exoplanet microlensing survey by the *Roman Space Telescope* and to make the first statistical measurement of exoplanet demographics in the central bulge fields where optical observations are challenging owing to the high extinction in these fields. Prior to the start of PRIME observations, I compared four observation strategies to discover more planets and improve the performance of PRIME's microlensing observations.

This thesis is organized as follows. Chapter 2 reviews the theoretical and practical aspects of exoplanet search by gravitational microlensing. The analysis of the very low-mass ratio microlensing event OGLE-2018-BLG-1185 is presented in Chapter 3. This chapter was published as Kondo et al. (2021). I also show the estimation of microlensing yield and planet yield by the PRIME microlensing survey in Chapter 4, which is to be published by Kondo et al. (2023), in preparation. Finally, Chapter 5 summarizes the results of the two works and gives further discussions.

Chapter 2

Review of Gravitational Microlensing

In general relativity, the presence of an object warps the space surrounding it and thereby bends the trajectory of light rays. Gravitational microlensing occurs when a foreground lens star happens to cross the line of sight between an observer and a background source star. The gravity of the lens star bends and magnifies the brightness from the source star. If the lens star has a companion, its gravity affects the magnification of the source star.

Paczynski (1986) first proposed the use of gravitational microlensing to search for MAssive Compact Halo Objects (MACHOs) as potential candidates for dark matter. Subsequently, Mao & Paczynski (1991) and Gould & Loeb (1992) suggested the possibility of using this technique to search for exoplanets. In 2003, the first exoplanet, OGLE-2003-BLG-235/MOA-2003-BLG-53Lb, was discovered through gravitational microlensing (Bond et al., 2004), and more than 130 planets have since been found using this method. In 2011, free-floating planets that do not orbit a main star were discovered for the first time using gravitational microlensing (Sumi et al., 2011).

2.1 Basic Theory

2.1.1 Theory of Gravitational Lenses

Lens Equation

To begin with, I will discuss the deflection angle where a light ray is bent by a mass distribution derived from general relativity. In general, the radius of the lens is much smaller than the distance from the observer to the lens or from the lens to the light source, so projecting along the line of sight makes the deflection angle a two-dimensional problem (Thin Lens Approximation). Furthermore, with a circularly symmetric lens, the deflection angle is considered to be one-dimensional. Under

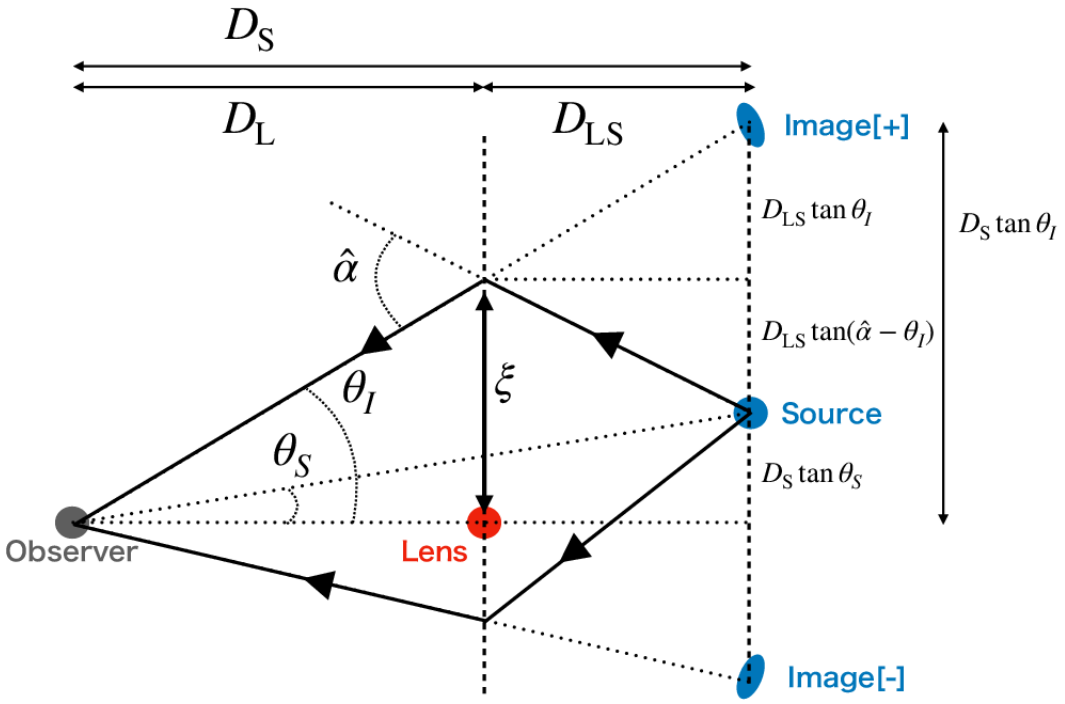

Figure 2.1: The geometry of the gravitational lensing. The gravity of the lens star at $D_{\rm L}$ bends the light from the source star at $D_{\rm S}$ by the Einstein bending angle δ and magnifies its brightness. . The distance between lens and source is D_{LS}. θ_S is the angular position of the unlensed source, and θ_I is the angular position of one of the images.

those conditions, the deflection angle is

$$\hat{\alpha}(\xi) = \frac{4GM(\xi)}{c^2\xi}, \tag{2.1}$$

$$\text{with} \quad M(\xi) \equiv 2\pi \int_0^{\xi} \Sigma(\xi')\xi' d\xi', \tag{2.2}$$

where c is the speed of light in vacuum, G the gravitational constant, the distance from the lens center $\xi = D_L\theta_I$, $M(\xi)$ is the mass enclosed within radius ξ, and $\Sigma(\xi)$ is the surface mass density.

This deflection angle is used to determine where the source image will be formed for a given source position, which is the lens equation. Figure 2.1 shows the geometry of the gravitational lensing and trajectory of a light ray in a weak gravitational field. A lens object and a bright source star are located at D_L and D_S away from the observer, respectively. The distance between the lens and source is D_{LS}. θ_S is the angular position of the unlensed source, and θ_I is the angular position of one

of the images. From Figure 2.1, we have the geometric relation

$$D_S \tan\theta_S = D_S \tan\theta_I - D_{LS} \tan\hat{\alpha}. \tag{2.3}$$

With the small-angle approximation ($\tan\vartheta \approx \vartheta$), Equation (2.3) reduces to

$$D_S\theta_S = D_S\theta_I - D_{LS}\hat{\alpha}. \tag{2.4}$$

Introducing the reduced deflection angle,

$$\alpha(\theta_I) \equiv \frac{D_{LS}}{D_S}\hat{\alpha}(D_L\theta_I), \tag{2.5}$$

the lens equation is finally obtained

$$\theta_S = \theta_I - \alpha(\theta_I). \tag{2.6}$$

Image Magnification by Point Mass Lens model

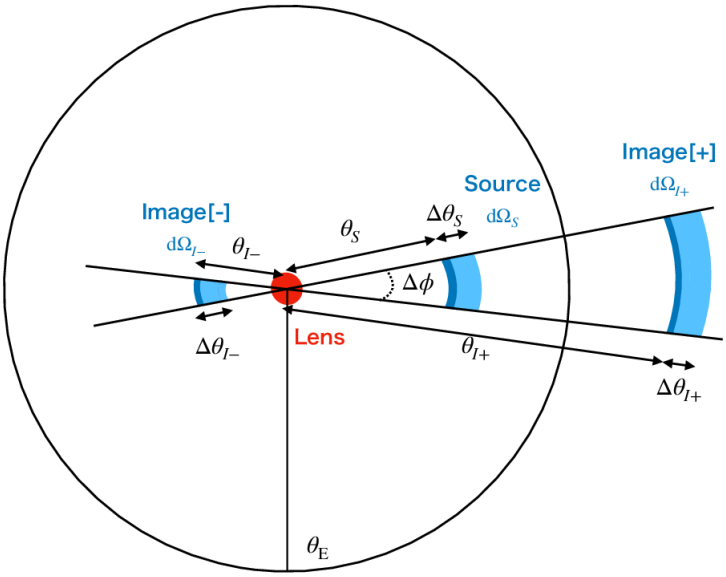

Figure 2.2: Magnification of lensed images.

Next, the simplest lens model, a point mass M, is used to derive the lens equation and calculate the magnification. Substituting $M(\xi) = M$ into Equation (2.1) and using Equation (2.5), the reduced deflection angle is given by

$$\alpha = \frac{D_{LS}}{D_L D_S}\frac{4GM}{c^2\theta_I} \tag{2.7}$$

Then the lens equation (Equation 2.6) becomes

$$\theta_S = \theta_I - \frac{\theta_E^2}{\theta_I}, \tag{2.8}$$

where $\theta_{\rm E}$ is the angular Einstein radius. The angular separation between two images of the source is the order of $2\theta_{\rm E}$. When we observe typical microlensing sources in the galactic bulge, a typical size of angular Einstein radius is,

$$\theta_{\rm E} \equiv \sqrt{\frac{D_{LS}}{D_L D_S}\frac{4GM}{c^2}} \tag{2.9}$$

$$\simeq 391\,\mu as \left(\frac{M}{0.5M_\odot}\right)^{1/2}\left(\frac{D_{\rm S}}{8\,{\rm kpc}}\right)^{-1/2}\left(\frac{(1-x)/x}{0.3}\right)^{1/2}, \tag{2.10}$$

where $x \equiv D_L/D_S$. We can define a physical distance on the lens plane as an Einstein radius, $R_{\rm E}$,

$$R_E \equiv D_{\rm L}\,\theta_{\rm E} \equiv \sqrt{\frac{4GM}{c^2}\,D_{\rm S}\,x\,(1-x)} \tag{2.11}$$

$$\simeq 2.6\,{\rm au}\left(\frac{M}{0.5M_\odot}\right)^{1/2}\left(\frac{D_{\rm S}}{8\,{\rm kpc}}\right)^{1/2}\left(\frac{x\,(1-x)}{0.2}\right)^{1/2}, \tag{2.12}$$

as noted in Equation (1.21) of Section 1.1.1. Therefore microlensing method is mainly sensitive to planets located a few au from their host stars.

The equation (2.8) is solved for θ_I,

$$\theta_{I\pm} = \frac{\theta_S \pm \sqrt{\theta_S^2 + 4\theta_{\rm E}^2}}{2} \tag{2.13}$$

Because of Liouville's theorem, surface brightness is preserved but the apparent solid angle of a source is changed by gravitational light deflection. The magnification factor at given an image with position θ_I is

$$|A| = \left|\frac{d\Omega_I}{d\Omega_S}\right| = \left|\frac{\theta_I {\rm d}\theta_I}{\theta_S {\rm d}\theta_S}\right|, \tag{2.14}$$

where $d\Omega_I$ and $d\Omega_S$ are elements of solid angle in the lens in the lens plane, respectively (Figure 2.2).

For point mass lens, the magnifications of the two images are obtained using Equation (2.8),

$$A_\pm = \left[1 - \left(\frac{\theta_{\rm E}}{\theta_{I\pm}}^4\right)^{-1}\right] = \frac{u^2+2}{2u\sqrt{u^2+4}} \pm \frac{1}{2}, \tag{2.15}$$

where the source position in units of the Einstein radius, $u \equiv \theta_S/\theta_{\rm E}$.

When the separation between two images $(\theta_{I+} - \theta_{I+})$ is small, they cannot be resolved and are observed as a single image,

$$A_{\rm tot} \equiv |A_+| + |A_-| \tag{2.16}$$

$$= \frac{u^2+2}{u\sqrt{u^2+4}}, \tag{2.17}$$

$$\simeq u^{-1} \qquad ({\rm for}\ u \ll 1), \tag{2.18}$$

$$\simeq 1 \qquad ({\rm for}\ u \gg 1), \tag{2.19}$$

2.1.2 Single Lens Microlensing

In general, because the lens and source star has some velocity relative to the observer, u depends on time and so does A. If we assume the lens and source star are moving inertially with respect to the observer, we can describe the time-dependent impact parameter in units of the Einstein radius as,

$$u(t) = \sqrt{u_0^2 + t_n^2} \tag{2.20}$$

$$= \sqrt{u_0^2 + \left(\frac{\mu_{\rm rel}}{\theta_{\rm E}}(t - t_0)\right)^2} \tag{2.21}$$

$$= \sqrt{u_0^2 + \left(\frac{t - t_0}{t_{\rm E}}\right)^2}, \tag{2.22}$$

where u_0 is the minimum impact parameter, t_0 is the time of lens-source closest approach ($u = u_0$), $\mu_{\rm rel}$ is the lens-source relative transverse velocity assuming the relative linear motion. $t_{\rm E}$ is the Einstein radius crossing time defined as

$$t_{\rm E} \equiv \frac{\theta_{\rm E}}{\mu_{\rm rel}} = \frac{1}{\mu_{\rm rel}}\sqrt{\frac{4GM}{c^2 D_{\rm S}}\frac{1-x}{x}}, \tag{2.23}$$

$$\simeq 22 \text{ days} \left(\frac{M}{0.5M_\odot}\right)^{1/2} \left(\frac{D_{\rm S}}{8\,\text{kpc}}\right)^{1/2} \left(\frac{x\,(1-x)}{0.2}\right)^{1/2} \left(\frac{v_\perp}{200\text{ km/s}}\right)^{-1} \tag{2.24}$$

where $v_\perp$ is the transverse velocity. Because the Einstein radius crossing time $t_{\rm E}$ is proportional to the square root of the lens mass M, the mass of the lens is expected to be small with a short timescale event.

The equation (2.18) is written as,

$$A(t) = \frac{y^2 + u_0^2 + 2}{\sqrt{y^2 + u_0^2}\sqrt{y^2 + u_0^2 + 4}}, \quad y \equiv \frac{t - t_0}{t_{\rm E}}. \tag{2.25}$$

The magnification $A \geq 1.34$, which corresponds to $u_0 \leq 1$, is often used as a threshold to detect the microlensing event.

2.1.3 Binary Lens Microlensing

Lens Equation

Next, we will discuss the case where the lens is not a single object, but rather two objects, such as a binary star or a star with a planet. This binary lensing system exhibits a very diverse luminosity curve. We define the lens as two point masses M_1 and M_2 at distance D_L from the observer. On the lens plane, we choose a coordinate system (x, y) where the x-axis passes through both masses and the origin is defined as the midpoint of the line connecting them. Define another coordinate system (u, v) on the light source plane that is parallel to (x, y) and whose origin is at the intersection with the optical axis.

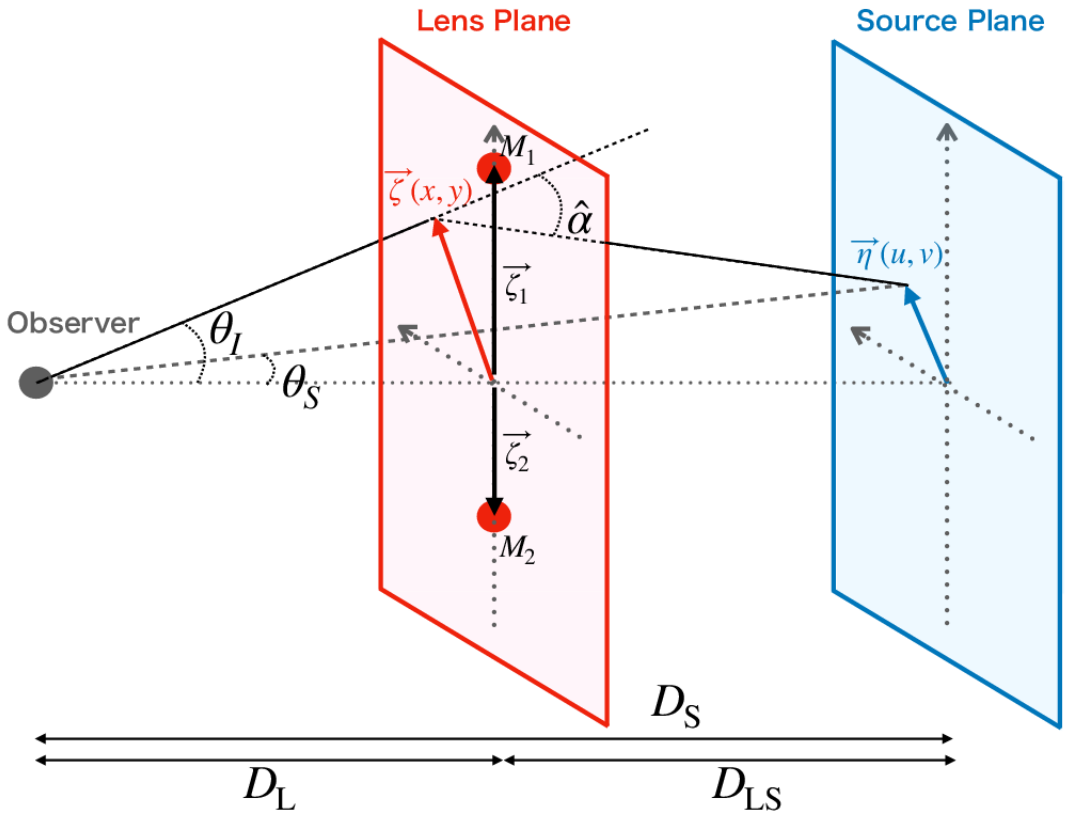

Figure 2.3: The geometry of gravitational microlensing by a binary lens.

Assuming a geometrically thin lens, when two lens masses are involved, the total deflection angle is the vector sum of all individual deflections. Adding up the contributions of each deflection mass, the deflection angle of such a compound lens can be written as

$$\vec{\hat{\alpha}} = \frac{4GM_1}{c^2}\frac{\vec{\zeta}-\vec{\zeta}_1}{|\vec{\zeta}-\vec{\zeta}_1|^2} + \frac{4GM_2}{c^2}\frac{\vec{\zeta}-\vec{\zeta}_2}{|\vec{\zeta}-\vec{\zeta}_2|^2}, \tag{2.26}$$

where $\vec{\zeta}_1$ and $\vec{\zeta}_2$ indicate the position of the two lenses in the lens plane.

The binary-lens equation can be written as

$$\vec{\eta} = \vec{\zeta}\frac{D_S}{D_L} - D_{LS}\vec{\hat{\alpha}}(\vec{\zeta}), \tag{2.27}$$

where $\vec{\eta}$ is the position of the source in the source plane and $\vec{\zeta}$ is the source image position in the lens plane.

However, as can be seen from the form of this equation, unlike the single lens case, the position of the source object and the position of the image are not parallel and cannot be considered in one dimension. Since it is difficult to think in general as a vector quantity as it is, we will consider it as a complex number so that it can be treated as a scalar quantity.

If we take the source plane $\vec{\eta}$ to be the source complex plane $\vec{w} = (D_L/D_S) \cdot \vec{\eta}/R_{\rm E}$ and the lens plane $\vec{\zeta}$ to be the lens complex plane, $\vec{z} = \vec{\zeta}/R_{\rm E}$, and the position of the source object is w, the possible position is z, and the positions of the two objects are $\vec{z_1}$ and $\vec{z_2}$, the binary-lens equation (2.27) becomes

$$\vec{w} = \vec{z} - \epsilon_1 \frac{\vec{z} - \vec{z_1}}{|\vec{z} - \vec{z_1}|^2} - \epsilon_2 \frac{\vec{z} - \vec{z_2}}{|\vec{z} - \vec{z_2}|^2}, \tag{2.28}$$

where $\epsilon_1 = M_1/(M_1 + M_2)$ and $\epsilon_2 = M_2/(M_1 + M_2)$. Then Equation (2.28) is can be rewritten using complex notation

$$w = z - \frac{\epsilon_1}{\bar{z} - \bar{z_1}} - \frac{\epsilon_2}{\bar{z} - \bar{z_2}}, \tag{2.29}$$

where $w = u + iv$ and $z = x + iy$ are now complex numbers and $\bar{w}$ and $\bar{z}$ are their complex conjugates. The conjugation of Equation (2.29) is

$$\bar{w} = \bar{z} - \frac{\epsilon_1}{z - z_1} - \frac{\epsilon_2}{z - z_2}. \tag{2.30}$$

Finally, the fifth-order polynomial equation is obtained from Equation (2.29) and (2.30),

$$\begin{aligned} &(z-w)\left\{(\bar{w}-\bar{z_1})(z-z_1)(z-z_2)+\epsilon_1(z-z_2)+\epsilon_2(z-z_1)\right\} \\ &\quad\times\left\{(\bar{w}-\bar{z_2})(z-z_1)(z-z_2)+\epsilon_1(z-z_2)+\epsilon_2(z-z_1)\right\} \\ &+\epsilon_1(z-z_1)(z-z_2)\left\{(\bar{w}-\bar{z_2})(z-z_1)(z-z_2)+\epsilon_1(z-z_2)+\epsilon_2(z-z_1)\right\} \\ &+\epsilon_2(z-z_1)(z-z_2)\left\{(\bar{w}-\bar{z_1})(z-z_1)(z-z_2)+\epsilon_1(z-z_2)+\epsilon_2(z-z_1)\right\} = 0. \end{aligned} \tag{2.31}$$

This equation means that the binary lens system will permit a maximum of five images and cannot be solved analytically. However, we can solve this equation numerically, and find three or five solutions for the image positions z in the binary lens.

Image Magnification by Binary lensing system

Then the magnification A_j of each image j is expressed by the inverse of the Jacobian determinant of the mapping by the binary-lens equation,

$$A_j = \frac{1}{\det J}\bigg|_{z=zj};\ \det J = 1 - \left|\frac{\partial w}{\partial \bar{z}}\right|^2;\ \frac{\partial w}{\partial \bar{z}} = \frac{\epsilon_1}{(\bar{z} - \bar{z_1})^2} + \frac{\epsilon_2}{(\bar{z} - \bar{z_2})^2}. \tag{2.32}$$

In a microlensing event, each image cannot be resolved, so the total magnification A can be given by,

$$A \equiv \sum_j |A_j|. \tag{2.33}$$

When ϵ_1 and ϵ_2 are the ratios of the host mass and the companion mass to the total mass, respectively, the relation between $\epsilon_{1,2}$ and q is given by $\epsilon_1 = 1/(1+q)$

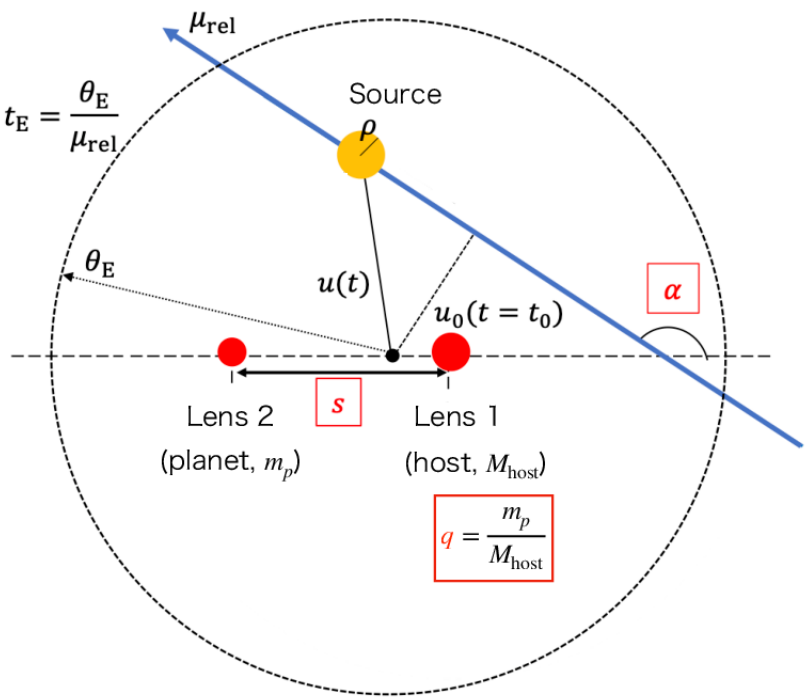

Figure 2.4: The parameters of the binary lens event on the lens plane. The yellow circle shows the source. The red circles show the binary lens. The black circle shows the center of mass of the binary lens.

and $\epsilon_2 = q/(1+q)$, where q is the companion–host mass ratio, $q \equiv m_p/M_{\rm host}$. Therefore, the magnification depends on the companion-host mass ratio, q, and the companion-host separation in units of the Einstein radius, $s \equiv |z_1 - z_2|$. The magnification A changes with time in the binary lens event as well as the magnification in the single lens event. So we require the additional parameter which explains the source trajectory, i.e., the angle between the trajectory of the source and the planet-host axis, α. Figure 2.4 shows the parameters of the binary lens event.

Caustic and Critical curve

According to the equation (2.32), when $\det J = 0$, the magnification diverges to infinity. The critical curves are the regions where the magnification is infinite on the lens plane. The caustics are the set of source positions where the mapping has a singularity, i.e., a point source has an infinite magnification. For a single lens, the caustic is the single point behind the lens. For binary lens, on the other hand, the position and shape of caustics depend on the plane–host mass ratio, q, and the angular plane–host separation in units of the Einstein radius, s. The critical curve is the positions of images of these caustics on the lens plane. The

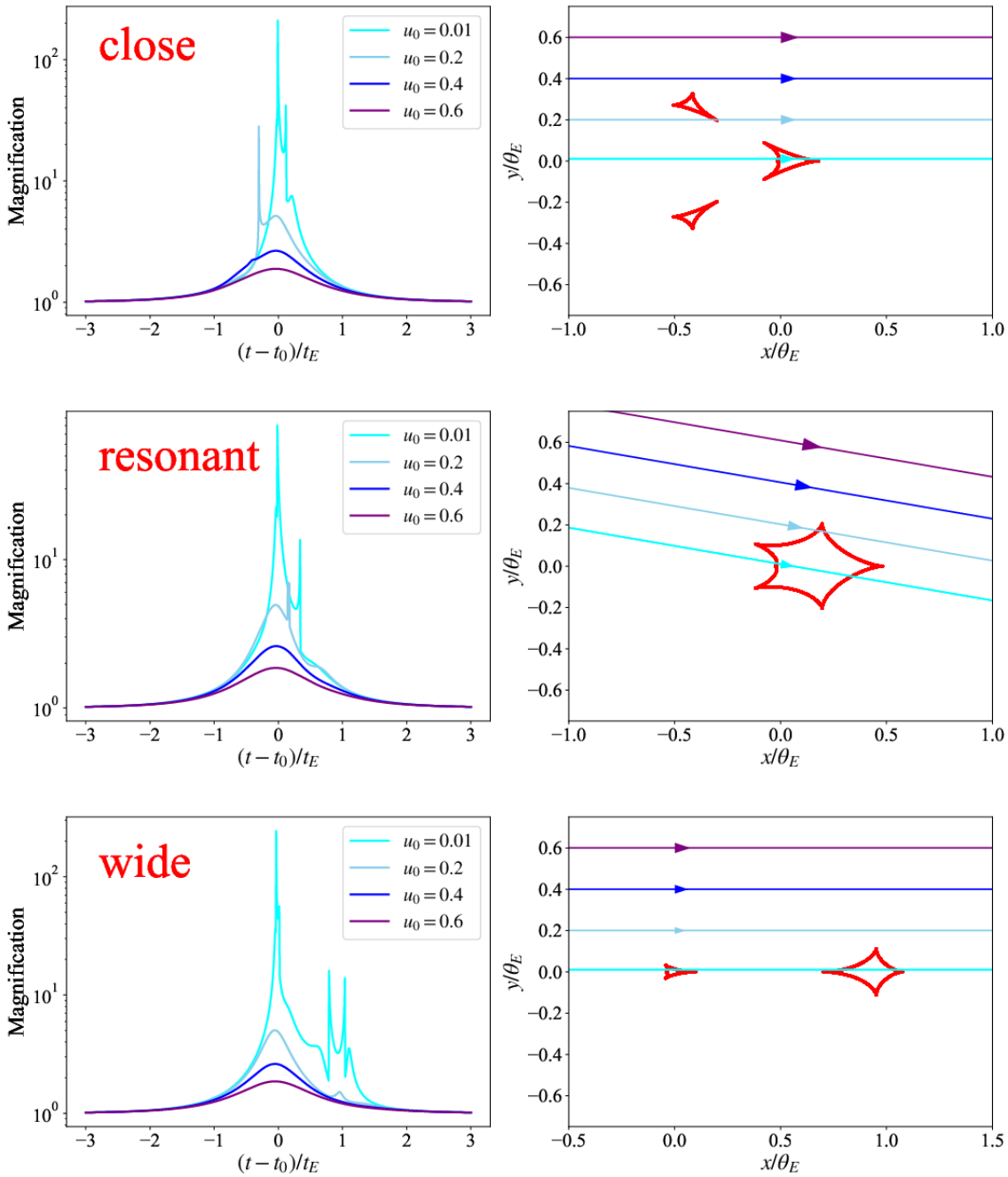

Figure 2.5: The left panels show the light curves of three topologies: close, resonant, and wide. The parameters of the binary lens with the mass ratio of $q = 0.03$ and the separation of s = 0.8, 1.1, and 1.6, respectively. The different color light curves are for different values of u_0. The right panels are the corresponding caustic topologies. The red lines show caustic.

critical curve corresponds to the Einstein ring for the single lens case. When the source is inside and outside of caustics, the number of images is five and three, respectively. Depending on q and s, caustics produce close, resonant, and wide topologies (Schneider & Weiss, 1986; Erdl & Schneider, 1993). The values of s for which the topology for a given q changes are given by,

$$\frac{(1-{s_c}^4)^3}{27{s_c}^8} = \frac{q}{(1+q)^2}, \tag{2.34}$$

$$s_w = \frac{(1+q^{1/3})^{2/3}}{(1+q)^{1/2}}, \tag{2.35}$$

where s_c and s_w represent the separation of the close and wide range, respectively (Schneider & Weiss, 1986; Cassan, 2008). Figure 2.5 shows these light curves and caustic topologies for different values of u_0 when the parameters of the binary lens with the mass ratio of $q = 0.03$ and the separation of s = 0.8, 1.1, and 1.6, respectively. Caustics are closed concave curves, which are called "folds" that meet points, "cusps". In the case of the close topology $s < s_c$, the number of caustics is three, which are one central caustic close to the primary lens and two planetary caustics on either side of the system axis and opposite side of the planet (Right upper panel in Figure 2.5). The resonant topology is composed of one large resonant caustic, which is formed by putting a central caustic and one or two planetary caustics (Right middle panel in Figure 2.5). The wide topology is formed by one central caustic and one planetary caustic (Right bottom panel in Figure 2.5). It is also known that the total magnification of all the images in the binary lenses is $A \geq 3$ when the source gets inside the caustic (Witt & Mao, 1995).

2.1.4 Optical Depth and Event Rate

Optical depth

The microlensing optical depth, τ is the probability that a source star is being lensed by a foreground lens with impact parameter $u_0 \leq 1$ at any given time, which depends on how the masses are distributed along the line of sight,

$$\tau(D_{\rm S}) = \frac{4\pi G}{c^2}\int_0^{D_{\rm S}} \rho(D_{\rm L})\frac{D_{\rm L}(D_{\rm S}-D_{\rm L})}{D_{\rm S}}dD_{\rm L}, \tag{2.36}$$

where $\rho(D_{\rm L})$ is the mass density distribution of lenses along the line of sight at $D_{\rm L}$. Since optical depth does not depend on the lens mass function or kinematics, but only on mass density, its measurement allows us to study the mass distribution of stars and other interesting objects toward the Galactic bulge.

On the other hand, the microlensing optical depth can be interpreted as the fraction of the sky covered by the angular Einstein rings of total lenses, or, equivalently, the fraction of time that sources pass inside the Einstein ring. It can be estimated using the following formula derived by Udalski et al. (1994b),

$$\tau = \frac{\pi}{2N_{\rm S}\Delta T}\sum_i \frac{t_{{\rm E},i}}{\varepsilon(t_{{\rm E},i})}, \tag{2.37}$$

where $N_{\rm S}$ is the total number of observed source stars, ΔT is the duration of the survey in days, $t_{{\rm E},i}$ is the Einstein timescale of the ith event, and $\varepsilon(t_{{\rm E},i})$ is the detection efficiency at that Event timescale.

Event rate

The microlensing event rate, Γ, is the probability that a source star is magnified by a foreground lens star per unit of time, which is given by,

$$\frac{d^4\Gamma}{dD_{\rm L}dMd^2\boldsymbol{\mu}_{\rm rel}} = 2{D_{\rm L}}^2\theta_{\rm E}|\boldsymbol{\mu}_{\rm rel}|\rho(D_{\rm L})f(\boldsymbol{\mu}_{\rm rel})\phi(M), \tag{2.38}$$

where M is the lens mass, $n(D_{\rm L})$ is the number density of lenses, $f(\boldsymbol{\mu}_{\rm rel})$ is the two-dimensional probability density for a given lens–source relative proper motion $\boldsymbol{\mu}_{\rm rel}$, and $g(M)$ is the mass function of lenses (Batista et al., 2011). The event rate depends on the mass function of lenses and their kinematics.

From an observational standpoint, the event rate can also be calculated by using the detection efficiency for the event timescale,

$$\Gamma = \frac{1}{N_{\rm S}\Delta T}\sum_i \frac{1}{\varepsilon(t_{{\rm E},i})}. \tag{2.39}$$

To maximize the event rate, the microlensing survey is conducted toward dense stellar fields such as the Galactic bulge.

Observation results

Measuring the optical depth and event rate toward the Galactic bulge through a microlensing survey is an effective way to uncover the kinematics, mass function, and structure of the Galaxy, which can then be compared to those derived from Galactic models or other observations. Here are two results obtained by optical microlensing surveys toward the Galactic bulge.

Sumi et al. (2013) demonstrates the measurements of an event rate and an optical depth toward the Galactic bulge using two years of MOA-II survey data, covering an area of $\sim$ 42 square degrees. They found the event rate of $\Gamma = [2.39 \pm 1.1]e^{[0.60\pm0.05](3^\circ-|b|)} \times 10^{-5}{\rm star}^{-1}{\rm yr}^{-1}$ and the optical depth of $\tau_{t_{\rm E}<200{\rm days}} = [2.35 \pm 0.18]e^{[0.51\pm0.07](3^\circ-|b|)} \times 10^{-6}$ in the bulge fields with $|l| < 5^\circ$ using $\sim$ 430 bright microlensing events with well-defined microlensing parameters.

Mróz et al. (2019) also shows the result of the OGLE survey during $2010-2017$, covering 160 square degrees along the Galactic bulge ($|b| < 7^\circ, 0^\circ < l < 50^\circ, 190^\circ < l < 360^\circ$). They found the event rate of $\Gamma = [1.34 \pm 0.03]e^{[0.49\pm0.02](3^\circ-|b|)} \times 10^{-5}{\rm star}^{-1}{\rm yr}^{-1}$ and the optical depth of $\tau_{t_{\rm E}<200{\rm days}} = [1.36\pm0.04]e^{[0.40\pm0.03](3^\circ-|b|)} \times 10^{-6}$ in the bulge fields with $|l| < 3^\circ$ and $|b| > 2^\circ$ using the largest sample of $\sim 8,000$ microlensing events.

These optical surveys cannot measure the optical depth and the event rate towards the inner Galactic bulge close to the Galactic center $|b| < 2^\circ$ due to high extinction. Therefore some near-infrared surveys are conducted but there are still no measurements of microlensing event rates and planet frequency in the inner Galactic bulge (Section 2.3.3).

2.2 High order effects

From the observed microlensing light curve, we can get some parameters such as the Einstein radius crossing time $t_{\rm E}$, the mass ratio q, and the sky-projected angular separation s of the lens system. However only the Einstein radius crossing time $t_{\rm E}$ is related to the lens physical parameters: the lens distance $D_{\rm L}$, the lens mass $M_{\rm L}$, and the lens–source relative proper motion $\mu_{\rm rel}$,

$$t_{\rm E}(M_{\rm L}, D_{\rm L}, \mu_{\rm rel}) = \frac{\theta_{\rm E}}{\mu_{\rm rel}}. \tag{2.40}$$

In order to derive the physical parameters' additional effects, parallax (Gould, 1992; Alcock et al., 1995), terrestrial (Gould & Yee, 2013) or space-based parallax (Refsdal, 1966), finite source effects and/or detection of the light coming from the lens thanks to high angular resolution, see e.g. Kubas et al. (2012). Otherwise, we can get only the probability distribution of the physical parameters by the Bayesian analysis.

If both microlens parallax parameter $\pi_{\rm E}$ and finite-source effects parameter ρ, i.e. $\theta_{\rm E}$ see bellow, could be measured, we can determine the lens physical parameters by solving the following equations,

$$\theta_{\rm E}(M_{\rm L}, D_{\rm L}) = \sqrt{\kappa M_{\rm L} \pi_{\rm rel}}, \tag{2.41}$$

$$\pi_{\rm E}(M_{\rm L}, D_{\rm L}) = \sqrt{\frac{\theta_{\rm E}}{\kappa M_{\rm L}}}, \tag{2.42}$$

where $\kappa \equiv 4G/c^2{\rm au} \simeq 8.14{\rm mas}/M_\odot$, and $\pi_{\rm rel} = ({\rm au})/(1/D_{\rm L} - 1/D_{\rm S})$ is the relative lens-source parallax.

2.2.1 Finite source effects

The lens can be regarded as a point source when the angular size of the source is negligibly small compared to the angular separation of the source and the lens. However, this assumption breaks down in particular cases. For example, we cannot neglect the finite size of the source star when the lens star passes over the source star in single lens events (Choi et al., 2012) and we should consider that effect when the source star crosses or approaches closely to the caustic in binary lens events. This effect is called the finite source effect.

In the light curve modeling, the magnitude of finite source effects is parameterized by the angular size of the source in units of the angular Einstein radius,

$$\rho = \theta_* / \theta_{\rm E}, \tag{2.43}$$

where θ_* is the angular source star radius. For typical main-sequence sources in the Galactic bulge, ρ is of order 10^{-3}, whereas for typical giant source, ρ is of order 10^{-2}. When we consider the magnification with the finite source effects, we can obtain the total amplification by integrating $A(u)$ over the whole source area, weighted by the surface-brightness profile. If we assume that the source star has

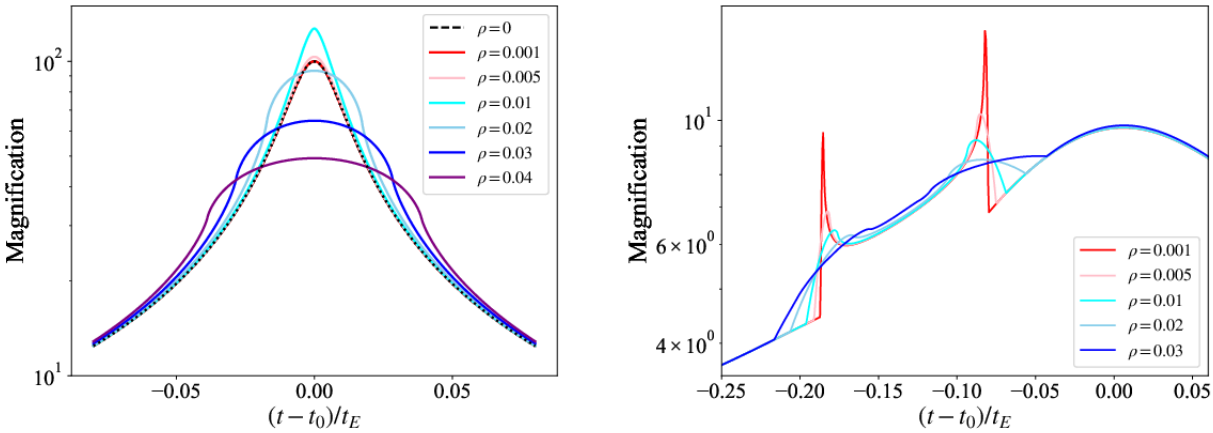

Figure 2.6: The light curves with different ρ values. The left panel shows the light curves of the single lens model with $u_0 = 0.01$. The black dot line shows the light curve assuming the source is a point source ($\rho = 0$) and the other color lines show the light curves assuming the source has a finite size. The right panel shows the light curves around the caustic crossing of the binary lens model with $q = 0.003$, $s = 1.1$, $\alpha = 220°$, and $u_0 = 0.1$.

uniform surface brightness, the magnification with the finite source effects is given by,

$$A_{\rm fin}(u|\rho) = \frac{\int_{A_{\rm source}} A(u)dA}{\int_{A_{\rm source}} dA} = \frac{1}{\pi\rho^2}\int_{A_{\rm source}} A(u)dA, \tag{2.44}$$

where $A_{\rm source}$ is the point source amplification over the source area (Lee et al., 2009). Especially when the lens is very close to the source center ($u \ll 1$), the magnification $A_{\rm fin}$ with finite source effects is given by,

$$A_{\rm fin}(u|\rho) = \frac{1}{\pi\rho^2}\int_0^{2\pi} d\theta \int_0^{\rho} d\tilde{\rho}\tilde{\rho}A[(x+\tilde{\rho}\cos\theta)^2 + (\tilde{\rho}\sin\theta)^2]. \tag{2.45}$$

Using the equation (2.18), we can change the equation (2.45),

$$A_{\rm fin}(u|\rho) = A(u)B(z);\ z \equiv \frac{u}{\rho}, \tag{2.46}$$

with

$$B(z) = \frac{z^2}{\pi}\int_0^{2\pi} d\theta \int_0^{1/z} d\tilde{z}\tilde{z}(1+\tilde{z}^2+2\tilde{z}\cos\theta)^{-1/2}, \tag{2.47}$$

where $B(z)$ means the ratio of the magnification with finite source effects to the magnification without finite source effects (Gould, 1994). When the separation between the center of the Einstein ring and the disk of the source is large ($z > 1$, or $u > \rho$), the magnification is similar to that without finite source effects ($B(z) \simeq 1$). However if $z \leq 2$, or $u \leq 2\rho$, we should consider the influence of the finite source effects. Figure 2.6 shows the light curves with the different ρ values for the light curves of the single lens model and the light curves around the caustic crossing of the binary lens model. The value of θ_* can be estimated empirically from the

observed source magnitude and color (Boyajian et al., 2014; Fukui et al., 2015). Therefore, $\theta_{\rm E}$ is obtained from the detection of the finite source effect and the lens-source relative proper motion $\mu_{\rm rel} = \theta_{\rm E}/t_{\rm E}$ is also measured.

2.2.2 Parallax effects

There are two effects causing three types of parallax effects. One effect is the motion of the observer, which causes "Orbital parallax effects". The other is the separation between two observers, which causes "Terrestrial parallax effects" and "Satellite parallax effects". The typical Einstein crossing time $t_{\rm E}$ is about 30 days and the observational scale of the Earth's rotation is 365 days. In order to detect the orbital parallax, the ratio of $t_{\rm E}$ to the earth's rotation should be large. On the other hand, the satellite parallax is an effective way to measure parallax, because the typical projected Einstein radii to the observer plane $\tilde{r}_{\rm E}$ is about 10 au, and for example, the separation between the earth and the *Spitzer* Space Telescope is about 1 au, which scales are better matched to measure the satellite parallax effects. Figure 2.7 shows the schematic views of orbital parallax effects and satellite parallax effects.

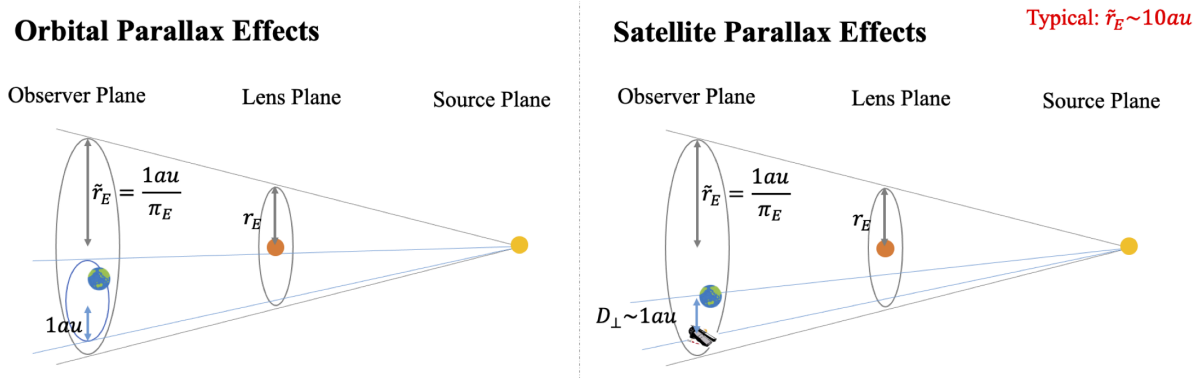

Figure 2.7: Schematic views of orbital parallax effects and space parallax effects. Orbital parallax measures the Einstein ring on a scale of the size of the Earth's orbit. On the other hand, Space parallax measures the Einstein ring on the scale of the projection distance between the Earth and a satellite.

Orbital Parallax

If the Earth's acceleration is not negligible during the microlensing event, the apparent trajectory of the deflector with respect to the line-of-sight becomes a cycloid rather than a linear line (assuming the orbit being nearly circular), yielding the asymmetric feature of the light curve. The magnification of the source star thereby becomes affected by the revolution of The earth around the Sun, providing an orbital parallax,

$$u(t) = \sqrt{\tau^2 + \beta^2}, \tag{2.48}$$

with

$$\tau = t_n + \delta\tau = \frac{t - t_0}{t_{\rm E}} + \delta\tau, \quad \beta = u_0 + \delta\beta, \tag{2.49}$$

where β is the component parallel to the lens trajectory, τ is the component perpendicular to the lens trajectory, and $\delta\tau$ and $\delta\beta$ is the deviation of the parallel component and perpendicular component from the impact parameter without parallax effects. Then $\delta\tau$ and $\delta\beta$ are given by,

$$\begin{aligned}(\delta\tau, \delta\beta) &= \boldsymbol{\pi}_{\rm E}\boldsymbol{\Delta}s, &(2.50)\\ &= (\boldsymbol{\pi}_{\rm E}\cdot\boldsymbol{\Delta}s, \boldsymbol{\pi}_{\rm E}\times\boldsymbol{\Delta}s), &(2.51)\\ &= (s_n(t)\pi_{{\rm E},N} + s_e(t)\pi_{{\rm E},E}, -s_n(t)\pi_{{\rm E},E} + s_e(t)\pi_{{\rm E},N}), &(2.52)\end{aligned}$$

where $\boldsymbol{\Delta}s$ is the positional offset of the Sun projected onto the sky, and $\boldsymbol{\pi}_{\rm E} = (\pi_{{\rm E},N}, \pi_{{\rm E},E})$ is the vector microlens parallax following the geocentric frame of Gould 2004. The microlens parallax $|\boldsymbol{\pi}_{\rm E}|$ is the size of the Earth's orbit ($\sim$ 1au) relative to the Einstein radius of the microlensing event projected onto the observer plane $\tilde{r}_{\rm E}$ as,

$$\pi_{\rm E} = \frac{1{\rm au}}{\tilde{r}_{\rm E}} = \frac{1{\rm au}}{\theta_{\rm E}}\left(\frac{1}{D_{\rm L}} - \frac{1}{D_{\rm S}}\right). \tag{2.53}$$

Terrestrial Parallax

The observations at the different locations on the Earth introduces a difference in the timing of the peak of light curves gathered at different longitudes. This is called the terrestrial parallax effect. Terrestrial parallax occurs because observatories located on different parts of the Earth have slightly different lines of sight toward the event and so observe slight differences in the impact parameters, u_0, and in the timing of the peak, t_0 (Hardy & Walker, 1995; Holz & Wald, 1996). To date, there have been two published terrestrial parallax mass measurements, OGLE-2007-BLG-224 (Gould et al., 2009) and OGLE-2008-BLG-279 (Yee et al., 2009), both of which are the extremely high magnification events.

Space Parallax

The idea of observing microlensing events from a satellite is proposed by Refsdal (1966). It should be a powerful way to constrain lens physical parameters. We can estimate the microlensing parallax by

$$\boldsymbol{\pi}_{\rm E} = \frac{\rm au}{D_\perp}(\Delta\tau, \Delta\beta), \tag{2.54}$$

with

$$\Delta\tau \equiv \frac{t_{0,{\rm Satellite}} - t_{0,\oplus}}{t_{\rm E}}, \ \Delta\beta \equiv \pm u_{0,{\rm Satellite}} - \pm u_{0,\oplus}, \tag{2.55}$$

where $D_\perp$ is the projected separation between a satellite and Earth at the time of the event. Generally, we have a four-fold degeneracy in the satellite parallax measurement due to the different signs of $(u_{0,\oplus}, u_{0,{\rm Satellite}}) = (+,+), (+,-), (-,+), (-,-)$ (Refsdal, 1966; Gould, 1994; Calchi Novati et al., 2015a).

2.2.3 Derive the lens physical parameters

By the detection of the finite source effects, we obtain the relation between the lens mass and the distance as,

$$M_{\rm L} = \frac{c^2}{4G}\theta_{\rm E}^2 \frac{D_{\rm S} D_{\rm L}}{D_{\rm S} - D_{\rm L}}. \tag{2.56}$$

where $D_{\rm L}$ is the lens distance and $M_{\rm L}$ is the lens mass.

By the detection of the parallax effects, we can also get the relation from the equation (2.53),

$$M_{\rm L} = \frac{c^2}{4G}\left(\frac{1{\rm au}}{\pi_{\rm E}}\right)^2 \frac{D_{\rm S} - D_{\rm L}}{D_{\rm S} D_{\rm L}}, \tag{2.57}$$

If both the finite source effects and the parallax effects can be detected, $D_{\rm L}$ and $M_{\rm L}$ can be determined,

$$M_{\rm L} = \frac{c^2}{4G}\frac{\theta_{\rm E}}{\pi_{\rm E}}, \tag{2.58}$$

$$D_{\rm L} = \left(\pi_{\rm E}\theta_{\rm E} + \frac{1}{D_{\rm S}}\right)^{-1}. \tag{2.59}$$

However, the number of events in which both effects are detected is quite a few ($\sim$ 30 %). As another method to constrain the lens physical parameters, the detection of the lens flux after the lens and the source are well separated is conducted. Actually, some high-resolution imaging follow-up observations by *Hubble Space Telescope* or Keck are conducted in order to detect the lens flux and to constrain the lens physical parameters of some important events (Bennett et al., 2006, 2007, 2015; Batista et al., 2014, 2015; Bhattacharya et al., 2017; Koshimoto et al., 2017; Bhattacharya et al., 2018).

2.3 Observation

2.3.1 Optical survey groups

Microlensing Observations in Astrophysics; MOA

The Microlensing Observations in Astrophysics (MOA; Bond et al., 2001; Sumi et al., 2003) collaboration conducts a microlensing exoplanet survey toward the Galactic bulge using the 1.8m MOA-II telescope, equipped with a 2.2 deg^2 wide field-of-view (FOV) CCD camera, known as MOA-cam3 (Sako et al., 2008), located at Mt. John Observatory in New Zealand. The MOA survey employs a custom wide-band filter, designated as $R_{\rm MOA}$, corresponding to a Cousins R- and I-band, as well as a V-band filter. Figure 2.8 shows a picture of the MOA-II telescope and the transmittance of the $R_{\rm MOA}$ and V-band filters.

Observations by the MOA-II telescope have been conducted since 2006. Figure 2.9 depicts the MOA-II observation fields and strategy prior to and subsequent to 2009 when the observation strategy was optimized in order to detect a greater

number of microlensing events. The MOA-II telescope's wide FOV enables the observation of expansive areas with high cadence, which is crucial for detecting short-duration anomalies on the light curve due to planets. Annually, the MOA-II survey discovers approximately $500 - 600$ microlensing events and $3 - 5$ planets.

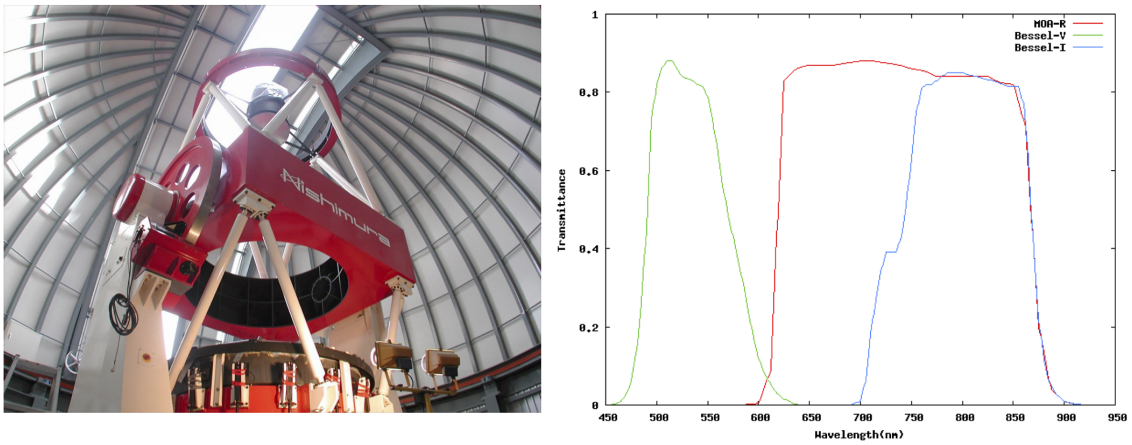

Figure 2.8: Left picture shows the MOA-II telescope. The right panel shows the transmittance of $R_{\rm MOA}$ and V-band filters.

The Optical Gravitational Lensing Experiment; OGLE

The Optical Gravitational Lensing Experiment (OGLE; Udalski, 2003) also conducts a microlensing survey at the Las Campanas Observatory in Chile. Currently, its forth phase, OGLE-IV (Udalski et al., 2015a) started its high-cadence survey in 2010 with a 1.4 deg^2 FOV CCD-camera. The OGLE survey finds $\sim 1800 - 2100$ microlensing events per year toward the Galactic bulge and Galactic plane.

Korea Microlensing Telescope Network; KMTNet

Korea Microlensing Telescope Network (KMT; Kim et al., 2018b) collaboration conducts a microlensing survey by using the three 1.6m telescopes with a 4.0 deg^2 FOV CCD-camera at Cerro Tololo Interamerican Observatory in Chile (KMTC), South African Astronomical Observatory in South Africa (KMTS), and Siding Spring Observatory in Australia (KMTA). The KMT survey finds $\sim$ 2200 microlensing events per year. With three telescopes in separate locations, most of the light curves can be observed with no time gaps.

2.3.2 *Spizer* microlensing campaign

The *Spitzer* Space Telescope is one of the missions of NASA's Great Observatories Program and was launched in 2003. *Spitzer* is located at the Earth-trailing orbit around the Sun. As part of a six-year ($2014 - 2019$) program, *Spitzer* had observed almost 1100 microlensing events toward the Galactic bulge (Gould & Yee, 2013; Gould et al., 2014, 2015a,b, 2016, 2018) with the primary objectives

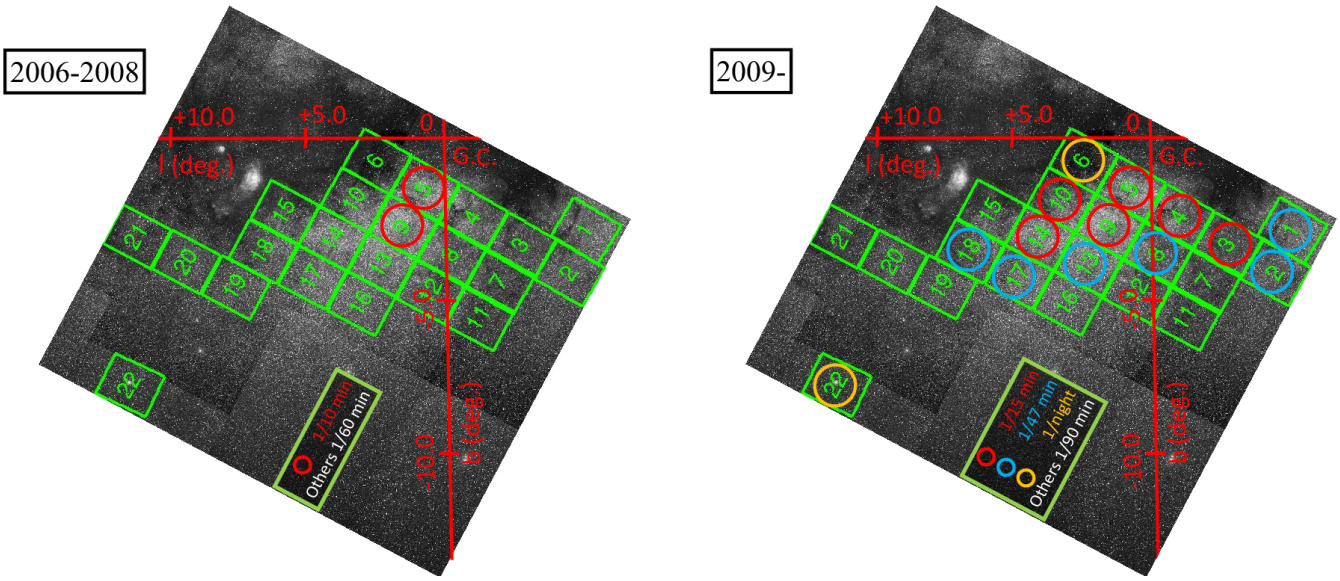

Figure 2.9: Observation fields and strategy of the MOA microlensing survey. During the 2006 − 2009 period, gb5 and gb9 were observed once per 10 minutes and others were once per 1 hour. Then since 2009, gb3, gb4, gb5, gb9, and gb10 are observed once per 15 minutes, gb1, gb2, gb8, gb13, gb17, and gb18 are once per 47 minutes, gb6 and gb22 are once per night, and the other fields are once per 95 minutes. The total field area is about 50 deg^2.

of measuring the mass of planets via space parallax, and reveal the dependence of planet frequency on the Galactic components and location. Observations with the *Spitzer* have allowed us to place limits on the masses of more than a dozen planetary events. Comparing the planet distributions in the disk to that in the bulge will reveal the difference in the planet formation process in the different environments.

2.3.3 NIR microlensing surveys

Microlensing Survey by the United Kingdom Infrared Telescope (UKIRT)

From 2015 to 2018, the UKIRT Microlensing Survey (Shvartzvald et al., 2017a) conducted a microlensing exoplanet survey towards the inner Galactic bulge by using the UKIRT 3.8 m telescope on Mauna Kea, Hawaii with a 0.8 deg^2 FOV IR camera, the Wide Field Camera (WFCAM). The UKIRT microlensing survey was conducted in H- and K-band filters. UKIRT-2017-BLG-001Lb (Shvartzvald et al., 2018) is the first planet discovered in close proximity to the Galactic center. The event is located at Galactic coordinates $(l, b) = (-0.12°, -0.33°)$ and suffers from high extinction of $A_K = 1.68$. The UKIRT survey demonstrated that operating at NIR wavelengths enables us to discover planets close to the Galactic center with high extinction.

Microlensing events by the VISTA Variables in the Via Lactea Survey (VVV)

The VISTA Variables in the Via Lactea Survey (VVV; Minniti et al., 2010) conducted a NIR microlensing survey close to the inner Galactic bulge by using the Visible and Infrared Survey Telescope for Astronomy (VISTA), a 4 m telescope with a 1.6 $\deg^2$ wide-field VISTA InfraRed Camera (VIRCAM, Emerson & Sutherland, 2010) at ESO's Cerro Paranal Observatory in Chile. The VVV observational schedule includes single-epoch photometry in Z, Y, J, H, and K_S bands and variability campaign in K_S-band (Minniti et al., 2010). Although the VVV survey cadence (once per night) is inadequate to routinely detect microlensing events with short timescales that should be numerous in the Galactic center region (Gould, 1995), this is sufficient to reveal the galactic longitude dependence and the galactic latitude dependence of the number of microlensing events toward the galactic center. They show the galactic longitude distribution ($-10.0 < l < 10.44$) using 630 microlensing events during $2010 - 2015$ (Navarro et al., 2018) and the galactic latitude distribution ($-3.7 < b < 3.9$) using 360 microlensing events (Navarro et al., 2020).

PRime-focus Infrared Microlensing Experiments; PRIME

The PRIME telescope has one of the largest fields of view in the near-infrared ($1.45\deg^2$) and will conduct microlensing exoplanet search in the near-infrared. The near-infrared has the following advantages over conventional visible-light surveys: the number of planets discovered will increase due to the ability to observe regions of high star density near the Galactic center, where interstellar attenuation is strong, the number of low-mass planets is also expected to increase due to the increased detection sensitivity, and the number of planets discovered is expected to increase to $42 - 52$/year, more than 10 times higher than that of conventional visible light observations (Kondo et al. 2023 in preparation).

The main goals of the PRIME microlensing survey are to measure the microlensing event rate in the inner Galactic bulge to help design the observing strategy for *Roman*'s microlensing survey and to make the first statistical measurement of exoplanet demographics in the central bulge fields where optical observations are challenging owing to the high extinction in these fields. By comparing with the planet frequency measured by visible observation, PRIME will verify the difference in planet frequency by the Galactic environment.

The PRIME telescope was installed in SAAO in the summer of 2022 and achieved its first light in July with an optical test camera (z-band). Then in October the installation of a wide-field near-infrared camera, PRIME-cam, was performed and its first light by the PRIME-Cam was achieved. Although we are still in the commissioning phase, PRIME will start microlensing survey observations in the middle of 2023. Figure 2.10 shows the pictures during the installation of the PRIME telescope and PRIME-Cam.

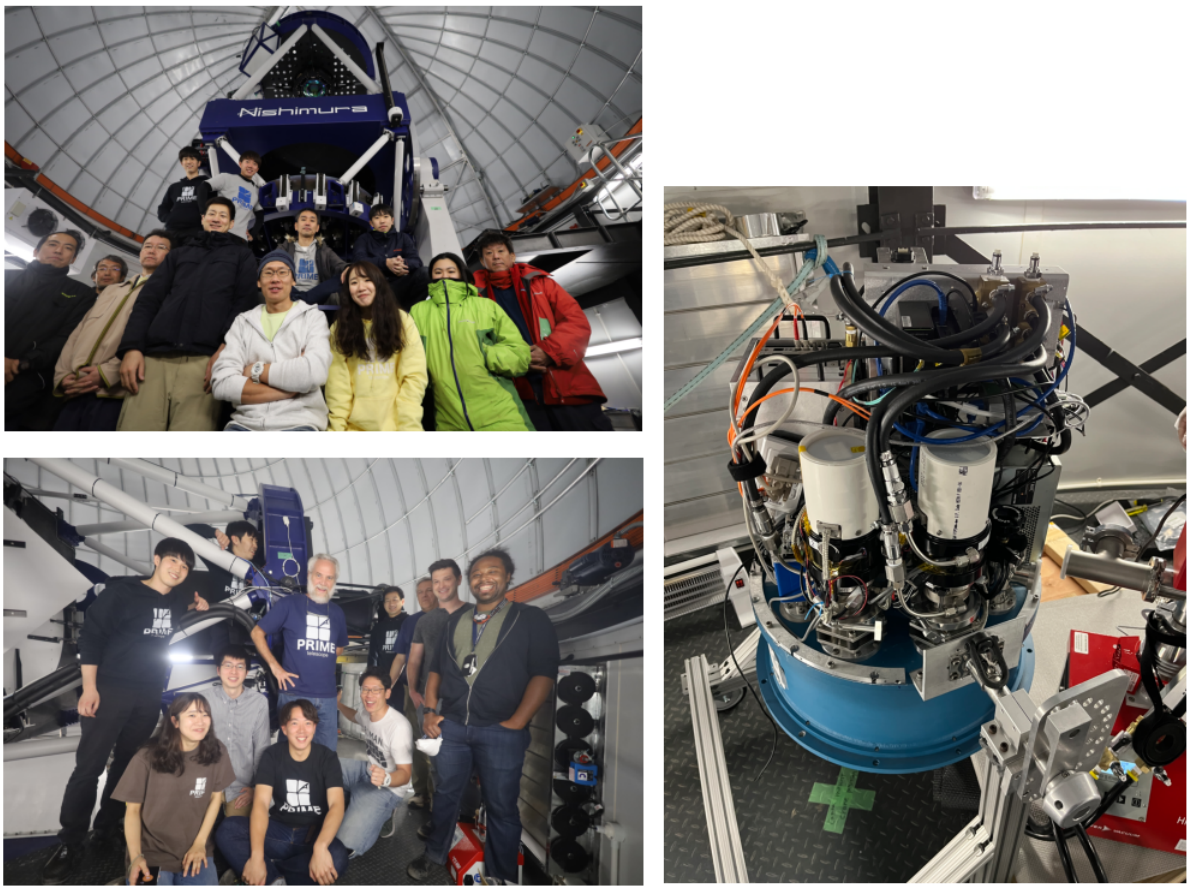

Figure 2.10: Group pictures and pictures of the PRIME telescope and PRIME-Cam. The upper left picture shows the PRIME telescope after its installation of the telescope in July 2022, with members of Osaka university and the Nishimura factory. The lower left picture shows the group picture with NASA members and the PRIME telescope mounted with PRIME-Cam in October 2022. The right picture shows the PRIME-Cam.

Nancy Grace Roman Space Telescope

Nancy Grace Roman Space Telescope is NASA's flagship mission (Spergel et al., 2015) following the *James Webb Space Telescope* (JWST), which is planned to launch in 2027. It is located at a halo orbit around the second Sun-Earth Lagrange Point (L2). The main purposes are to study dark energy and to conduct exoplanet searches by the microlensing survey. *Roman* is a 2.4 m space telescope with a 0.281 deg^2 FOV NIR imaging and spectroscopy and a coronagraph. In order to conduct a microlensing survey, *Roman* will use a wide W149 filter ($\sim 1-2\mu$m) at 15 minutes cadence for 6 seasons of 72 days each. *Roman* is expected to detect $\sim$ 1400 cold exoplanets with mass greater than that of Mars ($\sim 0.1M_\oplus$). Thanks to the high photometric accuracy, it has sensitivity to small mass objects such as Mercury ($\sim 0.05M_\oplus$) and Ganymede ($\sim 0.02M_\oplus$) (Penny et al., 2019). The predicted sensitivity of the *Roman* microlensing survey is shown in Figure 2.11.

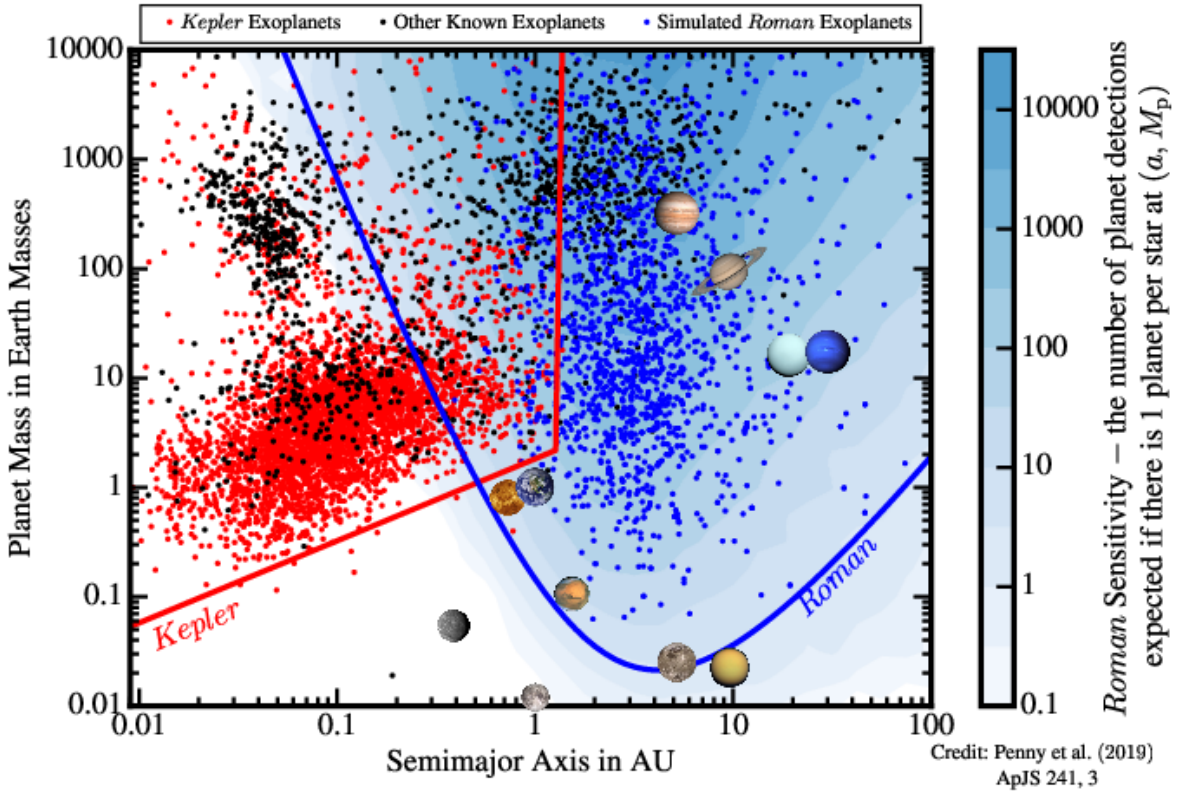

Figure 2.11: The *Roman* microlensing survey's predicted sensitivity (Penny et al., 2019). The blue line indicates the *Roman* planet detection limit. The red line indicates the *Kepler* planet detection limit based on Burke et al. (2015). Blue dots show the simulated planets, which are detected by the *Roman* microlensing survey. Red dots show the candidate and confirmed planets by *Kepler*. Black dots show all other detected planets.

Johnson et al. (2020) shows that *Roman* will detect $\sim$ 250 free-floating planets with masses down to that of Mars, including $\sim$ 60 with a mass of $\leq 1 M_{\oplus}$.

Chapter 3

OGLE-2018-BLG-1185b : A Low-Mass Microlensing Planet Orbiting a Low-Mass Dwarf

We report an analysis of the planetary microlensing event OGLE-2018-BLG-1185, which was observed by a large number of ground-based telescopes and by the *Spitzer* Space Telescope. The ground-based light curve indicates a low planet-host star mass ratio of $q = (6.9 \pm 0.2) \times 10^{-5}$, which is near the peak of the wide-orbit exoplanet mass-ratio distribution. We estimate the host star and planet masses with a Bayesian analysis using the measured angular Einstein radius under the assumption that stars of all masses have an equal probability to hosting the planet. The flux variation observed by *Spitzer* is marginal, but still places a constraint on the microlens parallax. Imposing a conservative constraint that this flux variation should be $\Delta f_{\rm Spz} < 4$ instrumental flux units yields a host mass of $M_{\rm host} = 0.37^{+0.35}_{-0.21}\ M_\odot$ and a planet mass of $m_{\rm p} = 8.4^{+7.9}_{-4.7}\ M_\oplus$. A Bayesian analysis including the full parallax constraint from *Spitzer* suggests smaller host star and planet masses of $M_{\rm host} = 0.091^{+0.064}_{-0.018}\ M_\odot$ and $m_{\rm p} = 2.1^{+1.5}_{-0.4}\ M_\oplus$, respectively. Future high-resolution imaging observations with *Hubble* Space Telescope or Extremely Large Telescope could distinguish between these two scenarios and help reveal the planetary system properties in more detail.

3.1 Introduction

The gravitational microlensing method has a unique sensitivity to low-mass planets (Bennett & Rhie, 1996) beyond the snow line of the host star (Gould & Loeb, 1992), where, according to core accretion theory predictions, planet formation is most efficient (Lissauer, 1993; Pollack et al., 1996). The Microlensing Observations in Astrophysics (MOA) Collaboration (Bond et al., 2001; Sumi et al., 2003) presented the most complete statistical analysis of planets found by microlensing to date and the best measurement of the planet distribution beyond the snow line in Suzuki et al. (2016). They found that the mass-ratio distribution from the $2007 - 2012$ MOA-II microlensing survey combined with earlier samples (Gould et al., 2010;

Cassan et al., 2012) is well fitted by a broken power-law model.

Their result shows the mass-ratio distribution peaks at $q_{\rm br} = (6.7^{+9.0}_{-1.8}) \times 10^{-5}$ with power-law slopes of $n = -0.85^{+0.12}_{-0.13}$ and $p = 2.6^{+4.2}_{-2.1}$ above and below $q_{\rm br}$, respectively[1]. This result is consistent with previous microlensing analyses, which suggest that Neptune-mass-ratio planets are more common than larger gas giants (Gould et al., 2006; Sumi et al., 2010), and further indicates that Neptune-mass-ratio planets are, in fact, the most common type of planet (large or small) in wide orbits.

Additionally, Suzuki et al. (2018) revealed a disagreement between the measured mass-ratio distribution in Suzuki et al. (2016) and the predictions of the runaway gas accretion scenario (Ida & Lin, 2004), which is part of the standard core accretion theory. Population synthesis models based on core accretion, including runaway gas accretion, predict too few planets in the mass range of approximately $20 - 80 M_\oplus$ compared to those inferred from microlensing observations. Similar tension is indicated by Atacama Large Millimeter/submillimeter Array (ALMA) observations. Nayakshin et al. (2019) compared the wide-orbit (9-99 au) planet candidates with masses of $0.01 M_{\rm Jup}$ to a few $M_{\rm Jup}$ suggested by ALMA protoplanetary disk observations to a population synthesis prediction from the runaway gas accretion scenario. They found that the scenario predicts fewer sub-Jovian planets than the ALMA observations inferred. Three-dimensional hydrodynamical simulations of protoplanetary disks do not support the runaway gas accretion scenario either (Lambrechts et al., 2019).

The peak position of the mass-ratio function and its slope at low-mass ratios are uncertain due to the lack of planets with mass ratios of $q < 5.8 \times 10^{-5}$ in the Suzuki et al. (2016) sample. Udalski et al. (2018) and Jung et al. (2019a) used samples of published planets to refine the estimates of the peak and the low mass-ratio slope of the mass-ratio function. Udalski et al. (2018) confirmed the turnover shown in Suzuki et al. (2016) and obtained the slope index in the low-mass regime, $p \sim 0.73$, using seven published planets with $q < 1 \times 10^{-4}$. Jung et al. (2019a) found $q_{\rm br} \simeq 0.55 \times 10^{-4}$ using 15 published planets with low-mass ratios ($q < 3 \times 10^{-4}$). The Jung et al. (2019a) study was subject to "publication bias". That is, the planets were not part of a well-defined statistical sample. Instead, these planets were selected for publication for reasons that are not well characterized. Nevertheless, the authors make the case that this publication bias should not be large enough to invalidate their results. By contrast, the Udalski et al. (2018) study only made the implicit assumption that all planets with $q < 1 \times 10^{-4}$ (and greater than that of the actual published planet) would have been published. If this is true (which is very likely), the study is not subject to publication bias.

A more definitive improvement of the Suzuki et al. (2016) mass-ratio function can be obtained with an extension of the MOA-II statistical sample to include additional microlensing seasons (D. Suzuki et al., in preparation). The low-mass-

[1]These values are the median and 68% confidence level by the Markov Chain Monte Carlo analysis with a 30-planet sample, which is given in Table 5 of Suzuki et al. (2016). So the 1σ range of the mass-ratio distribution peaks is roughly $q_{\rm br} \sim (0.5 - 2) \times 10^{-4}$. At the same time, they also show that the best fitting parameters are $q_{\rm br} = 1.65 \times 10^{-4}$ with power-law slopes of $n = -0.92$ and $p = 0.47$ in Table 4 of Suzuki et al. (2016).

ratio planet analyzed in this paper, OGLE-2018-BLG-1185Lb, will be part of that extended sample, and it will contribute to an improved characterization of the low end of the wide-orbit exoplanet mass-ratio function.

The statistical analysis of the wide-orbit planet population can also be improved by including information on the lens physical parameters, such as the lens mass, $M_{\rm L}$, and the distance to the lens star, $D_{\rm L}$. While the lens planet-host mass ratios, q, are usually well constrained from the light-curve modeling, we need at least two mass-distance relations in order to derive $M_{\rm L}$ and $D_{\rm L}$ directly. There are three observables that can yield mass-distance relations: finite source effects, microlens parallax effects, and direct detection of the lens flux.

In recent years, lens flux detection by high-resolution imaging follow-up observations (such as by the *Hubble Space Telescope* (*HST*) or Keck) has been done for several microlens planetary systems after the lens and the source are separated enough to be detected (Bennett et al., 2006, 2007, 2015, 2020; Batista et al., 2014, 2015; Bhattacharya et al., 2017, 2018; Koshimoto et al., 2017; Vandorou et al., 2020). However, the required separation for resolving the lens and source depends on their relative brightnesses, and even if they are comparable in brightness, it typically takes a few years for them to separate sufficiently.

If both the Einstein radius $\theta_{\rm E}$ from the finite source effect and the microlens parallax $\pi_{\rm E}$ from the parallax effect are measured, we can derive two mass-distance relations as follows:

$$M_{\rm L} = \frac{c^2}{4G}{\theta_{\rm E}}^2 \frac{D_{\rm S} D_{\rm L}}{D_{\rm S} - D_{\rm L}} = \frac{c^2}{4G}\frac{\rm au}{{\pi_{\rm E}}^2}\frac{D_{\rm S} - D_{\rm L}}{D_{\rm S} D_{\rm L}}, \tag{3.1}$$

where $D_{\rm S}$ is the distance to the source (Gould, 1992, 2000). Finite source effects are detected in most planetary-lens events through the observation of a caustic crossing or a close approach to a caustic cusp, thus enabling the measurement of $\theta_{\rm E}$.

The most common method for measuring the microlens parallax has been via the effects of the motion of the observer, which is called the orbital parallax effect. In order to detect the orbital parallax, the ratio of $t_{\rm E}$ (typically $t_{\rm E}$ is ~ 30 days) to Earth's orbital period (365 days) should be significant. Thus, we only measure the orbital parallax effect for microlensing events with long durations and/or with relatively nearby lens systems, yielding mass measurements in less than half of published microlensing planetary systems.

The most effective method for routinely obtaining a microlens parallax measurement is via the satellite parallax effect (Refsdal, 1966), which is caused by the separation between two observers. Because the typical Einstein radius projected onto the observer plane, $\tilde{r}_{\rm E}$, is about 10 au, the satellite parallax effect can be measured for a wide range of microlenses provided the separation between Earth and the satellite is about 1 au (as was the case for *Spitzer*).

For the purpose of measuring the Galactic distribution of planets and making mass measurements through the satellite parallax effect, the *Spitzer* microlensing campaign was carried out from 2014–2019 (Gould & Yee, 2013; Gould et al., 2014, 2015a,b, 2016, 2018). During the six-year program, close to 1000 microlensing events were simultaneously observed from the ground and by *Spitzer*, and there are

11 published[2] planets with satellite parallax measurements from *Spitzer*: OGLE-2014-BLG-0124Lb (Udalski et al., 2015b), OGLE-2015-BLG-0966Lb (Street et al., 2016), OGLE-2016-BLG-1067Lb (Calchi Novati et al., 2019), OGLE-2016-BLG-1195Lb (Shvartzvald et al., 2017b), OGLE-2016-BLG-1190Lb (Ryu et al., 2018), OGLE-2017-BLG-1140Lb (Calchi Novati et al., 2018), TCP J05074264+2447555 (Nucita et al., 2018; Fukui et al., 2019; Zang et al., 2020a), OGLE-2018-BLG-0596Lb (Jung et al., 2019b), KMT-2018-BLG-0029Lb (Gould et al., 2020), OGLE-2017-BLG-0406Lb (Hirao et al., 2020), and OGLE-2018-BLG-0799Lb (Zang et al., 2022b). Comparison of planet frequency in the disk to that in the bulge could probe the effects of the different environments on the planet formation process.

Obvious correlated noise in *Spitzer* photometry was first noted by Poleski et al. (2016) and Zhu et al. (2017), but those works did not expect the systematic errors would have a significant effect on the parallax measurements. Indeed, two comparisons of small, heterogeneous samples of published *Spitzer* microlensing events confirmed this expectation (Shan et al., 2019; Zang et al., 2020b). However, a larger study (Koshimoto & Bennett, 2020) of the 50-event statistical sample of Zhu et al. (2017) indicated a conflict between the *Spitzer* microlensing parallax measurements and Galactic models. They suggested that this conflict was probably caused by systematic errors in *Spitzer* photometry. Based, in part, on the Koshimoto & Bennett (2020) analysis, the *Spitzer* microlensing team has made a greater effort to understand these systematic errors, including obtaining baseline data in 2019 for many of the earlier planetary events. These additional baseline data proved very useful in the characterization of systematics in *Spitzer* photometry for three previously published events (Gould et al., 2020; Hirao et al., 2020; Zang et al., 2022b). Those analyses show that systematics in *Spitzer* photometry can be present at the level of 1–2 instrumental flux units, so observed signals in *Spitzer* photometry on those scales should be interpreted with caution.

In this chapter, we present an analysis of the planetary microlensing event OGLE-2018-BLG-1185, which was simultaneously observed by many ground-based telescopes and by the *Spitzer* Space Telescope. From the ground-based light-curve analysis, the planet-host star mass ratio turns out to be very low, $q \sim 6.9 \times 10^{-5}$, which is thought to be near the peak of the wide-orbit exoplanet mass-ratio distribution in Suzuki et al. (2016), Udalski et al. (2018), and Jung et al. (2019a). Section 3.2 explains the observations and the data reductions. Our ground-based light-curve modeling method and results are shown in Section 3.3. In Section 3.4, we derive the angular Einstein radius from the source magnitude and color and the finite source effect in order to constrain the physical parameters of the planetary system. In Section 3.5, we estimate the physical properties such as the host star and planet masses based on the ground-based light curve alone by performing a Bayesian analysis using the measured angular Einstein radius under the assumption that stars of all masses have an equal probability of hosting the planet. We present our parallax analysis including the *Spitzer* data in Section 3.6. Finally, we discuss the analysis and summarize our conclusions in Section 4.6.

[2]In addition Yee et al. (2021) have submitted a paper on OGLE-2019-BLG-0960.

3.2 Observations and Data Reductions

3.2.1 Ground-based Survey Observations

The microlensing event OGLE-2018-BLG-1185 was first discovered on 2018 July 7 ($\mathrm{HJD}' = \mathrm{HJD} - 2450000 \sim 8306$), at the J2000 equatorial coordinates (RA, Dec) = ($17^h\ 59^m\ 10^s.26, -27^\circ\ 50'\ 06''.3$) corresponding to Galactic coordinates $(l, b) = (2.465^\circ, -2.004^\circ)$ by the Optical Gravitational Lensing Experiment (OGLE) Collaboration (Udalski, 2003). The OGLE Collaboration conducts a microlensing survey using the 1.3m Warsaw telescope with a 1.4 deg^2 field-of-view (FOV) CCD camera at Las Campanas Observatory in Chile and distributes alerts of the discovery of the microlensing events by the OGLE-IV Early Warning System (Udalski et al., 1994a; Udalski, 2003). The event is located in the OGLE-IV field BLG504, which is observed with a cadence of one observation per hour.

The event was also discovered independently on 2018 July 9 by the MOA Collaboration and identified as MOA-2018-BLG-228 by the MOA alert system (Bond et al., 2001). The MOA Collaboration conducts a microlensing exoplanet survey toward the Galactic bulge using the 1.8m MOA-II telescope with a 2.2 deg^2 wide FOV CCD camera, MOA-cam3 (Sako et al., 2008), at the University of Canterbury's Mount John Observatory in New Zealand. The MOA survey uses a custom wideband filter referred to as R_{MOA}, corresponding to the sum of the Cousins R- and I-bands and also uses a Johnson V-band filter. The event is located in the MOA field gb10, which is observed at a high cadence of one observation every 15 minutes. The Korea Microlensing Telescope Network (KMTNet) Collaboration (Kim et al., 2016) conducts a microlensing survey using three 1.6m telescopes each with a 4.0 deg^2 FOV CCD camera. The telescopes are located at Cerro Tololo Interamerican Observatory (CTIO) in Chile (KMTC), South African Astronomical Observatory (SAAO) in South Africa (KMTS), and Siding Spring Observatory (SSO) in Australia (KMTA). This event is located in an overlapping region between two fields (KMTNet BLG03 and BLG43) and was identified by the KMTNet EventFinder (Kim et al., 2018a) as KMT-2018-BLG-1024.

3.2.2 *Spitzer* Observations

In order to construct statistical samples from the *Spitzer* microlensing campaign, Yee et al. (2015) established detailed protocols for the selection and observational cadence of *Spitzer* microlensing targets. On 2018 July 8 ($\mathrm{HJD}' \sim 8308.25$), OGLE-2018-BLG-1185 was selected as a "Subjective, Immediate" (SI) target to be observed with the "objective" cadence by the *Spitzer* microlensing team. The selection as SI meant that this event was observed even though it never met the objective criteria established in Yee et al. (2015). The *Spitzer* Space Telescope began to observe this event on 2018 July 14 ($\mathrm{HJD}' \sim 8313.83$), which was 3 days after the peak observed from the ground-based telescopes. The objective cadence resulted in approximately one observation per day for the remainder of the observing window (27 days total). These observations were taken with the Infrared Array Camera in the 3.6 μm (L) band.

3.2.3 Ground-based Follow-up Observations

After the event was selected for *Spitzer* observations, some ground-based follow-up observations were conducted. The Microlensing Network for the Detection of Small Terrestrial Exoplanets (MiNDSTEp) used the 1.54m Danish Telescope at La Silla Observatory in Chile and the 0.6m telescope at Salerno University Observatory in Italy. The Microlensing Follow-Up Network (μFUN) used the 1.3m SMARTS telescope at CTIO in Chile. Las Cumbres Observatory (LCO; Brown et al., 2013) used the 1.0m telescopes at CTIO in Chile, at SSO in Australia, and at SAAO in South Africa, as part of an LCO-*Spitzer* program. The ROME/REA team (Tsapras et al., 2019) also used the 1.0m LCO robotic telescopes at CTIO in Chile, at SSO in Australia, and at SAAO in South Africa. A summary of observations from each telescope is given in Table 3.1.

3.2.4 Data Reduction

The OGLE, MOA, and KMTNet data were reduced using the OGLE Difference Image Analysis (DIA) photometry pipeline (Udalski, 2003), the MOA DIA photometry pipeline (Bond et al., 2001), and the KMTNet pySIS photometry pipeline (Albrow et al., 2009), respectively. The MiNDSTEp data were reduced using DanDIA (Bramich, 2008; Bramich et al., 2013). μFUN data were reduced using DoPHOT (Schechter et al., 1993), and LCO data from the LCO-*Spitzer* program were reduced using a modified ISIS package (Alard & Lupton, 1998; Alard, 2000; Zang et al., 2018). The LCO data obtained by the ROME/REA team were reduced using a customized version of the DanDIA photometry pipeline. The *Spitzer* data were reduced using the photometry algorithm described in Calchi Novati et al. (2015b).

It is known that the photometric error bars calculated by the data pipelines can be underestimated (or more rarely overestimated). Various factors, such as observational conditions, can cause systematic errors. In order to get proper errors of the parameters in the light-curve modeling, we empirically normalize the error bars by using the standard method of Bennett et al. (2008). We use the formula

$$\sigma_i' = k\sqrt{\sigma_i^2 + e_{\rm min}^2}, \tag{3.2}$$

where σ_i' is the ith renormalized error, σ_i is the ith error obtained from DIA, and k and $e_{\rm min}$ are the renormalizing parameters. We set the value of $e_{\rm min}$ to account for systematic errors that dominate at high magnification, and we adjust the value of k to achieve $\chi^2/{\rm dof} = 1$. The data from Salerno, LCO SAAO by the LCO-Spitzer program, LCO SSO and SAAO by the ROME/REA project are too few to give any significant constraint or show systematics and disagreement with other data sets. Therefore, we do not use them for the modeling. We list the calculated error bar renormalization parameters in Table 3.1.

Table 3.1: The number of data points in the light curves and the normalization parameters

Name	Site	Collaboration	Aperture(m)	Filter	k	$e_{\rm min}$	$N_{\rm use}/N_{\rm obs}$
OGLE	Chile	OGLE	1.3	I	1.660	0.003	3045/3045
OGLE	Chile	OGLE	1.3	V	1.301	0.003	68/68
MOA	New Zealand	MOA	1.8	$R_{\rm MOA}$	1.650	0.003	7277/7509
MOA	New Zealand	MOA	1.8	V	1.321	0.003	240/240
KMT SSO f03	Australia	KMTNet	1.6	I	1.900	0.003	2087/2706
KMT SSO f43	Australia	KMTNet	1.6	I	1.824	0.003	2080/2658
KMT CTIO f03	Chile	KMTNet	1.6	I	1.579	0.003	2304/2486
KMT CTIO f43	Chile	KMTNet	1.6	I	1.443	0.003	2195/2363
KMT SAAO f03	South Africa	KMTNet	1.6	I	2.444	0.003	1813/2096
KMT SAAO f43	South Africa	KMTNet	1.6	I	1.900	0.003	1846/2078
Danish	Chile	MiNDSTEp	1.54	Z	1.015	0.003	139/154
Salerno	Italy	MiNDSTEp	0.6	I			0/5
LCO SSO	Australia	LCO-*Spitzer*	1.0	i'	2.528	0.003	31/44
LCO CTIO	Chile	LCO-*Spitzer*	1.0	i'	1.129	0.003	17/17
LCO SAAO	South Africa	LCO-*Spitzer*	1.0	i'			0/19
CTIO 1.3m	Chile	μFUN	1.3	I	0.852	0.003	18/18
CTIO 1.3m	Chile	μFUN	1.3	V	0.566	0.003	3/3
LCO SSO	Australia	ROME/REA	1.0	g			0/25
LCO SSO	Australia	ROME/REA	1.0	i'			0/74
LCO SSO	Australia	ROME/REA	1.0	r			0/29
LCO CTIO	Chile	ROME/REA	1.0	g	1.110	0.003	33/33
LCO CTIO	Chile	ROME/REA	1.0	i'	1.589	0.003	61/61
LCO CTIO	Chile	ROME/REA	1.0	r	1.337	0.003	31/31
LCO SAAO	South Africa	ROME/REA	1.0	g			0/17
LCO SAAO	South Africa	ROME/REA	1.0	i'			0/19
LCO SAAO	South Africa	ROME/REA	1.0	r			0/45
Spitzer	Earth-trailing orbit	*Spitzer*	0.85	L	2.110	...	26/26

3.3 Ground-based Light Curve Analysis

3.3.1 Binary-lens model

The magnification of the binary lens model depends on seven parameters: the time of lens-source closest approach, t_0; the Einstein radius crossing time $t_{\rm E}$; the impact parameter in units of the Einstein radius, u_0; the planet-host mass ratio q; the planet-host separation in units of the Einstein radius, s; the angle between the trajectory of the source and the planet-host axis, α; and the ratio of the angular source size to the angular Einstein radius, ρ. The model flux $f(t)$ of the magnified source at time t is given by

$$f(t) = A(t)f_S + f_b, \tag{3.3}$$

where $A(t)$ is the magnification of the source star, and f_S and f_b are the unmagnified flux from the source and the flux from any unresolved blend stars, respectively.

We also adopt a linear limb-darkening model for the source star,

$$S_\lambda(\vartheta) = S_\lambda(0)[1 - u_\lambda(1 - \cos(\vartheta))], \tag{3.4}$$

where $S_\lambda(\vartheta)$ is the limb-darkened surface brightness. The effective temperature of the source star estimated from the extinction-free source color presented in Section 3.4 is $T_{\rm eff} \sim 5662$K (González Hernández & Bonifacio, 2009). Assuming a surface gravity $\log g = 4.5$ and a metallicity of $\log[M/H] = 0$, we select the limb-darkening coefficients of $u_I = 0.5494$, $u_V = 0.7105$, $u_R = 0.6343$, $u_Z = 0.6314$, $u_g = 0.7573$, $u_r = 0.6283$ and $u_i = 0.5389$ from the ATLAS model (Claret & Bloemen, 2011). For the $R_{\rm MOA}$ passband, we use the coefficient for $u_{Red} = 0.5919$, which is the mean of u_I and u_R.

We first conducted the light-curve fitting with only ground-based data. We employed a Markov Chain Monte Carlo algorithm (Verde et al., 2003) combined with the image-centered ray-shooting method (Bennett & Rhie, 1996; Bennett, 2010). We conducted grid search analysis following the same procedure in Kondo et al. (2019). First, we performed a broad grid search over (q, s, α) space with the other parameters free. The search ranges of q, s, and α are $-6 < \log q < 0$, $-0.5 < \log s < 0.6$, and $0 < \alpha < 2\pi$, with 11, 22, and 40 grid points, respectively. Next, we refined all parameters for the best 100 models with the smallest χ^2 to search for the global best-fit model. The parameters of the best-fit models are summarized in Table 3.2. The light curve and the caustic geometry are shown in Figure 3.1 and Figure 3.2. As a result of the grid search, we found that the best-fit binary-lens model is favored over the single-lens model by $\Delta\chi^2 \sim 2330$. The bottom panels in Figure 3.1 show the clear deviations of the light curve with respect to the single-lens model from HJD$' \sim 8310.9$ to ~ 8311.8, which are well fitted by the approach to the central caustic for the best binary-lens model. Although the additional magnification from the cusp approach to the planetary caustic is small, the asymmetric feature on the right side of the light curve due to the approach to the central caustic shows clear residuals from the single-lens model, which suggest the existence of a companion. The best binary-lens model suggests that the lens

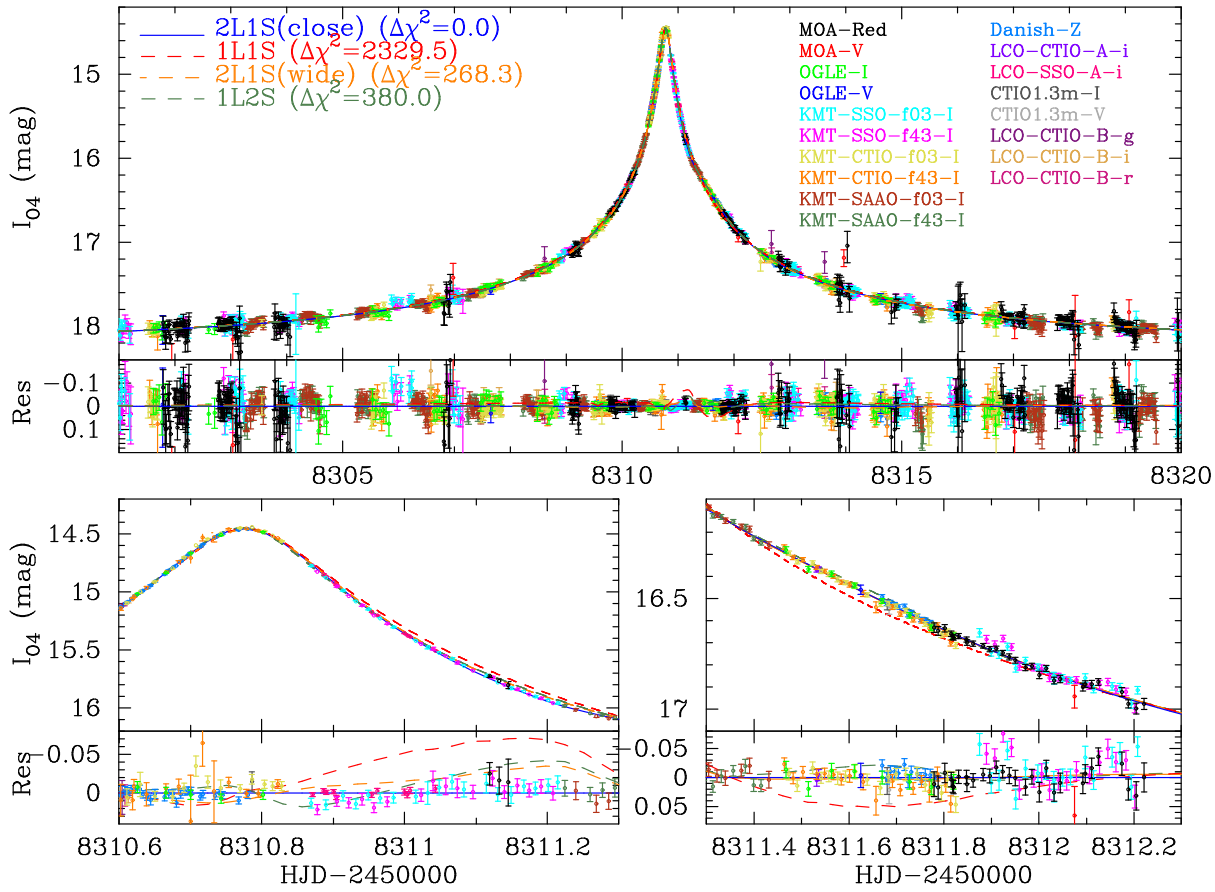

Figure 3.1: The light curve and models with the ground-based data for OGLE-2018-BLG-1185. Top panel shows the light curve, models, and residuals from the best-fit close binary-lens (2L1S) model. The blue line shows the best-fit close 2L1S model. The red, orange, and green dot lines show the single-lens (1L1S) model, the wide 2L1S model, and the binary-source (1L2S) model, respectively. The left bottom panel and the right panel show the zoomed-in views of the light curve, where we can find clear deviations of data points from the 1L1S and 1L2S models.

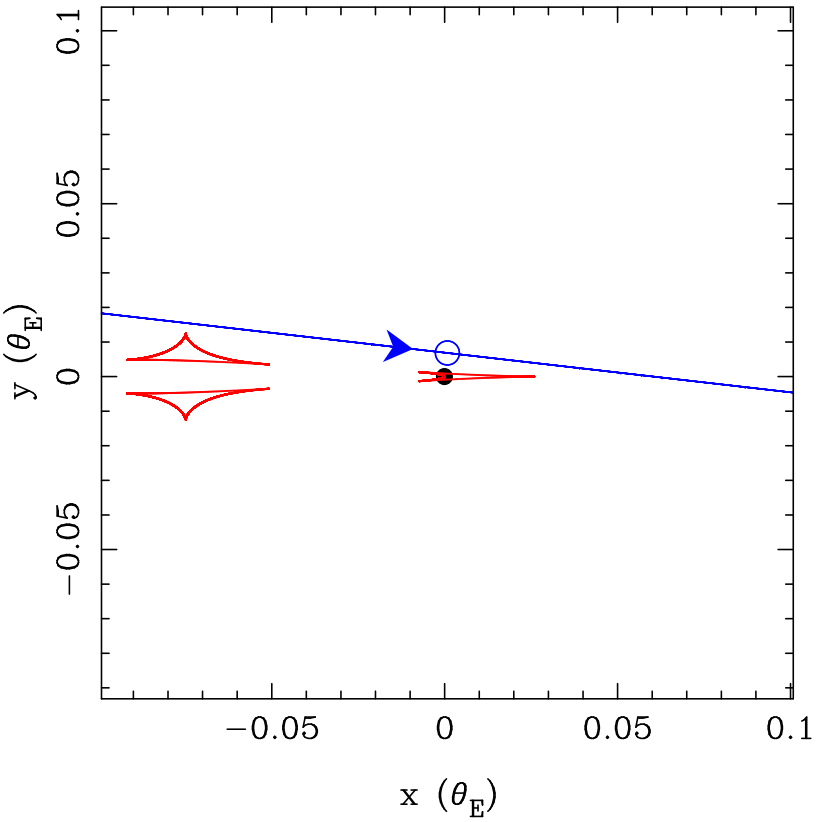

Figure 3.2: Caustic geometry of the best-fit model. The caustics are shown in red lines. The blue line shows the source trajectory on the lens plane and the arrow indicates the direction of the source/lens relative proper motion. The blue open circle indicates the source size and position at t_0.

system has a very-low-mass ratio, $q \sim 6.9 \times 10^{-5}$, with a normalized separation $s \sim 0.96$. It is well known that there is a close/wide degeneracy in high-mag binary-lens events (Griest & Safizadeh, 1998; Dominik, 1999; Chung et al., 2005), which is due to the similar shape and size of the central caustic between s and s^{-1}. From the grid search, we found the best wide binary-lens model ($s > 1$) has $q \sim 9.2 \times 10^{-5}$ and $s \sim 1.14$. The separation of this wide model is slightly different from the reciprocal of the separation of the close model ($s < 1$), yielding a different shape and size for the central caustic from those of the best close model. We ruled out the wide model because the best close binary-lens model is favored over the wide model by $\Delta\chi^2 \sim 268$. The $\Delta\chi^2$ is large because the source trajectory is parallel to the lens axis and approaches not only the central caustic but also the planetary caustics.

3.3.2 Binary-source model

We checked the possibility that the observed light-curve can be explained by the binary-source model because it is known that there is a possible degeneracy between single-lens binary-source (1L2S) model and binary-lens single-source (2L1S)

model (Griest & Hu, 1993; Gaudi, 1998). For the 1L2S model, the total effective magnification of the source stars A is expressed as follows:

$$A = \frac{A_1 f_1 + A_2 f_2}{f_1 + f_2} = \frac{A_1 + q_f A_2}{1 + q_f}, \tag{3.5}$$

where A_1 and A_2 are the magnification of the two sources with model flux f_1 and f_2, respectively, and q_f is the flux ratio between the two sources ($= f_2/f_1$). In order to explain the magnification of the second source, we introduce additional parameters: the time of lens-source closest approach $t_{0,2}$, the impact parameter in units of the Einstein radius $u_{0,2}$, and the ratio of the angular source size to the angular Einstein radius, ρ_2. We found the best-fit 1L2S model is disfavored relative to the best-fit 2L1S model by $\Delta\chi^2 \sim 380$, and we excluded the 1L2S model. The parameters of the best-fit 1S2L model are summarized in Table 3.2. The light curve of the 1L2S model is shown in Figure 3.1.

3.3.3 Ground-Based Parallax

The magnification of the binary-lens model with parallax effects needs two additional parameters: the north and east components of parallax vector $\boldsymbol{\pi}_{\rm E}$ in equatorial coordinates, $\pi_{\rm E,E}$ and $\pi_{\rm E,N}$ (Gould, 2004). The orbital parallax effects are caused by Earth's orbital motion. In the case of OGLE-2018-BLG-1185, the timescale, $t_{\rm E} \sim 15.9$ days, is small compared to Earth's orbital period, which makes it less likely for us to measure the parallax effects. The best-fit parallax model improves the fit slightly by $\Delta\chi^2 \sim 20$, but there is disagreement in χ^2 improvement between the data sets. The parallax information such as the direction and the value is easily influenced by the systematics in each telescope data set. Considering these facts, we concluded that we should disregard the parallax information from the ground-based data.

Table 3.2: The best-fit models for ground-only data

Parameters	Unit	2L1S(close)	2L1S(wide)	1L2S
χ^2/dof		23221.473/23252	23489.306/23252	23601.431/23249
$t_{0,1}$	HJD′	8310.7772 ± 0.0003	8310.7793 ± 0.0003	8310.7726 ± 0.0003
$t_{0,2}$	HJD′	...	...	8311.5874 ± 0.0010
$t_{\rm E}$	days	15.931 ± 0.133	16.312 ± 0.144	15.730 ± 0.189
$u_{0,1}$	10^{-3}	6.877 ± 0.063	6.606 ± 0.067	7.777 ± 0.131
$u_{0,2}$	10^{-3}	...	...	8.773 ± 1.515
q	10^{-5}	6.869 ± 0.229	9.164 ± 0.552	...
s		0.963 ± 0.001	1.144 ± 0.003	...
α	radian	0.114 ± 0.001	3.261 ± 0.002	...
ρ_1	10^{-3}	3.468 ± 0.083	<1.026[a]	7.234 ± 0.241
ρ_2	10^{-3}	...	...	1.613 ± 0.956
$q_{f,I}$	10^{-2}	...	...	1.699 ± 0.192
f_S (OGLE) [b]		107.777 ± 0.437	106.493 ± 0.448	108.583 ± 0.550
f_b (OGLE) [b]		396.165 ± 0.594	397.397 ± 0.440	393.516 ± 0.587

[a] The value is the 3σ upper limit.

[b] All fluxes are on a 25th magnitude scale, e.g., $I_{\rm S} = 25 - 2.5\log(f_{\rm S})$.

3.4 Angular Einstein Radius

We can estimate the angular Einstein radius $\theta_{\rm E} = \theta_*/\rho$ because ρ can be derived by the light-curve fitting and the angular source radius θ_* can be derived by using an empirical relation between θ_*, the extinction-corrected source color $(V-I)_{\rm S,0}$, and the magnitude $I_{\rm S,0}$ (e.g., Boyajian et al., 2014).

We derived the OGLE-IV instrumental source color and magnitude from the light-curve fitting and then converted them to the standard ones by using the following color-color relation from Udalski et al. (2015a):

$$I_{\rm O3} - I_{\rm O4} = (0.182 \pm 0.015) + (-0.008 \pm 0.003)(V-I)_{\rm O3}, \quad (3.6)$$

$$V_{\rm O3} - V_{\rm O4} = (0.257 \pm 0.015) + (-0.074 \pm 0.004)(V-I)_{\rm O3}. \quad (3.7)$$

The apparent color and the standard magnitude of the source star are $(V-I, I)_{\rm S,O4,calib} = (2.344 \pm 0.031, 20.082 \pm 0.012)$.

We also derived the apparent source color and magnitude from the CT13 measurements in the I- and V-bands from the light-curve fitting, and then converted them to the standard ones following the procedure explained in Bond et al. (2017). We cross-referenced isolated stars in the CT13 catalog reduced by DoPHOT (Schechter et al., 1993) with the stars in the OGLE-III map within $120''$ of the source star and obtained the color-color relations

$$I_{\rm O3} - I_{\rm CT13} = (-0.880 \pm 0.005) + (-0.042 \pm 0.005)(V-I)_{\rm CT13}, \quad (3.8)$$

$$V_{\rm O3} - I_{\rm CT13} = (1.290 \pm 0.004) + (-0.036 \pm 0.004)(V-I)_{\rm CT13}. \quad (3.9)$$

The apparent color and magnitude of the source star are $(V-I, I)_{\rm S,CT13,calib} = (2.335 \pm 0.025, 20.105 \pm 0.013)$. This color is consistent with $(V-I)_{\rm S,O4,calib}$ within 1σ and the magnitude is consistent with $I_{\rm S,O4,calib}$ within 2σ. Because the light curve was well covered by the OGLE observations, while it was highly magnified, we adopted $(V-I, I)_{\rm S,O4,calib}$ as the source color and magnitude.

To obtain the extinction-corrected source color and magnitude, we used the standard method from Yoo et al. (2004). The intrinsic color and magnitude are determined from the source location relative to the color and magnitude of the red clump giant (RCG) centroid in the color-magnitude diagram (CMD). In Figure 3.3, the red point shows the RCG centroid color and magnitude, $(V-I, I)_{\rm RCG} = (2.720, 16.325) \pm (0.009, 0.032)$ for the field around the source star. Assuming that the source star suffers the same reddening and extinction as the RCGs, we compared these values to the expected extinction-corrected RCG color and magnitude for this field, $(V-I, I)_{\rm RCG,0} = (1.060, 14.362) \pm (0.070, 0.040)$ (Bensby et al., 2013; Nataf et al., 2013). As a result, we obtained an extinction of $A_I = 1.963 \pm 0.051$ and a color excess of $E(V-I) = 1.660 \pm 0.071$. Finally, the intrinsic source color and magnitude were derived:

$$(V-I, I)_{\rm S,0} = (0.684, 18.119) \pm (0.077, 0.053). \quad (3.10)$$

As a reference for later discussion of future follow-up observations, we also estimated the intrinsic source magnitudes in the H- and K-bands from the color-color

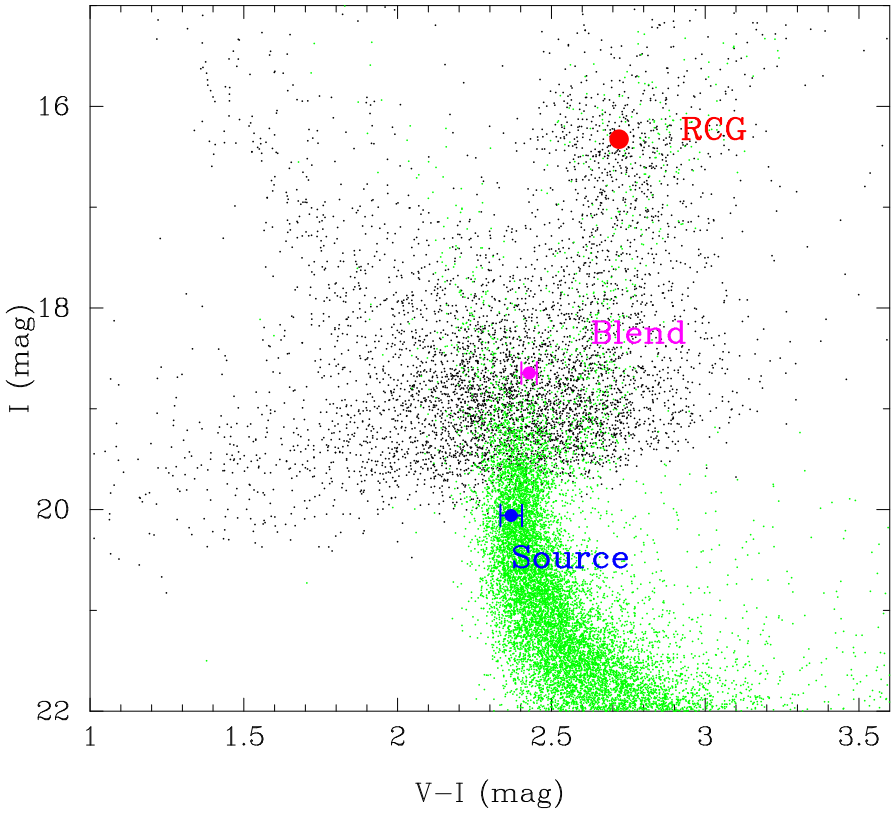

Figure 3.3: The CMD. The stars in the OGLE-III catalog within 120″ of the source star are shown with black dots. The green dots indicate the *HST* CMD of (Holtzman et al., 1998), which is transformed to the same reddening and extinction of the field of the event. The red dot shows the centroid of the RCG distribution. The colors and magnitudes of the source star and the blend are shown with blue and pink, respectively.

relation in Kenyon & Hartmann (1995), including a 5% uncertainty. Then, we applied the extinction in the H- and K-bands, which was derived from the extinction in the I- and V-bands of the RCGs according to Cardelli et al. (1989).

Figure 3.3 shows that the source is consistent with being part of the standard bulge sequence of stars, i.e., it falls within the distribution of stars from (Holtzman et al., 1998) after they have been shifted to the same reddening and extinction as the field for OGLE-2018-BLG-1185. However, the source also has a similar color to the Sun. Thus, it would also be consistent with having an absolute magnitude similar to that of the Sun but being somewhat in the foreground, e.g., at ~ 6 kpc. Therefore, we also checked how a different assumption about the source would affect our results. If the source was more in the foreground, it would then suffer less extinction and reddening than the RCGs. However, even if we assume 10% less extinction and reddening than those of the RCGs, the value of $\theta_{\rm E}$ increases by only 7%, which is still consistent within 1σ with values obtained assuming the same extinction and reddening as those of the RCGs. We summarize the source colors and magnitudes in Table 3.3.

Table 3.3: The source color and magnitudes

Parameters	Unit	Source (apparent)	Source (intrinsic)[a]	Source (intrinsic)[b]
I	mag	20.082 ± 0.012 [c]	18.119±0.053	18.315±0.053
$V-I$	mag	2.344 ± 0.031 [c]	0.684±0.077	0.850±0.077
H [d]	mag	18.012±0.143	17.444±0.095	...
K [d]	mag	17.756±0.145	17.394±0.095	...

[a] Extinction-corrected magnitudes assuming that the source star suffers the same reddening and extinction as the RCGs.
[b] Extinction-corrected magnitudes assuming that the source star suffers the reddening and extinction of 0.9 times as much as those for the RCGs.
[c] The magnitude and color are measured from the light-curve fitting.
[d] The magnitudes are estimated from the color-color relation in Kenyon & Hartmann (1995) and the extinction law in Cardelli et al. (1989).

Applying the empirical formula, $\log(\theta_{\rm LD}) = 0.501414 + 0.419685(V-I) - 0.2I$ (see Fukui et al., 2015 but also Boyajian et al., 2014), where $\theta_{\rm LD} \equiv 2\theta_*$ is the limb-darkened stellar angular diameter, we found the angular source radius,

$$\theta_{\rm LD} = 1.461 \pm 0.109\ \mu{\rm as}, \tag{3.11}$$

$$\theta_* = 0.730 \pm 0.059\ \mu{\rm as}. \tag{3.12}$$

Finally, we obtained the source angular radius and the lens–source relative proper motion in the geocentric frame:

$$\theta_{\rm E} = \frac{\theta_*}{\rho} = 0.211 \pm 0.018\ {\rm mas}, \tag{3.13}$$

$$\mu_{\rm rel,geo} = \frac{\theta_{\rm E}}{t_{\rm E}} = 4.832 \pm 0.410\ {\rm mas\ yr^{-1}} \tag{3.14}$$

This $\theta_{\rm E}$ value is relatively small, which suggests that the lens is a low-mass star and/or distant from the observer.

3.5 Lens Physical Parameters by Bayesian Analysis

If we can measure both the finite source effects and the parallax effects, the lens physical parameters such as the host mass $M_{\rm host}$ and the distance to the lens $D_{\rm L}$ are calculated directly, following the equations

$$M_{\rm host} = \frac{\theta_{\rm E}}{(1+q)\kappa\pi_{\rm E}}; \quad D_{\rm L} = \frac{\rm au}{\pi_{\rm rel}+\pi_{\rm S}}; \quad \pi_{\rm rel} = \theta_{\rm E}\pi_{\rm E}; \quad \boldsymbol{\mu}_{\rm rel} = \frac{\theta_{\rm E}}{t_{\rm E}}\frac{\boldsymbol{\pi}_{\rm E}}{\pi_{\rm E}}, \tag{3.15}$$

where $\kappa \equiv 4G/(c^2{\rm au}) = 8.1439$ mas$/M_\odot$, and $\pi_{\rm S} = {\rm au}/D_{\rm S}$ is the source parallax. From the ground-based light-curve alone, we are only able to measure $\theta_{\rm E}$ (via finite source effects), but no meaningful constraint on $\pi_{\rm E}$ (see Section 3.3).

In order to estimate the probability distributions of $M_{\rm L}$ and $D_{\rm L}$, we conducted a Bayesian analysis with the Galactic model of Koshimoto et al. (2021a). We randomly generated a 50 million simulated microlensing event sample. Then we calculated the probability distributions for the lens physical parameters by weighting the microlensing event rate by the measured $t_{\rm E}$ and $\theta_{\rm E}$ likelihood distribution. It is important to note that we conducted the Bayesian analysis under the assumption that stars of all masses have an equal probability of hosting the planet.

We calculated some parameters in addition to the lens physical parameters, $M_{\rm L}$ and $D_{\rm L}$. For instance, the lens-source proper motion in the geocentric frame, $\boldsymbol{\mu}_{\rm rel}$, is converted to that in the heliocentric frame,

$$\boldsymbol{\mu}_{\rm rel,hel} = \boldsymbol{\mu}_{\rm rel} + \boldsymbol{v}_{\oplus,\perp}\frac{\pi_{\rm rel}}{\rm au}, \tag{3.16}$$

where $\boldsymbol{v}_{\oplus,\perp} = (v_{\oplus,N}, v_{\oplus,E}) = (-0.78, 27.66)$ km/s is the projected velocity of Earth at t_0.

We also calculated the I- and V-band magnitudes of the lens from the mass-luminosity relations of main-sequence stars (Kenyon & Hartmann, 1995), and the 5 Gyr isochrone for brown dwarfs from Baraffe et al. (2003). Then we estimated the H- and K-band magnitudes of the lens from the color-color relation in Kenyon & Hartmann (1995), including a 5% uncertainty. In order to estimate the extinction in the foreground of the lens, we assumed a dust scale height of $h_{\rm dust} = 0.10 \pm 0.02$ kpc (Bennett et al., 2015),

$$A_{\lambda,{\rm L}} = \frac{1 - e^{-|D_{\rm L}/(h_{\rm dust}\sin b)|}}{1 - e^{-|D_{\rm S}/(h_{\rm dust}\sin b)|}} A_{\lambda,{\rm S}}, \tag{3.17}$$

where the index λ refers to the passband: V-, I-, H-, or K-band. We obtained the extinction in the I- and V-band magnitudes of the source from the RCGs in Section 3.4, and then we converted it to the extinction in the H- and K-bands according to Cardelli et al. (1989).

The results are shown in Table 3.4 and Figure 3.4. According to Figure 3.4, the lens system is likely to be a super-Earth with a mass of $m_{\rm p} = 8.1^{+7.6}_{-4.4}\ M_\oplus$ orbiting a late M-dwarf with a mass of $M_{\rm host} = 0.36^{+0.33}_{-0.19} M_\odot$ at a projected separation of $a_\perp = 1.54^{+0.18}_{-0.22}$ au. The system is located at $D_{\rm L} = 7.4^{+0.5}_{-0.9}$ kpc from Earth. For

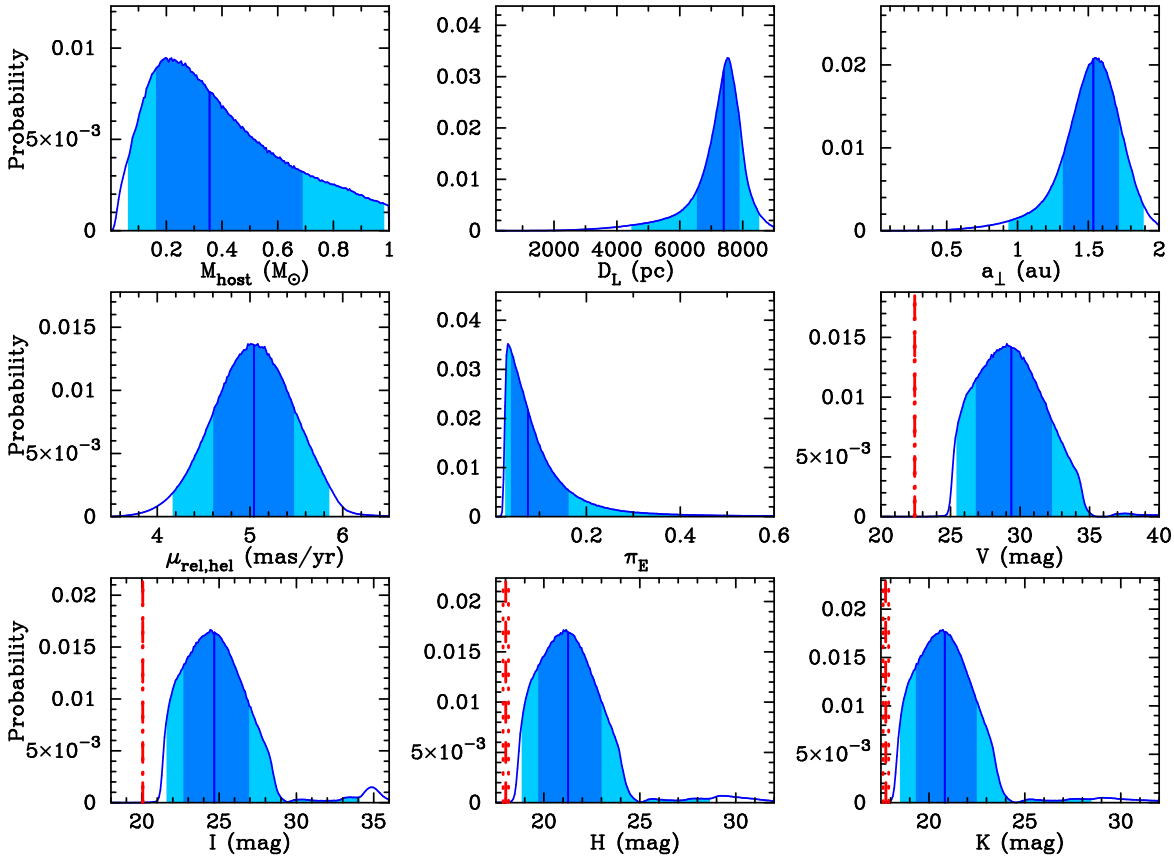

Figure 3.4: Probability distribution of lens properties derived from the Bayesian analysis with a Galactic prior and constrained by $t_{\rm E}$ and $\theta_{\rm E}$. The vertical blue lines show the median values. The dark-blue and the light-blue regions show the 68.3% and 95.4% confidence intervals. The vertical red lines in the probability distributions of I-, V-, H-, and K-band magnitudes show the magnitudes of the source star with extinction.

reference, we also plot the source magnitudes in the V-, I-, H-, and K-band as red lines; the H- and K-band magnitudes were estimated in Section 3.4. We also show the parallax contour derived from the Bayesian analysis in Figure 3.5.

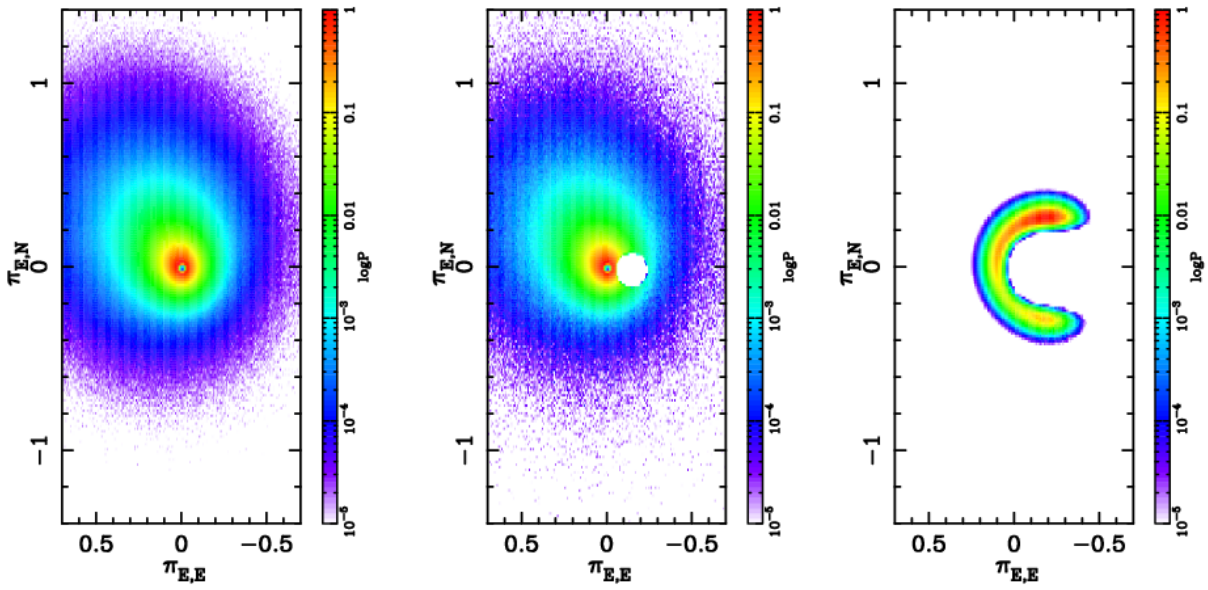

Figure 3.5: **Left**: The parallax contours for OGLE-2018-BLG-1185 expected from the Galactic model of Koshimoto et al. (2021a) after imposing the two observational constraints of the angular Einstein radius, $\theta_{\rm E}$ and the Einstein radius crossing time, $t_{\rm E}$, on the event rate. The colorbar corresponds to the logarithm of the event rate and the red region indicates higher probability. **Center**: Including the constraint that $\Delta f_{\rm Spz} < 4$. **Right**: Including the full constraint from the *Spitzer*-"only" parallax.

Table 3.4: The lens physical parameters

		Bayesian			Naive *Spitzer*-"only"	
Parameters	Unit	Ground-only	Ground + $\Delta f_{\rm Spz}$	Ground + $\boldsymbol{\pi}_{\rm E,Spz}$	($u_0 > 0$)	($u_0 < 0$)
$M_{\rm host}$	$M_\odot$	$0.36^{+0.33}_{-0.19}$	$0.37^{+0.35}_{-0.21}$	$0.091^{+0.064}_{-0.018}$	0.073 ± 0.011	0.070 ± 0.010
$m_{\rm p}$	$M_\oplus$	$8.1^{+7.6}_{-4.4}$	$8.4^{+7.9}_{-4.7}$	$2.1^{+1.5}_{-0.4}$	1.7 ± 0.3	1.6 ± 0.2
D_L	kpc	$7.40^{+0.51}_{-0.85}$	$7.40^{+0.51}_{-0.88}$	$5.45^{+1.70}_{-0.66}$	4.96 ± 0.74	4.89 ± 0.66
$a_\perp$	au	$1.54^{+0.18}_{-0.22}$	$1.54^{+0.18}_{-0.22}$	$1.14^{+0.32}_{-0.15}$	1.01 ± 0.18	0.99 ± 0.16
$\pi_{\rm E}$		$0.075^{+0.087}_{-0.036}$	$0.073^{+0.093}_{-0.035}$	$0.292^{+0.066}_{-0.120}$	0.354 ± 0.042	0.369 ± 0.037
$\mu_{\rm rel,hel}$	mas/yr	$5.04^{+0.43}_{-0.44}$	$5.06^{+0.43}_{-0.44}$	4.86 ± 0.44	...	...
V	mag	$29.4^{+2.9}_{-2.6}$	$29.3^{+3.1}_{-2.6}$	$34.1^{+5.2}_{-1.6}$	...	...
I	mag	$24.7^{+2.3}_{-2.0}$	$24.6^{+2.4}_{-2.0}$	$28.2^{+3.4}_{-1.2}$	...	...
H	mag	$21.3^{+1.7}_{-1.6}$	$21.2^{+1.9}_{-1.6}$	$23.9^{+2.6}_{-0.9}$	...	...
K	mag	$20.8^{+1.7}_{-1.5}$	$20.8^{+1.8}_{-1.5}$	$23.3^{+2.9}_{-0.8}$	...	...

3.6 Analysis including *Spitzer* data

We measure the microlens parallax vector $\boldsymbol{\pi}_{\rm E}$ via the satellite parallax effect, which can be approximated as

$$\boldsymbol{\pi}_{\rm E} = \frac{\rm au}{D_\perp} \left(\frac{t_{0,\rm sat} - t_{0,\oplus}}{t_{\rm E}}, u_{0,\rm sat} - u_{0,\oplus} \right), \tag{3.18}$$

where $D_\perp$ is the Earth-satellite separation projected on the plane of the sky, and $t_{0,\rm sat}$ and $u_{0,\rm sat}$ are the time of lens-source closest approach and the impact parameter as seen by the satellite. The Einstein timescale $t_{\rm E}$ is assumed to be the same for both Earth and the satellite. In practice, we fully model *Spitzer*'s location as a function of time.

The *Spitzer* light curve for OGLE-2018-BLG-1185 shows a very weak decline of $\Delta f_{\rm Spz} \sim 1$ flux unit over the four-week observation period (see Figure 3.6). This change (rather than, e.g., the value of the flux at the start of observations) is the most robust constraint because it is independent of the unknown blended light. However, the magnitude of the decline is comparable to the level of systematics seen in a few other events (Gould et al., 2020; Hirao et al., 2020; Zang et al., 2022b) and, thus, should be treated with caution. At the same time, even this weak decline indicates a significant parallax effect for the event as seen from *Spitzer*. We derive a color constraint for the *Spitzer* data by measuring the IHL color-color relation for clump stars in CT13 I and H, and *Spitzer* L. Evaluating this relation at the measured $(I-H)$ color of the source gives a constraint on the *Spitzer* source flux:

$$I_{\rm CT13} - L = -4.518 \pm 0.028, \tag{3.19}$$

which gives an expected source flux from *Spitzer* of $f_{\rm S,Spz} = 0.6254$ flux units for the best-fit value of $I_{\rm CT13}$. This constraint and the best-fit ground-based model (Table 3.4) together imply some tension with the observed *Spitzer* light curve unless there is a significant parallax effect. They predict that the observed *Spitzer* flux should have been substantially brighter at the start of the *Spitzer* observations ($f_{\rm Spz}({\rm HJD}' = 8313.83) \sim 6$ flux units) and declined by a total of $\Delta f_{\rm Spz} \sim 3.3$ flux units as compared to the observed $\Delta f_{\rm Spz} \sim 1$ flux unit. This tension can be seen in Figure 3.6 and suggests that, due to the parallax effect, the event peaked at a lower magnification and/or earlier as seen from *Spitzer*.

We can use limits on the change in *Spitzer* flux ($\Delta f_{\rm Spz}$) to place conservative constraints on the physical properties of the lens. Suppose that systematics affect the *Spitzer* light curve at the level of 1–2 flux units, i.e., at the level seen in previous work. If the true signal is $\Delta f_{\rm Spz} \sim 4$ flux units, it is very unlikely that systematics would cause us to measure $\Delta f_{\rm Spz} = 1$ flux unit. Therefore, we repeat the Bayesian analysis imposing the constraint $\Delta f_{\rm Spz} < 4$, where $\Delta f_{\rm Spz}$ is calculated from Equation (3.19). The parallax effect can produce a degeneracy in the sign of u_0. In this case, because u_0 is small, the effect of this degeneracy is much smaller than the uncertainties (Gould & Yee, 2012), so we only carry out this calculation for the $u_0 > 0$ case.

The results are given in Table 3.4 (as "Ground + $\Delta f_{\rm Spz}$"), Figure 3.6, and the center panel of Figure 3.5. This constraint suggests an $M_{\rm host} = 0.37^{+0.35}_{-0.21}\ M_\odot$ host

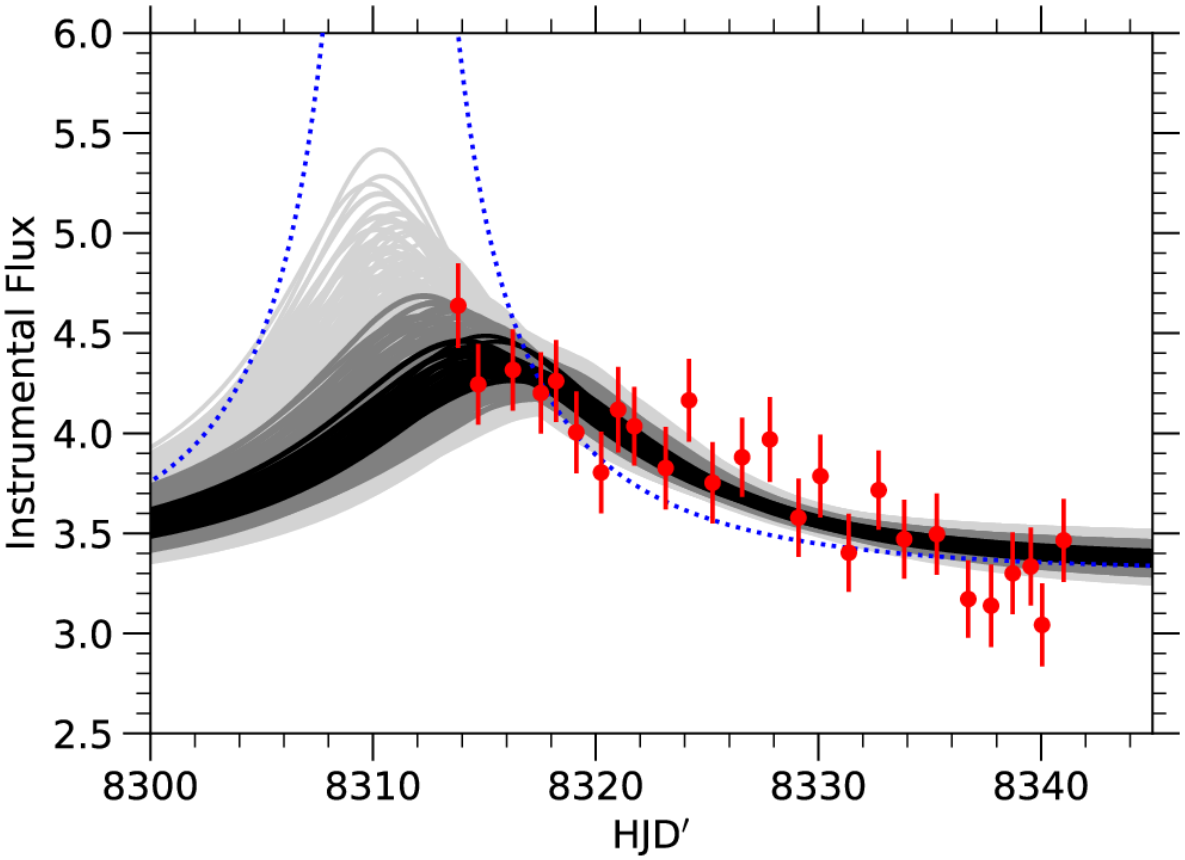

Figure 3.6: The light curve and models with the *Spitzer* data. The blue dotted line shows the *Spitzer* flux predicted by the 2L1S best-fit model derived from the ground-based analysis for $\boldsymbol{\pi}_{\rm E} = (0, 0)$ evaluated at the central value of the color-constraint. The black and gray shaded regions show the models derived from the *Spitzer*-"only" parallax analysis. Each color (black, dark gray, and light gray) represents $\Delta\chi^2 < (1,4,9)$.

with an $m_p = 8.4^{+7.9}_{-4.7}\ M_\oplus$ planet at a projected separation $a_\perp = 1.54^{+0.18}_{-0.22}$ au. We adopt these values as our conservative Bayesian estimates of the properties of the lens system.

3.6.1 *Spitzer*-"only" Parallax

If we take the *Spitzer* light curve at face value, we can derive stronger constraints on the parallax using the *Spitzer*-"only" parallax method. This method has been used in several previous analyses (starting with Gould et al., 2020) to show how the *Spitzer* light curve constrains the parallax. For this analysis, we hold the microlensing parameters t_0, u_0, and $t_{\rm E}$ fixed at values found by fitting the ground-based data and make the assumption that the *Spitzer* light curve is in the point

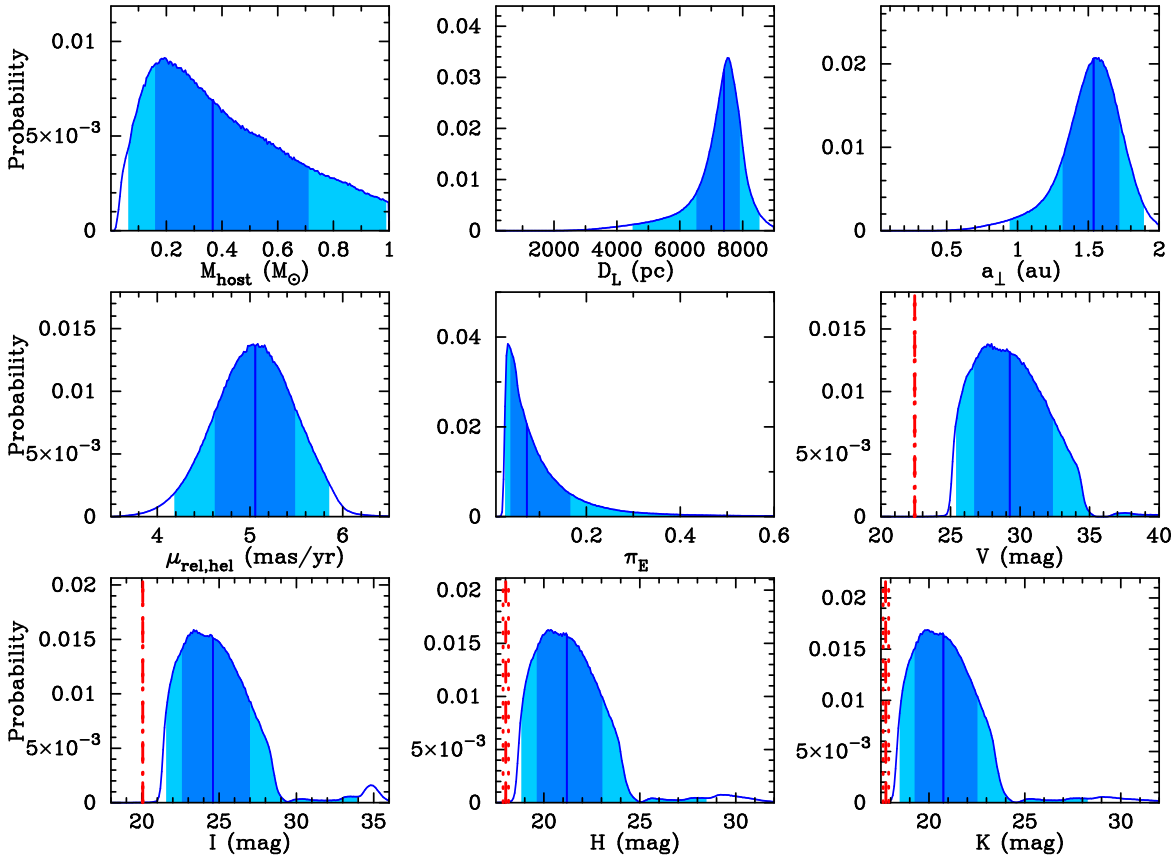

Figure 3.7: Same as Figure 3.4, but with the addition of the constraint $\Delta f_{\rm Spz} < 4$.
Same as Figure 3.4, but with the addition of the constraint $\Delta f_{\rm Spz} < 4$.

lens regime.[3] Then, for a grid of parallax values, we fit for the *Spitzer* flux while applying the color constraint from Equation (3.19). We repeat the analysis for $-u_0$, which produces an indistinguishable ground-based light curve and, as expected, only slight variations in the parallax.

The resulting parallax contours are shown in Figure 3.8. The four minima correspond to the well-known satellite parallax degeneracy (Refsdal, 1966; Gould, 1994) and the overall arc shape follows the expectation from the Gould (2019) osculating circles formalism. The values for the magnitude of the microlens parallax vector are $\pi_{\rm E} = 0.35 \pm 0.04$ for the $(u_0 > 0)$ case and $\pi_{\rm E} = 0.37 \pm 0.04$ for the $(u_0 < 0)$ case. The 3σ ranges are $\pi_{\rm E} = [0.18, 0.50]$ and $\pi_{\rm E} = [0.20, 0.48]$, respectively.

[3] In principle, we should calculate the *Spitzer* magnification using the full planetary model, but in practice, this makes almost no difference because the *Spitzer* observations start well after the planetary perturbation.

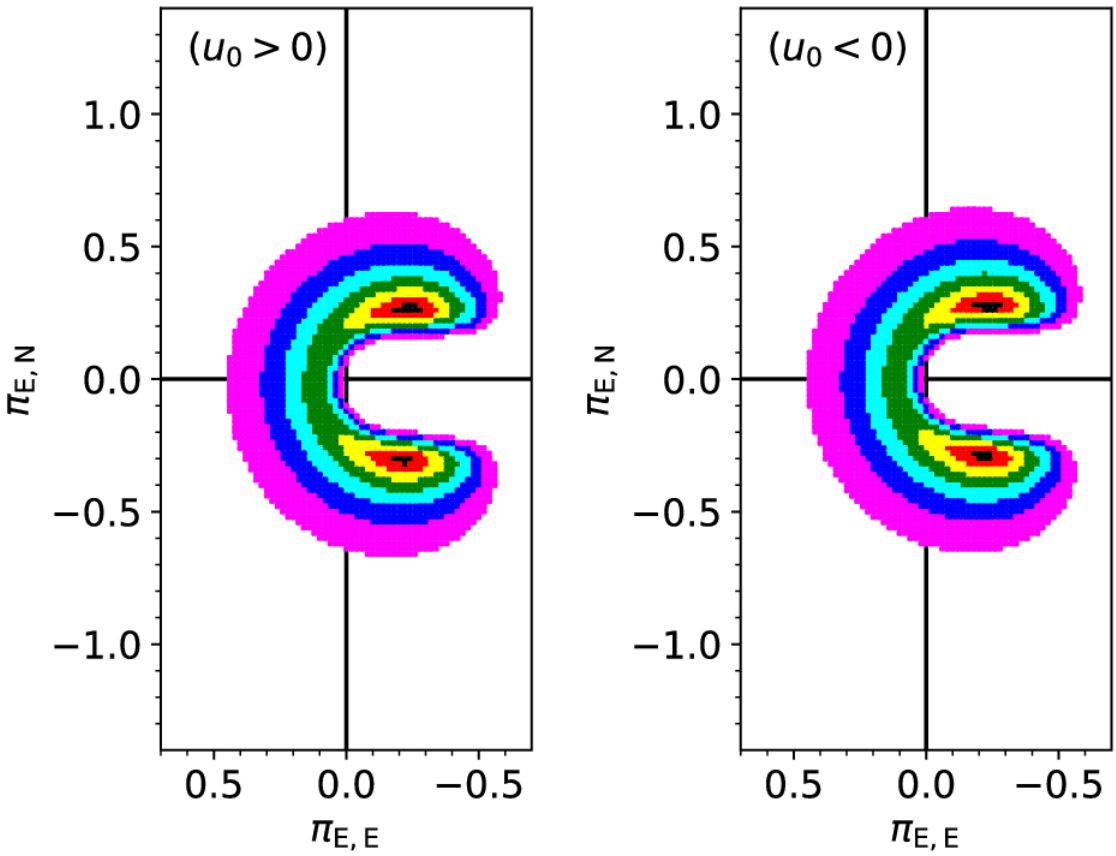

Figure 3.8: Parallax contours from *Spitzer*-"only" analysis (see text). The colors –black, red, yellow, green, cyan, blue, and magenta– indicate $1\sigma, 2\sigma, 3\sigma, 4\sigma, 5\sigma, 6\sigma$, and 7σ from the minimum, respectively. The left panel is for $(u_0 > 0)$ and the right panel is for $(u_0 < 0)$.

3.6.2 Physical Lens Properties from *Spitzer* Parallax

We can derive the physical properties of the lens by combining the measurement of the parallax from the *Spitzer*-"only" analysis with the measurement of $\theta_{\rm E} = 0.211 \pm 0.019$ mas from fitting the ground-based light curve. These estimates and their uncertainties are derived from Equation (3.15) using simple error propagation, and so are the "naive" values of these quantities. For the $(u_0 > 0)$ solution, this yields a lens mass of $M_{\rm L} = 0.073 \pm 0.011 M_\odot$ and $D_{\rm L} = 4.96 \pm 0.74$ kpc for $D_{\rm S} = 7.88$ kpc. This would then imply that the mass of the planet is $m_{\rm p} = 1.7 \pm 0.3\ M_\oplus$ and that it is separated from the host by $a_\perp = 1.01 \pm 0.18$ au. The values for the $(u_0 < 0)$ solution are comparable. See Table 3.4.

In order to estimate the lens magnitude, we also performed a Bayesian analysis including the $\pi_{\rm E}$ constraint derived from the *Spitzer*-"only" parallax analysis. First, we took the average of the χ^2 values for the two $(u_0 > 0)$ and $(u_0 < 0)$ solutions for each value of $\pi_{\rm E,E}$ and $\pi_{\rm E,N}$. Then, the event rate was weighted by $\exp(-\Delta\chi^2/2)$ and the measured $t_{\rm E}$ and $\theta_{\rm E}$ constraints to calculate the probability

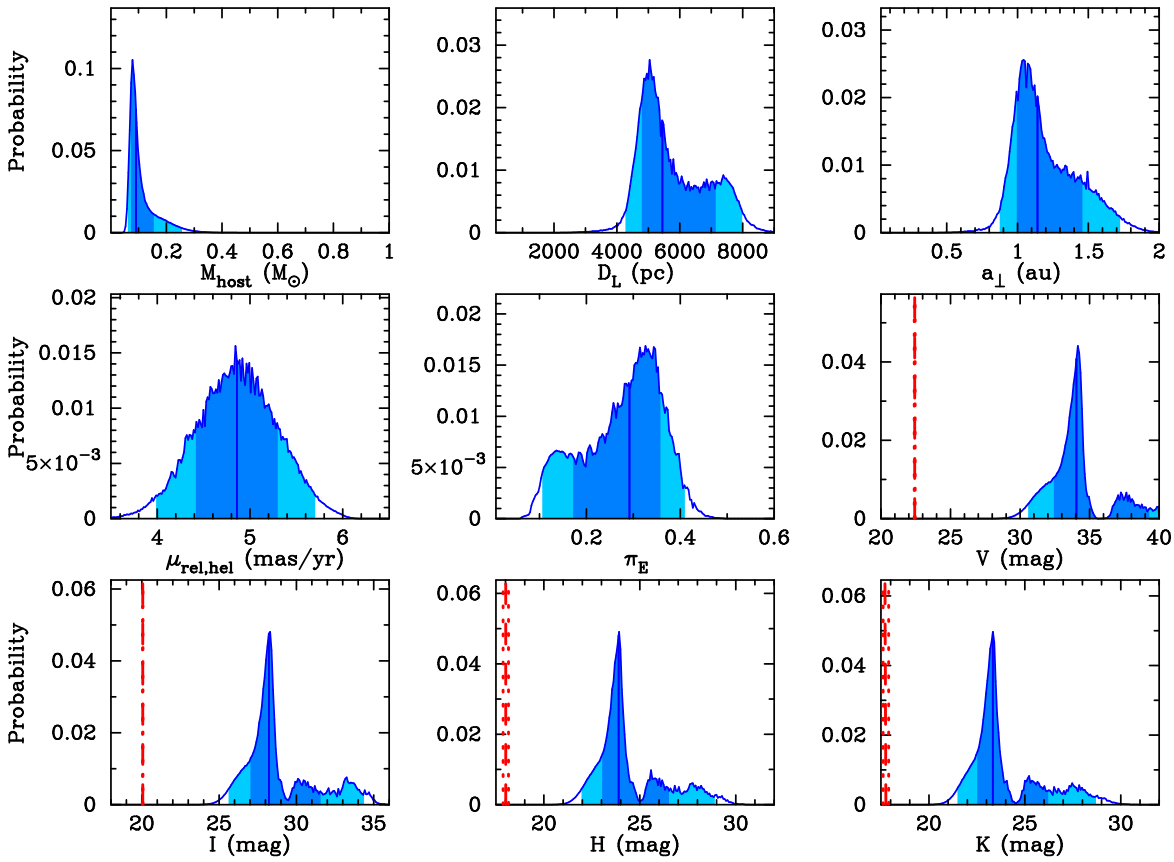

Figure 3.9: Same as Figure 3.4, but with the addition of the $\pi_{\rm E}$ constraint from the *Spitzer*-"only" parallax measurement.

distribution. Table 3.4 and Figure 3.9 show the results. The distributions for some of the parameters in Figure 3.9 are bimodal. In addition to the expected peak for lenses at $D_{\rm L} \sim 5$ kpc, there is a second peak for lenses with $D_{\rm L} \sim 7.5$ kpc. This second peak corresponds to events with lenses in the bulge and sources in the far disk, which were not considered in our naive calculations. For the bimodal distributions, the central values and confidence intervals reported in Table 3.4 are not a complete description of the distributions and should be considered in context of Figure 3.9. However, the mass distribution is not subject to this issue. We find that the lens system is likely a terrestrial planet with a mass of $m_{\rm p} = 2.1^{+1.5}_{-0.4}\ M_\oplus$ orbiting a very low mass (VLM) dwarf with a mass of $M_{\rm host} = 0.091^{+0.064}_{-0.018}\ M_\odot$.

3.6.3 Implications

Hence, if the *Spitzer*-"only" parallax is correct, this would be the second detection of a terrestrial planet orbiting a VLM dwarf from the *Spitzer* microlensing program. The first was OGLE-2016-BLG-1195Lb (Bond et al., 2017; Shvartzvald et al., 2017b), which is an $m_{\rm p} = 1.43^{+0.45}_{-0.32}\ M_\oplus$ planet orbiting an $M_{\rm L} = 0.078^{+0.016}_{-0.012}\ M_\odot$ VLM dwarf at a separation of $a_\perp = 1.16^{+0.16}_{-0.13}$ au. The distance to

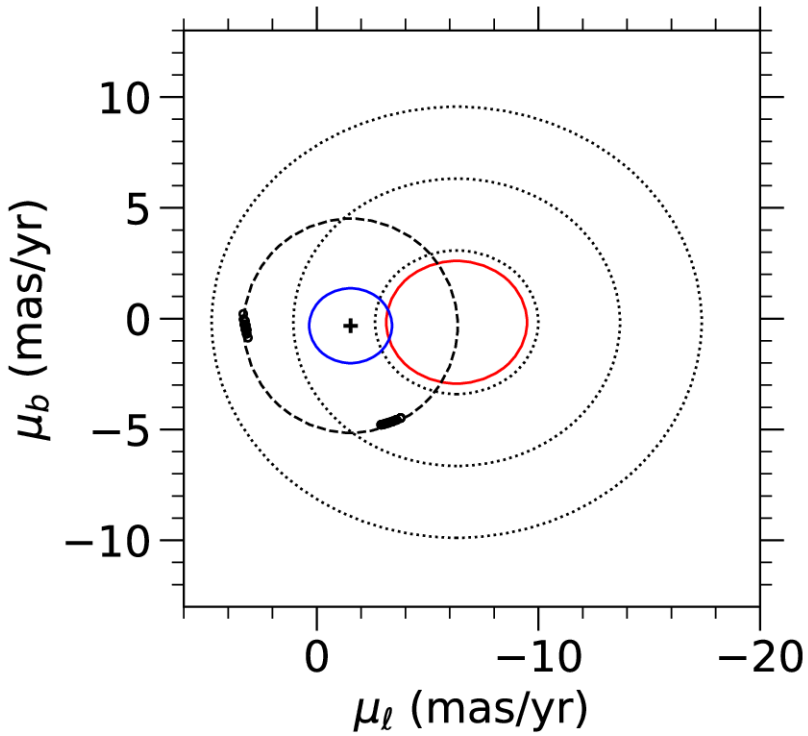

Figure 3.10: Test of source proper motion predicted by the *Spitzer*-"only" parallax. **Black points**: Derived source proper motions for $\pi_{\rm E}$ within 1σ of the minimum for the *Spitzer*-"only" contours (based on $\mu_{\rm rel,hel}$). **Black cross**: Mean proper motion for disk stars assuming a distance of $D_{\rm L} = 4.9$ kpc. **Dashed circle**: Centered on black cross with a radius $\mu_{\rm rel,geo} = 4.832$ mas yr^{-1}. Note that the black cross and dashed circle are merely reference points. **Red**: 1σ error ellipse for the bulge stars as derived from Gaia. **Blue**: 1σ error ellipse for the disk stars derived from $(\sigma_{v,\phi}, \sigma_{v,z})$. **Dotted black contours**: 1σ, 2σ, and 3σ contours adding the dispersions of the bulge and disk in quadrature. The observed constraints are consistent with a lens in the disk and a source in the bulge.

the OGLE-2016-BLG-1195L system is also comparable: $D_{\rm L} = 3.91^{+0.42}_{-0.46}$ kpc. One curiosity about OGLE-2016-BLG-1195L is that the lens-source relative proper motion suggests that the lens could be moving counter to the direction of Galactic rotation, which would be unusual for a disk lens.

Therefore, we also consider the implications of the *Spitzer*-"only" $\boldsymbol{\pi}_{\rm E}$ for constraining the lens motion in OGLE-2018-BLG-1185. First, we note that there is no independent information on the proper motion of the source $\mu_{\rm S}$ because there is no evidence that the blend, which dominates the baseline object, is associated with the event (see Appendix A.1). Second, given $D_{\rm L} \sim 4.9$ kpc, we assume that the lens is in the disk, and therefore, has a proper motion similar to that of other disk stars. The velocity model of Koshimoto et al. (2021a) is based on the Shu distribution function model in Sharma et al. (2014), but the mean velocity and velocity dispersion in the disk are fitted to the Gaia DR2 data (Gaia

Collaboration et al., 2018) as a function of the Galactocentric distance, R, and the height from the Galactic plane, z. The velocity of disk stars at 4.9 kpc is $(v_\phi, v_z) = (207.6^{+42.7}_{-44.0}, -0.4^{+38.8}_{-39.6})$ km s^{-1}. Hence, for the velocity dispersion, we use $(\sigma_{v,\phi}, \sigma_{v,z}) = (43.4, 39.2)$ km s^{-1}. Table 3.5 summarizes the disk star velocities and proper motions expected from the Galactic model at $D = 4.9 \pm 0.7$ kpc. The values in the table are derived from the Bayesian analysis with a Galactic prior and constrained by $\theta_{\rm E}$ and $t_{\rm E}$. For the Sun's motion, we use $(v_R, v_\phi, v_z)_{\rm Sun} = (-10, 243, 7)$ km s^{-1} (for $(R_\odot, z_\odot) = (8160, 25)$ pc). We combine the two velocities to estimate the proper motion of disk stars. Finally, by applying Equation 3.16, we can derive the expected source proper motion $\mu_{\rm S} = \mu_{\rm L} - \mu_{\rm rel,hel}$ for a given value of the parallax. Figure 3.10 shows the results for values of $\boldsymbol{\pi}_{\rm E}$ out to the 1σ *Spitzer*-"only" contours for the $(u > 0)$ solution (the results for the $(u < 0)$ solution are nearly identical). The properties of bulge stars are derived from Gaia stars within $5'$ of the target: $\mu_{\rm bulge}(\ell, b) = (-6.310, -0.163) \pm (0.088, 0.076)$ mas yr^{-1} and $\sigma_{\rm bulge}(\ell, b) = (3.176, 2.768) \pm (0.062, 0.054)$ mas yr^{-1}. To account for the uncertainty in the lens motion, we add the proper motion dispersions of the disk and bulge in quadrature. One of the two *Spitzer* minima suggests a source more than 2σ from the bulge distribution, but the other minimum is consistent with a bulge source at $\sim 1.5\sigma$. Therefore, there is no reason to believe that the *Spitzer* $\boldsymbol{\pi}_{\rm E}$ requires a lens proper motion in tension with the motion of typical disk stars.

Finally, in order to include the event in the statistical sample for the study of the Galactic distribution of planets, Zhu et al. (2017) proposed the criteria

$$\sigma(D_{8.3}) < 1.4\text{kpc}; \quad D_{8.3} \equiv \frac{\text{kpc}}{\pi_{\rm rel}/\text{mas} + 1/8.3}. \tag{3.20}$$

We find $D_{8.3} = 5.15 \pm 0.28$ kpc for the $(u_0 > 0)$ case and $D_{8.3} = 5.04 \pm 0.28$ kpc for the $(u_0 < 0)$ case by combining the measurement of $\boldsymbol{\pi}_{\rm E}$ from the *Spitzer*-"only" analysis with the measurement of $\theta_{\rm E}$ from fitting the ground-based light curve. The small $\sigma(D_{8.3})$ is consistent with the expectation for a high magnification event as investigated by Gould & Yee (2012), Shin et al. (2018), and Gould (2019). They show that accurate parallax measurements are possible even if there are only a few observations taken by *Spitzer* when the Earth-based magnification is high ($A_\oplus \geq 100$). Therefore, in terms of $\sigma_{\rm D8.3}$ (Zhu et al., 2017), the *Spitzer*-"only" parallax suggests that the apparent signal is good enough to include OGLE-2018-BLG-1185Lb in the statistical sample of *Spitzer* events. However, the systematics need to be studied and understood before membership in the sample can be definitively evaluated.

Table 3.5: Disk star velocities and proper motions at $D = 4.9 \pm 0.7$ kpc

Star Component	Velocity Component	Unit	-2σ	-1σ	Median	$+1\sigma$	$+2\sigma$
Thin Disk	v_l	km s^{-1}	110.7	163.6	205.9	242.4	280.7
	v_b	km s^{-1}	-95.0	-48.8	-13.7	22.4	71.1
	$\mu_{\mathrm{hel},l}$	mas yr^{-1}	-5.615	-3.349	-1.577	-0.024	1.656
	$\mu_{\mathrm{hel},b}$	mas yr^{-1}	-4.364	-2.388	-0.884	0.653	2.690
Thick Disk	v_l	km s^{-1}	60.7	125.2	181.4	236.5	293.7
	v_b	km s^{-1}	-147.8	-86.4	-12.1	63.3	128.6
	$\mu_{\mathrm{hel},l}$	mas yr^{-1}	-7.662	-4.995	-2.602	-0.275	2.177
	$\mu_{\mathrm{hel},b}$	mas yr^{-1}	-6.577	-3.987	-0.808	2.379	5.102
All	v_l	km s^{-1}	103.6	161.0	204.9	242.2	281.3
	v_b	km s^{-1}	-101.1	-50.5	-13.6	24.4	77.4
	$\mu_{\mathrm{hel},l}$	mas yr^{-1}	-5.878	-3.457	-1.620	-0.034	1.685
	$\mu_{\mathrm{hel},b}$	mas yr^{-1}	-4.611	-2.462	-0.883	0.737	2.960

3.7 Discussion and Summary

We analyzed the microlensing event OGLE-2018-BLG-1185, which was simultaneously observed from a large number of ground-based telescopes and the *Spitzer* telescope. The ground-based light-curve modeling indicates a low-mass ratio of $q = (6.9 \pm 0.2) \times 10^{-5}$, which is close to the peak of the wide-orbit exoplanet mass-ratio distribution derived by Suzuki et al. (2016) and investigated further by Udalski et al. (2018) and Jung et al. (2019a). Suzuki et al. (2016) derived the wide orbit planet occurrence rate using a sample of 30 planets, primarily from the MOA-II microlensing survey during $2007 - 2012$. The planet presented here, OGLE-2018-BLG-1185Lb, will be included in an extension of the MOA-II statistical analysis (Suzuki et al., in preparation), and its low-mass ratio will help to define the mass-ratio function peak.

From the ground-based light-curve modeling, only the finite source effect is detected, yielding a measurement of the angular Einstein radius. However, the physical properties of the lens as derived from the light curve are unclear because the observed flux variation of the *Spitzer* light curve is marginal. Using only the constraint from the measured angular Einstein radius and a conservative constraint on the change in the *Spitzer* flux, we estimate the host star and planet masses with a Bayesian analysis under the assumption that stars of all masses have an equal probability of hosting the planet. This analysis indicates a host mass of $M_{\rm host} = 0.37^{+0.35}_{-0.21}\ M_\odot$ and a planet mass of $m_p = 8.4^{+7.9}_{-4.7}\ M_\oplus$ located at $D_L = 7.4^{+0.5}_{-0.9}$ kpc. By contrast, the *Spitzer* data favor a larger microlensing parallax, which implies a VLM host with a terrestrial planet ($M_{\rm host} = 0.091^{+0.064}_{-0.018}\ M_\odot$, $m_{\rm p} = 2.1^{+1.5}_{-0.4}\ M_\oplus$) that is either in the disk at $D_{\rm L} \sim 5$ kpc or in the bulge at $D_{\rm L} \sim 7.5$ kpc (these values include a Galactic prior but are not significantly different from the values without the prior; see Table 3.4).

Figure 3.7 compares the Bayesian estimates from the conservative *Spitzer* flux constraint and the full *Spitzer* parallax measurement of the host and planet mass for OGLE-2018-BLG-1185 to those of other planetary systems. The pink circles show the microlens planets without mass measurements, and the red circles show the microlens planets with mass measurements from ground-based orbital parallax effects and/or the detection of the lens flux by high-resolution follow-up observations. The red squares represent microlens planets with mass measurements from the satellite parallax effect observed by *Spitzer*. Figure 3.7 indicates that if the *Spitzer* parallax is correct, this is one of the lowest-mass planets discovered by microlensing.

However, the result that this is a terrestrial planet orbiting a VLM dwarf in the disk should be treated with caution, because the amplitude of the *Spitzer* signal is at the level of systematics seen in other events. A comparison of these properties to the Bayesian posteriors (Figure 3.4) demonstrates that a higher-mass system is preferred given $t_{\rm E}$, $\theta_{\rm E}$, and the Galactic priors. At the same time, a VLM-dwarf + terrestrial planet is still within the 2σ range of possibilities from the Bayesian analysis, especially once the constraint on $\Delta f_{\rm Spz}$ is imposed (Figure 3.6). Furthermore, Shvartzvald et al. (2017b) suggest that such planets might be common. Nevertheless, further investigation is needed in order to assess whether

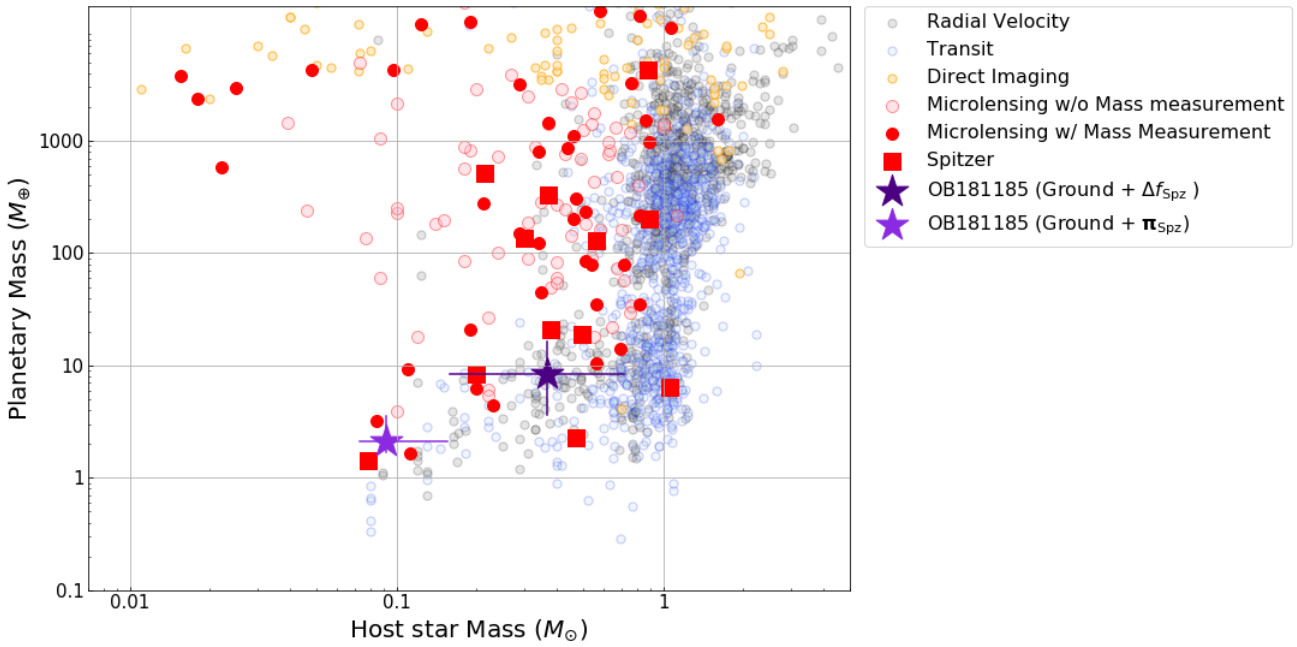

Figure 3.11: The mass distribution of the detected exoplanets as of 2021 February 25 from http://exoplanetarchive.ipac.caltech.edu. The purple stars indicate OGLE-2018-BLG-1185. The pink circles show the microlens planets without mass measurements, and the red circles show the microlens planets with mass measurements from ground-based orbital parallax effects and/or the detection of the lens flux by the high-resolution follow-up observations. The red squares represent the microlens planets with mass measurements from satellite parallax effects by *Spitzer*. The blue, yellow, and black dots indicate planets found by the transit, direct imaging, and radial velocity methods, respectively.

the fitted parallax signal (and so the inferred mass) is real.

Adaptive optics observations are one way to test the *Spitzer* parallax signal. The Bayesian analysis with ground-based + $\Delta f_{\rm Spz}$ constraints indicates the lens K-band magnitude with extinction should be $K = 20.8^{+1.8}_{-1.5}$ mag, which is about 3 magnitudes fainter than the source. By contrast, if the *Spitzer*-"only" parallax is correct and the lens is a VLM dwarf, it should be $K = 23.3^{+2.9}_{-0.8}$ mag and therefore, much fainter and possibly undetectable. The Bayesian estimate of the heliocentric relative proper motion, $\mu_{\rm rel,hel} = 5.0 \pm 0.4$ mas yr^{-1}, predicts that the angular separation between the source and the lens will be ~ 30 mas around mid-2024. Thus, the lens can be resolved from the source by future follow-up observations with Keck or the Extremely Large Telescope. If such resolved measurements were made (and the lens were luminous), it would also lead to a direct measurement of $\boldsymbol{\mu}$. The observed magnitude of $\boldsymbol{\mu}$ can serve as a check on $\theta_{\rm E}$. Additionally, the

direction of $\boldsymbol{\mu}$ is the same as the direction of the microlens parallax vector, which could clarify how the *Spitzer*-"only" parallax contours should be interpreted in the presence of systematics.

If the *Spitzer* parallax is verified, this event confirms the potential of microlensing for measuring the wide-orbit planet frequency into the terrestrial planet regime. Although the number of microlens planets with mass measurements is small for now, observing the satellite parallax effect can continue to increase the number. In particular, this effect can be measured for terrestrial planets by simultaneous observations between the ground and L2 (Gould et al., 2003). This can be achieved with the PRIME telescope (principal investigator: Takahiro, Sumi) and *Roman* Space Telescope (Spergel et al., 2015; Penny et al., 2019) in the mid-2020s.

Chapter 4

Prediction of the Planet Yields by the PRime-focus Infrared Microlensing Experiment

The PRime-focus Infrared Microlensing Experiment (PRIME) will be the first to conduct a dedicated near infrared (NIR) microlensing survey by using a 1.8m telescope with a wide field of view of 1.45 deg^2 at the South African Astronomical Observatory (SAAO). The major goals of the PRIME microlensing survey are to measure the microlensing event rate in the inner Galactic bulge to help design the observing strategy for the exoplanet microlensing survey by the *Nancy Grace Roman Space Telescope* and to make a first statistical measurement of exoplanet demographics in the central bulge fields where optical observations are very difficult owing to the high extinction in these fields. Here we conduct a simulation of the PRIME microlensing survey to estimate its planet yields and determine the optimal survey strategy, using a Galactic model optimized for the inner Galactic bulge. In order to maximize the number of planet detections and the range of planet mass, we compare the planet yields among four observation strategies. Assuming the Cassan et al. (2012) mass function as modified by Penny et al. (2019), we predict that PRIME will detect planetary signals for $42 - 52$ planets ($1 - 2$ planets with $M_p \leq 1M_\oplus$, $22 - 25$ planets with mass $1M_\oplus < M_p \leq 100M_\oplus$, $19 - 25$ planets $100M_\oplus < M_p \leq 10000M_\oplus$), per year depending on the chosen observation strategy.

4.1 Introduction

The number of the detection of exoplanets has exceeded 5,000. Most of these have been discovered via transit and radial velocity methods and have orbital radii and masses different from those of the solar system planets. The microlensing method, in contrast, is complementary to the other methods because it is sensitive to Earth-mass planets (Bennett & Rhie, 1996) beyond the snow-line (Gould & Loeb, 1992), as well as to free floating planets that are not orbiting a host star (Sumi et al., 2011; Mróz et al., 2017; Gould et al., 2022). The snow-line represents the boundary where H_2O becomes ice, outside of which planet formation is pre-

dicted to be most active according to the core accretion model (Lissauer & Stewart, 1993; Pollack et al., 1996). Currently, there are three optical microlensing survey projects; the Microlensing Observations in Astrophysics (MOA; Bond et al., 2001; Sumi et al., 2003), the Optical Gravitational Lensing Experiment (OGLE; Udalski et al., 2015a) and the Korea Microlensing Telescope Network (KMTNet; Kim et al., 2016). Thanks to these survey observations and other follow-up observations, the total number of planets detected via microlensing is 141 as of 2022 November 2[1]. Statistical analyses using microlensing planets provide important findings such as cold planet frequency (Suzuki et al., 2016) and constraints on the dependence of cold planet frequency on the Galactic location (Koshimoto et al., 2021b). Suzuki et al. (2016) measured the mass-ratio function of planets beyond the snow-line using 29 planets discovered by the MOA and other optical microlensing surveys. They found a break, and likely peak in the mass-ratio function near a Neptune mass for the first time. However, there is still a large degree of uncertainty in the location of the break (or peak) in the planet mass-ratio distribution owing to the lack of low-mass planets in their analysis. Recently Zang et al. (2022a) have suggested a possibility that low-mass planets are more abundant than previous results. Their analysis used 13 planets including small mass-ratio planets detected by KMTNet, but did not correct for detection efficiencies. Koshimoto et al. (2021b) used the statistical samples in Suzuki et al. (2016) and showed that there is no strong dependence of the cold planet frequency on the Galactocentric distance.

The inner bulge ($|b| \lesssim 2^\circ$) regions including the Galactic center have remained hidden for the current microlensing survey owing to high extinction. However, these regions are interesting because this is where we expect to find microlensing events in large quantities because of the high stellar density (Gould, 1995). In the near infrared (NIR), light can penetrate through the dust in this region. Comparing the measurements of the planet frequency using an NIR microlensing survey with that determined by the present optical survey, the dependency of planet occurrence on the Galactic structure can be measured, which provides key insights into planetary formation and its history in the Galaxy.

So far, hundreds of microlensing events were discovered in the inner bulge region by the two NIR surveys, VISTA Variables in the Via Lactea Survey (VVV; Minniti et al., 2010) and the United Kingdom Infrared Telescope (UKIRT) Microlensing Survey (Shvartzvald et al., 2017a, 2018). The VVV survey conducts an NIR survey toward the inner Galactic bulge including the Galactic central region and adjacent region of the Galactic plane by using the Visible and Infrared Survey Telescope for Astronomy (VISTA), a 4 m telescope with the 1.6 deg^2 field of view (FOV) VISTA InfraRed Camera (VIRCAM; Emerson & Sutherland, 2010) at ESO's Cerro Paranal Observatory in Chile. Although there are multiple epochs in K_S-band, the survey is not designed for microlensing and the observation cadence was irregular (1/day at best), which is generally inadequate to detect microlensing light curves with features due to planets. However, their survey is sufficient to reveal the number of microlensing events as a function of Galactic longitude and Galactic

[1]https://exoplanetarchive.ipac.caltech.edu/docs/counts_detail.html

latitude. They found the Galactic longitude distribution ($-10.0^\circ < l < 10.44^\circ$) by using 630 microlensing events discovered during $2010-2015$ (Navarro et al., 2018) and the Galactic latitude distribution ($-3.7^\circ < b < 3.9^\circ$) using 360 microlensing events (Navarro et al., 2020). From 2015 to 2018, the UKIRT Microlensing Survey (Shvartzvald et al., 2017a) conducted a microlensing exoplanet survey toward the inner Galactic bulge by using the UKIRT 3.8 m telescope on Mauna Kea, Hawaii with a 0.8 deg^2 FOV infrared camera, Wide Field Camera (WFCAM). The UKIRT microlensing survey observed in H- and K-band filters. UKIRT-2017-BLG-001Lb (Shvartzvald et al., 2018) is the first planet that was found near the Galactic center at $(l, b) = (-0.12^\circ, -0.33^\circ)$ with a high extinction of $A_K = 1.68$. The discovery of UKIRT-2017-BLG-001Lb demonstrated that an NIR survey enables the detection of planets close to the Galactic center with high extinction. Although the above observations have been made, there are still no measurements of microlensing event rates and planet frequency in the inner Galactic bulge.

The *Nancy Grace Roman Space Telescope* is NASA's next flagship mission (Spergel et al., 2015), which is planned to launch in late 2026. It will be placed in a halo orbit around the second Sun-Earth Lagrange Point (L2). The main uses of *Roman* are to study dark energy and to conduct a statistical census of exoplanets by conducting a microlensing survey. *Roman* comprises a 2.4 m telescope with a 0.281 deg^2 wide FOV camera. The *Roman* Galactic Exoplanet Survey (Bennett & Rhie, 2002; Bennett et al., 2010) will comprise 15 minute cadence observations over a few square degrees toward the inner Galactic bulge with a wide W149 filter ($1-2$ μm). Thanks to the high photometric accuracy and continuous observations during 72 days in each of six seasons over five years, *Roman* will detect ~ 1400 cold exoplanets with masses greater than that of Mars ($\sim 0.1 M_\oplus$) including 300 planets with mass of less than $3 M_\oplus$ (Penny et al., 2019). In addition, Johnson et al. (2020) shows that *Roman* would detect ~ 250 free floating planets.

Prior to the microlensing survey by *Roman*, the PRime-focus Infrared Microlensing Experiment (PRIME) will start its NIR microlensing survey toward the inner Galactic bulge in 2023. PRIME will conduct a high-cadence wide FOV survey by using a 1.8m telescope (f/2.29) with 1.45 deg^2 (0.5"/pix) FOV at Sutherland Observatory operated by the South African Astronomical Observatory (SAAO). Half of the observation time will be used for the microlenisng planet survey towards the inner Galactic bulge. The other half will be used for other sciences, such as the transit surveys for M-dwarfs and the transient search for counterparts of high-z gamma-ray bursts and gravitational-wave events.

Here we present results of our simulations that compare four observation strategies for the PRIME microlensing survey and predict the planet yields. In Section 4.2, we introduce the PRIME microlensing survey. Then we explain the methodology of our simulations in order to calculate the detection efficiency of microlensing events and planets in Section 4.3. Next, we calculate star counts, microlensing event rate, detection efficiencies, and detection number of microlensing events and planets for each line of sight over the inner Galactic bulge in Section 4.4. We present microlensing and planet yields depending on four observation strategies in Section 4.5. Finally, we discuss our results and summarize our conclusions in Section 4.6 and Section 4.7.

4.2 PRime-focus Infrared Microlensing Experiment (PRIME)

4.2.1 The PRIME Microlensing Survey

PRIME will be the first dedicated NIR microlensing experiment for the inner Galactic bulge. PRIME will use a NIR camera called PRIME-Cam, consisting of four Teledyne HgCdTe 4K x 4K photodiode array (H4RG-10) detectors with 10 micron pixels. The primary passband for microlensing survey is H-band and Z-, Y-, J-band filters are also used for color measurements. The current plan, which is assumed in our simulations, is that each observation epoch will be composed of twelve 9 second co-added dithered exposures and take 160 sec including overheads (readout time per exposure, 3 sec, slew time for dithering, 1 sec, and slew time for the next field, 4 sec) per exposure. Parameters for the PRIME telescope and PRIME-Cam are summarized in Table 4.1. We note that some parameters in Table 4.1 are current assumptions and are subject to change.

4.2.2 The Goal of the PRIME Microlensing Survey

The main goals of the PRIME microlensing survey are to measure the microlensing event rate in the inner Galactic bulge to help design the observing strategy for *Roman*'s exoplanet microlensing survey and to make a first statistical measurement of exoplanet demographics in the central bulge fields where optical observations are very difficult owing to the high extinction in these fields. By comparing with the planet frequency measured by visible observation, PRIME will reveal the Galactic distribution of planet frequency. PRIME also helps to provide insight into the performance of the H4RG-10 detectors that *Roman* will use. Moreover, after the *Roman* telescope begins to observe, the simultaneous observations of PRIME and *Roman* enable us to measure the microlensing parallax which gives us the mass and distance of lens systems. In particular, observations where the baseline between the Earth and L2 is ~ 0.01 au have a sensitivity to the parallax measurements in timing of a caustic crossing (Wyrzykowski et al., 2020), which is just as sharp a feature as planetary signals, and the parallax measurements down to the free-floating planets regime (Bachelet et al., 2022).

Table 4.1: Adopted Parameters of PRIME microlensing survey

Mirror diameter(m)	1.8
Field of View (deg^2)	1.45
Detectors	4 × H4RG-10
Pixel Scale ($''$/pixel)	0.5
Plate Scale (μm/pixel)	10
Primary bandpass (μm)	1.64±0.30 (H-band)
Exposure time (s)	9
Readout number	3
Stack number	12
Readout noise(counts/pixel)[a]	12.12
Dark(counts/pixel/s)[a]	0.130
QE	0.88[b]
Throughput, η	0.78[c]
Thermal background (counts/pixel/s)	500[d]
Sky background (counts/pixel/s)	5600[e]
Limiting magnitude (mag)	18.5[f](H-band)
Saturation limit (mag)	11.0 (H-band)

[a] The readout noise and dark count value is assumed to be the same as those of the *Roman* telescope as shown in Penny et al. (2019).

[b] Assumed QE in H-band.

[c] Throughput is estimated by multiplying the assumed transmittance of the atmosphere, the measured reflectance of the primary mirror, the measured transmittance of AR coatings, the measured transmittance of the filters, and the assumed detector QE.

[d] Assumed thermal background at 290 K in H-band.

[e] Assumed sky background in H-band.

[f] Faint magnitude limit for a 5σ.

4.3 Simulations

Although an expected microlensing event rate of each field in the inner bulge can be calculated by a model of our Galaxy, we need a survey simulation to obtain detection efficiencies of (i) microlensing events and (ii) planetary events to calculate how many microlensing events and planets are expected to be found by PRIME.

In this section, we present procedure of a Monte Carlo simulation for one year of PRIME observations toward the inner Galactic bulge with 16, 32, 48, and 96 minute cadence observations to estimate the detection efficiencies as a function of field coordinate and observation cadence.

4.3.1 Simulation overview

Figure 4.1 shows a schematic view of our simulation. For each Galactic coordinate and for each observation cadence, a Monte Carlo simulation is performed to calculate the detectability of one hundred thousand microlensing events. A brief explanation of each procedure is presented in the following.

First, we randomly select source and lens objects from each star catalog at specific Galactic coordinates, (l, b), generated from a stellar population synthesis model in our Galaxy. We then assign parameters for single-lens microlensing and binary-lens microlensing with planetary mass-ratios. Synthetic light curves are generated. Each light curve is then modified according to the observation cadence, the parameters of PRIME-Cam and telescope, and observation conditions at Sutherland. Finally, based on the detection criteria, we will examine whether the microlensing events and the planetary signatures can be detected.

4.3.2 Simulation of planetary microlensing events

In this section, we describe how to simulate planetary microlensing light-curves. First, we generate a microlensing event by randomly drawing lens and source stars from catalogs of lens and source stars created by the Galactic model and adding a planet to the lens. Then we compute the parameters of single-lens and binary-lens models which are associated with the physical parameters assigned to the combination of the source and lens. Then, we calculate the magnification of that event as a function of time.

Galactic model and Catalogs of source and lens

Koshimoto et al. (in prep). developed a stellar population synthesis tool, `genstars`[2], which uses a modified version of the Galactic model by Koshimoto et al. (2021a). The modified model is applicable for the inner bulge region because it has a nuclear stellar disk (NSD) structure based on the NSD model by Sormani et al. (2022). The NSD is not included in other population synthesis tools such as the Besançon model (Robin et al., 2003, 2012) or `Galaxia` (Sharma et al., 2011). Thus, `genstars`

[2]The software is available via Zenodo (Koshimoto, 2022) or https://github.com/nkoshimoto/genstars.

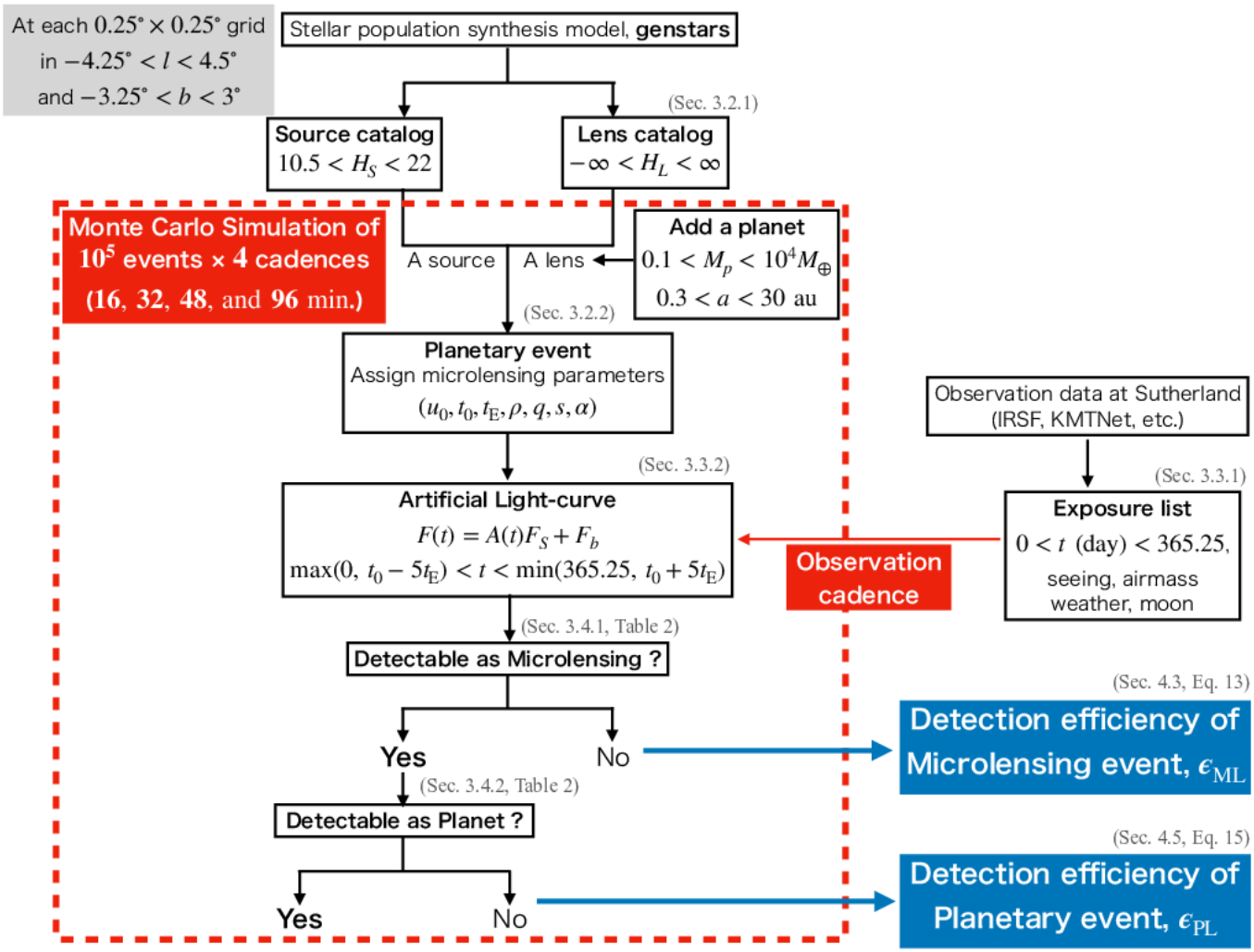

Figure 4.1: Schematic view of our simulation to estimate the detection efficiency of both microlensing events and planets at specific (l, b). For each Galactic coordinate and for each observation cadence, a Monte Carlo simulation is performed to calculate the detectability of one hundred thousand microlensing events.

is currently only the public population synthesis tool suitable for our simulation toward the inner bulge region.

Note that we use a slightly different version of `genstars` from the public version, where the center of our Galaxy is at $(l, b) = (0, 0)$ rather than at Sgr A* at $(l, b) = (-0.056^\circ, -0.046^\circ)$ (Reid & Brunthaler, 2004). The central shift slightly affects our simulation results in the inner NSD region or central ~ 0.5 deg^2. However, the influence is negligible compared to other issues such as the underestimation of extinction in the Galactic central region which is shown in Koshimoto et al. (in prep). This version of their Galactic model will hereafter be referred to as KGM.

In order to simulate the combination of a source and a lens for microlensing events, we use two star catalogs. The first list, the list of source, is selected by specifying a range of magnitudes, $10.5 < H_S < 22$ in the Vega magnitude system within 16 kpc from the Sun. The source list includes stars fainter than PRIME's limiting magnitude, $H_{\rm lim} \sim 18.5$, because they can become bright enough to be detected if sufficiently magnified. The second list, the list of lenses, is selected without magnitude limitations ($-\infty < H_L < \infty$), i.e., including dark objects such as brown dwarfs, white dwarfs, neutron stars, and black holes. Each list contains the following physical parameters of sources or lenses: the magnitude, mass, radius, distance, and proper motions.

Microlensing parameters

A microlensing event occurs when a foreground lens star passes close to the line of sight between an observer and a background source star. The gravity of the lens star bends the light from the source star and magnifies its brightness. The angular Einstein ring radius is given by,

$$\theta_{\rm E} = \sqrt{\kappa M_L \pi_{\rm rel}}, \tag{4.1}$$

where M_L is the mass of the lens object, and $\kappa = 4G(c^2 \text{ au})^{-1} = 8.14 \text{ mas} M_\odot^{-1}$. When the distance from the observer to the lens and source are represented by D_L and D_S, respectively, the lens-source relative parallax is $\pi_{\rm rel} = 1 \text{ au}(D_L^{-1} - D_S^{-1})$.

The magnification of the single-lens light-curve model depends on three parameters: the time of lens-source closest approach t_0, the impact parameter in units of the Einstein radius u_0, and the Einstein radius crossing time $t_{\rm E}$. We also include the finite source effects and introduce one parameter: the ratio of the angular source size to the angular Einstein radius, ρ.

We assume uniform distributions of t_0 and u_0:

$$0 \leq t_0 \leq T_{\rm obs}, \tag{4.2}$$

$$0 \leq u_0 \leq u_{0,\rm max}, \tag{4.3}$$

where we adopt the survey duration $T_{\rm obs} = 365.25$ day. We also adopt the maximum value of impact parameter $u_{0,\rm max} = 1.0$. The events with $u_{0,\rm max} > 1.0$ do not significantly affect the final result because the detection efficiency is lower owing to the low magnification. $t_{\rm E}$ and ρ are derived from the physical parameters assigned to the combination of the source and lens,

$$t_{\rm E} = \frac{\theta_{\rm E}}{\mu_{\rm rel}} \tag{4.4}$$

$$\rho = \frac{\theta_*}{\theta_{\rm E}}, \tag{4.5}$$

where $\mu_{\rm rel}$ is the lens-source relative proper motion drawn from the velocity distribution in the Galactic model. The angular radius of the source star $\theta_* = R_*/D_S$, where R_* is the radius of the source star estimated from the source magnitude from `genstars`. Note that the microlensing event rate is not equal among all the source–lens pairs picked up from the catalogs because it is $\propto \mu_{\rm rel}\theta_{\rm E}$. We will later add this weight when considering the statistics of simulated events.

The magnification of the binary-lens model requires three additional parameters; the planet-host mass ratio, q, the planet-host separation in units of the Einstein radius, s, the angle between the trajectory of the source and the planet-host axis, α. The mass ratio and the planet-host separation are given by

$$q = \frac{M_p}{M_h} \tag{4.6}$$

$$s = \frac{a_\perp}{D_L\theta_{\rm E}}, \tag{4.7}$$

where M_p and M_h are the mass of the planet and the host star, respectively. Assuming a circular orbit, the projected orbital separation $a_\perp = a\sqrt{1-\cos^2\zeta}$, where a is semi major axis and ζ is the angle between the plane of the sky and the binary-axis at a given time. We use a uniform distribution of $\cos\zeta$ assuming a circular planetary orbit that is inclined randomly to the line of sight. We use 21 fixed values of planetary mass distributed logarithmically in the range $0.1 < M_p < 10^4 M_\oplus$ (0.10, 0.18, 0.32, ... , 10000 $M_\oplus$) and 15 fixed values of semi major axis in the range $0.3 < a < 30$ au (0.3, 0.42, 0.58, ... , 30 au). We also assume a uniform distribution of $0 < \alpha < 360$.

Magnification calculation

We calculate the magnification of the single-lens model as a function of time, using either the Yoo et al. (2004) or the Lee et al. (2009) method depending on the value of ρ for the calculation of the finite source with limb darkening as implemented in `MulensModel` (Poleski & Yee, 2019). In order to calculate the magnification of the binary-lens model, we use the advanced contour integration method as implemented in `VBBinaryLensing` (Bozza, 2010; Bozza et al., 2018). In our simulations, we do not consider higher-order effects such as parallax, xallarap, or lens orbital motion.

We note that the magnification of the binary-lens model are calculated to generate synthetic data points in Section 4.3.3 and to examine the validity of planetary signatures in Section 4.3.4. The magnification of the single-lens model are calculated to investigate the detectability of microlensing events and planetary signatures by the χ^2 value of the single-lens model in Section 4.3.4.

4.3.3 Generate synthetic data points

After generating the microlensing models, the next step is to model how the microlensing events are observed by PRIME. We generate the synthetic data points with 16, 32, 48, and 96 minute cadences.

Exposure list

First of all, we make an exposure list of observational parameters such as seeing and airmass for each exposure time ($\sim$ 160 sec). In order to reproduce actual observations, we consider the visibility of the Galactic center, weather, and the days of full moon at Sutherland. The observation toward the inner Galactic bulge is assumed to be conducted when the Sun's altitude is more than 12 degrees below the horizon and when the Galactic center's altitude is more than 20 degrees. Then, we remove the days of the bad weather and three days across the full moon from the set of observable times, based on observation statistics[3] and online data[4] over $2016-2018$. The simulated observable time accounts for $\sim 55-60$ % of the whole night time of the bulge season.

After making the exposure list of the epochs when the Galactic center is visible, we assign the value of airmass and seeing to each exposure time. We calculate airmass from the altitude of the Galactic Center, airmass = sec(z), where z is the zenith angle. We draw the seeing values from the log normal distribution presented in Kato et al. (2007). That work provides an observational seeing distribution under certain airmass conditions obtained observations of the Large Magellanic Cloud from Sutherland with the InfraRed Survey Facility (IRSF). We also consider the airmass dependence of the seeing, airmass$^{0.6}$, given by Woolf (1982).

Flux determination

Now we have the exposure list, where the observational parameters such as exposure epoch, seeing, and airmass are assigned. Then we calculate the flux for each observable data point of a microlensing event. The PRIME photometry will be reduced by using an implementation of the MOA Difference Imaging Analysis (DIA) pipeline (Bond et al., 2001). Since the microlensing survey is conducted toward the inner Galactic bulge, where the optical depth is expected to be high, aperture photometry and point-spread function fitting photometry are known to be less effective in these crowded fields. With the magnification of the source flux as a function of time, $A(t, \boldsymbol{x})$, which is defined the microlensing parameters, $\boldsymbol{x} = (u_0, t_0, t_{\rm E}, \rho, q, s, \alpha)$ described in Section 4.3.2, the total flux of the magnified source, $F(t)$, is given by

$$F(t) = A(t, \boldsymbol{x})F_s + F_b, \tag{4.8}$$

where F_s is the baseline flux of the source star, and F_b is the blend flux which can, in principle include the lens flux.

[3]https://kmtnet.kasi.re.kr/kmtnet-eng/observing-statistics-of-three-sites/
[4]https://kmtnet.kasi.re.kr/ulens/

When we simulate data points for each microlensing event, data points are generated during $T_{\rm min} < t < T_{\rm max}$, where $T_{\rm min} = t_0 - 5t_{\rm E}$ and $T_{\rm max} = t_0 + 5t_{\rm E}$. If $T_{\rm min} < 0$, we use $T_{\rm min} = 0$ and if $T_{\rm max} > 365.25$, we use $T_{\rm max} = 365.25$.

We calculate the source flux, F_s, by combining the H-band magnitude of the source star, H_S generated from `genstars` with the throughput, η in Table 4.1.

To estimate the blending flux F_b, we calculate the lens flux from the H-band magnitude of the lens star, H_L, and the total flux of stars brighter than the limiting magnitude within the PSF, $F_{\rm bright}$. We derive $F_{\rm bright}$ by using the H-band images taken by the VVV survey fourth data release (DR4) (Minniti et al., 2010). We evaluate $F_{\rm bright}$ by subtracting the smooth background flux from the total flux in the region within the typical H-band seeing disc at Sutherland ($\sim 1.4''$). Then, the blending flux, F_b, can be obtained by adding the lens flux and $F_{\rm bright}$ contaminated in the event.

We evaluate the flux uncertainty $F_{\rm err}$ by quasi-smooth backgrounds such as sky backgrounds and faint unresolved stars, and instrumental backgrounds such as thermal background and dark current. These sources of error and their magnitudes are summarized in Table 4.1. The average flux of quasi-smooth background produced by faint unresolved stars, $F_{\rm faint}$ is estimated by the smooth background light in the region within the resolution of the simulation, $0.25^\circ \times 0.25^\circ$ using the H-band images in VVV DR4. We consider both Poisson noise from the total flux, $F(t)$, quasi-smooth backgrounds and instrumental backgrounds and Gaussian noise from the readout noise. It is known that the true photometric errors are underestimated owing to the crowded stellar fields, nearby bright stars, scintillation and flat-fielding, etc. In order to include a fractional systematic uncertainty, we also add 0.3 % of the magnitude in quadrature to each error.

4.3.4 Detection Criteria

Microlensing event

In order to detect planets via microlensing, it is required to detect both the microlensing event itself and to distinguish the planetary perturbations from the single-lens event. We defined five criteria for the detection of microlensing events, which are summarized in Table 4.2. The first criterion is as follows,

$$\Delta\chi^2_{\rm ML} \equiv \chi^2_{\rm const} - \chi^2_{\rm ML} > \Delta\chi^2_{\rm ML,th}, \tag{4.9}$$

where $\chi^2_{\rm const}$ and $\chi^2_{\rm ML}$ is the χ^2 of the best-fit constant flux and best-fit single-lens model, respectively. We use $\Delta\chi^2_{\rm ML,th} = 500$. The second criterion is that there must be more than 100 data points to guarantee modeling accuracy. The third criterion is that there must be data points before and after the peak time of the event, which enhances the accuracy of the parameters measured from the light-curves. The fourth criterion is that the maximum value of the source brightness must be > 5 times larger than the flux error at the time. We note that this criteria is more conservative than criteria that is used in the analysis by KMTNet (Zang et al., 2022a,c). The fifth criterion is that there are at least three consecutive points with the observed flux deviating from the constant baseline by more than

5σ. This requirement is intended to reduce the occasional artifacts on the baseline, like cosmic ray hit. Note that some events passed these criteria thanks to their planetary perturbation. Thus, even events with weak signals from the microlensing event itself have not been missed in our simulations if its planetary signature is sufficiently strong.

Planetary Signature

To estimate the expected yields of the planet detection by the PRIME microlensing survey, we need to set the planet detection criteria. Our criterion for the detection of planetary signature is as follows,

$$\Delta\chi^2_{\rm PL} \equiv \chi^2_{\rm ML} - \chi^2_{\rm PL} > \Delta\chi^2_{\rm PL,th}, \tag{4.10}$$

where $\chi^2_{\rm ML}$ and $\chi^2_{\rm PL}$ is the χ^2 of the best-fit single-lens model and binary-lens model, respectively. We use $\Delta\chi^2_{\rm PL,th} = 160$ following previous microlensing simulation studies (e.g., Bennett & Rhie, 2002; Penny et al., 2013; Henderson et al., 2014).

Although Suzuki et al. (2016) conducted their statistical analysis using a $\Delta\chi^2_{\rm PL}$ threshold of 100 from only MOA survey data, we use $\Delta\chi^2_{\rm PL,th} = 160$ as a conservative assumption in order to consider uncertainties in our simulation. We investigate the impact of changing $\Delta\chi^2_{\rm PL,th}$ on our simulation results. When we use $\Delta\chi^2_{\rm PL,th} = 100$, the detection efficiency of planetary signatures averaged over the planetary masses becomes $\sim 12\%$ higher than that of $\Delta\chi^2_{\rm PL,th} = 160$. As the result, the change of threshold slightly increases the planet detections described in Section 4.5.2. We also estimate the detection efficiency of planetary signatures averaged over the planetary masses for $\Delta\chi^2_{\rm PL,th} = 300$ and find that the detection efficiency become $\sim 16\%$ lower than that of $\Delta\chi^2_{\rm PL,th} = 160$. Despite the lower detection rate, the number of Earth-mass planets to be detected is still more than one. Although the change of threshold affects the planet yields slightly, there is no significant change in the trend in the number of planet detections depending on observation strategies and our results in Section 4.5.2.

4.3.5 Simulated light-curves

Figure 4.2 shows examples of simulated microlensing events in which the planetary signature can be detectable by PRIME. Although the duration of the significant deviation due to the low mass planet is only a few hours (top panels in Figure 4.2), the planetary signature is detectable if there are sufficient observation data. The detection efficiency for high mass planets is high because the duration is a few days (bottom panels in Figure 4.2).

On the contrary, Figure 4.3 shows examples of planetary events whose planetary signatures are missed in our simulation. The artificial event in the top panel is located in a field observed with a 32 minute cadence. The duration of the signature due to a planet with mass of 1 $M_\oplus$ is too short to be detected. The event in the bottom panel of Figure 4.3 has a longer planetary signature due to a 10000 $M_\oplus$ planet. However, the planetary signature is missed because the there are no data points during the period of perturbation.

Table 4.2: Detection criteria

level	criteria	comments
Microlensing	$\Delta\chi^2_{\rm ML} > \Delta\chi^2_{\rm ML,th} = 500$	the χ^2 difference between the best-fit constant flux model and the best-fit single-lens model
	$N_{\rm data} > 100$	Number of data points
	$N_{\rm data,(t<t_0)} \geq 1$ AND $N_{\rm data,(t>t_0)} \geq 1$	there are data points before and after the peak time of the event
	$\max(A(t)F_s/F_{\rm err}) > 5$	the maximum value of the source brightness is 5 times larger than the flux error at the time, t
	$N_{5\sigma} > 3$	there are at least three consecutive points with the observed flux deviating from the constant baseline by more than 5σ
Planet	$\Delta\chi^2_{\rm PL} > \Delta\chi^2_{\rm PL,th} = 160$	the χ^2 difference between the best-fit single-lens model and the binary-lens model

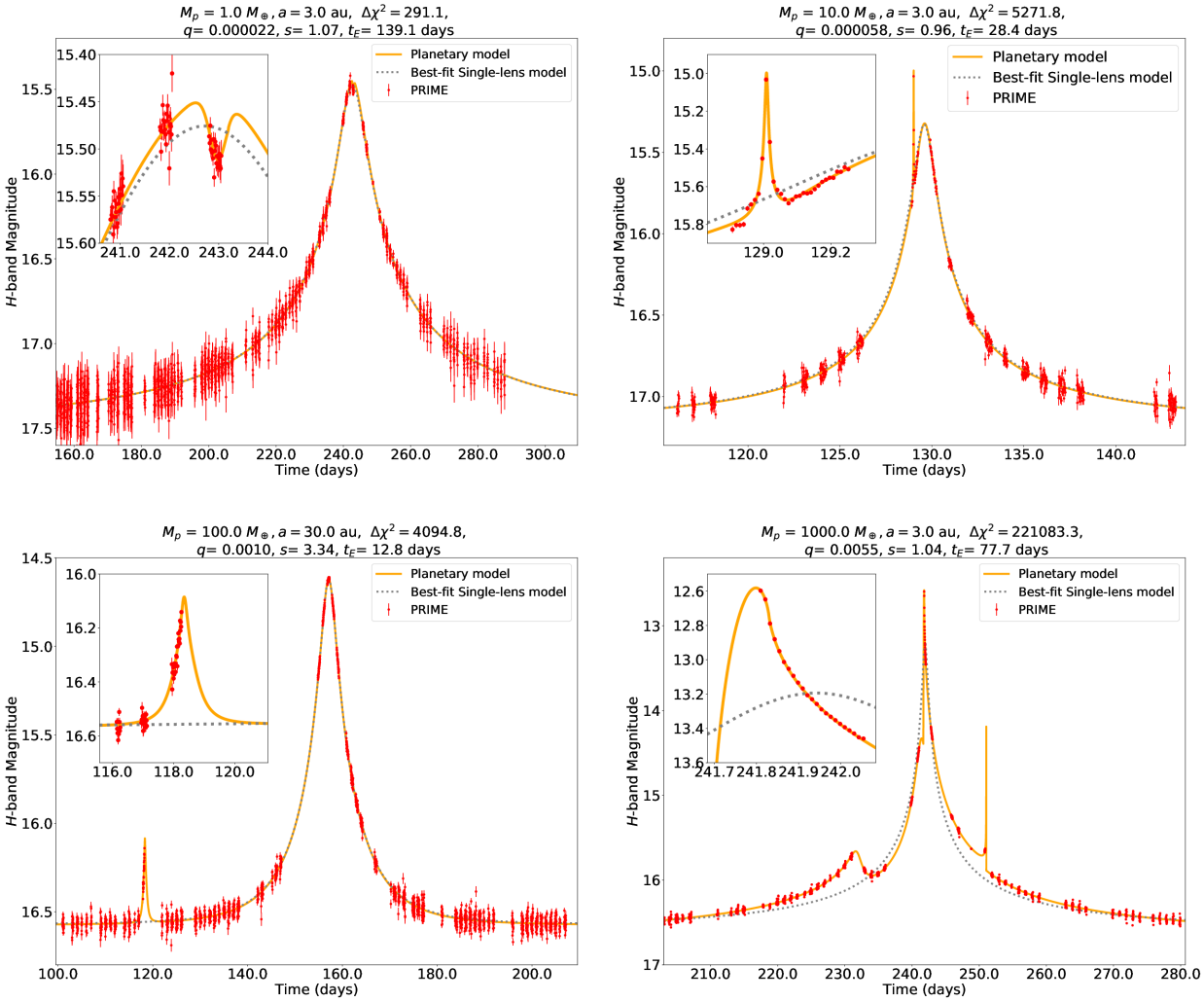

Figure 4.2: Examples of simulated microlensing events whose planetary perturbation are detectable with the PRIME microlensing survey. The insets show the zoom-in of planetary signatures. The red dots show the synthetic data points with a 16 minute cadence. The planetary model for each event is shown in the orange line. The gray dotted lines show the best-fit single lens models.

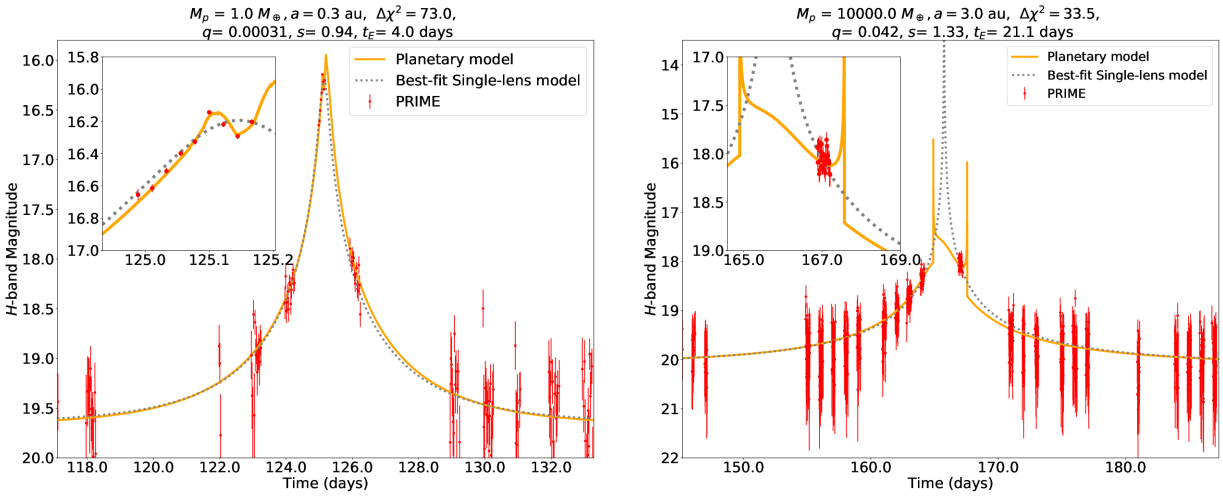

Figure 4.3: Same as Figure 4.2, but for the planetary microlensing events that do not pass the detection criteria of the planetary signatures. Observation cadence is 32 minutes in these examples.

4.4 Statistics of observable microlensing events

By repeating the steps described in the previous section as illustrated in Figure 4.1, we conduct a Monte Carlo simulation of microlensing events and probe their detectability for each specified Galactic longitude and latitude, so that we obtain the expected number of microlensing events and planets.

In the first four subsections, we calculate the number of detections of microlensing events. The yields of microlensing events for each Galactic coordinate per square degree during the survey duration $T_{\rm obs}$, $N_{\rm ML}(l,b)$, are derived by multiplying the number of source stars, $N_{\rm source}(l,b)$, the event rate, $\Gamma_{\rm source}(l,b)$, and the detection efficiency of microlensing events, $\epsilon_{\rm ML}(l,b)$,

$$N_{\rm ML}(l,b) = \Gamma_{\rm source} N_{\rm source} T_{\rm obs} \epsilon_{\rm ML}. \tag{4.11}$$

We show the distribution of $N_{\rm source}$ and $\Gamma_{\rm source}$ for each field at first in Figure 4.4 and Figure 4.6. Then we show the results of the estimation of the detection efficiency and the number of detections of microlensing events as a function of field coordinate and observation cadence in Figure 4.8 and Figure 4.12.

In the last two subsections, we also calculate the number of detections of planets per square degree per year, $N_{\rm PL}(l,b)$ in Figure 4.14, as follows,

$$N_{\rm PL}(l,b) = \int_{a=0.3{\rm au}}^{a=30{\rm au}} \int_{M_p=0.1M_\oplus}^{M_p=10^5 M_\oplus} N_{\rm ML} \epsilon_{\rm PL} f_p d\log(a) d\log(M_p). \tag{4.12}$$

where $\epsilon_{\rm PL}(l,b,a,M_p)$ is the detection efficiency of planets and $f_p[\log(a),\log(M_p)]$ is the cool-planet mass function.

We conduct our simulation for 875 fields over $-4.25^\circ < l < 4.5^\circ$ and $-3.25^\circ < b < 3^\circ$ with a resolution of $0.25^\circ \times 0.25^\circ$. The Surot et al. (2020) extinction map used in `genstars` has up to $0.0025^\circ \times 0.0025^\circ$ resolution. To reduce the computational time without losing the extinction variation, the source and lens catalogs for each grid are drawn by giving the total grid size of $0.25^\circ \times 0.25^\circ$ as the input value for `genstars`, but with the scaling factor $f_{\rm sim} = 0.0032$ that only outputs 0.0032 times the number of stars in the given field. Along each line of sight and each observation cadence, we randomly generate one hundred thousand microlenisng events.

4.4.1 Source star counts

Figure 4.4 shows the KGM stellar density map for stars with $10.5 < H_S < 22$; $N_{\rm source}(l,b)$, calculated from the source catalogs. The star counts per square degree, $N_{\rm source}(l,b)$, along the line of sight is calculated as,

$$N_{\rm source}(l,b) = \frac{N_{\rm sim}}{f_{\rm sim}\delta\Omega_S}, \tag{4.13}$$

where $N_{\rm sim}$ is the number of source stars generated by `genstars`, $\delta\Omega_S = 0.25^\circ \times 0.25^\circ$ is the solid angle within which each source is drawn from `genstars`, and

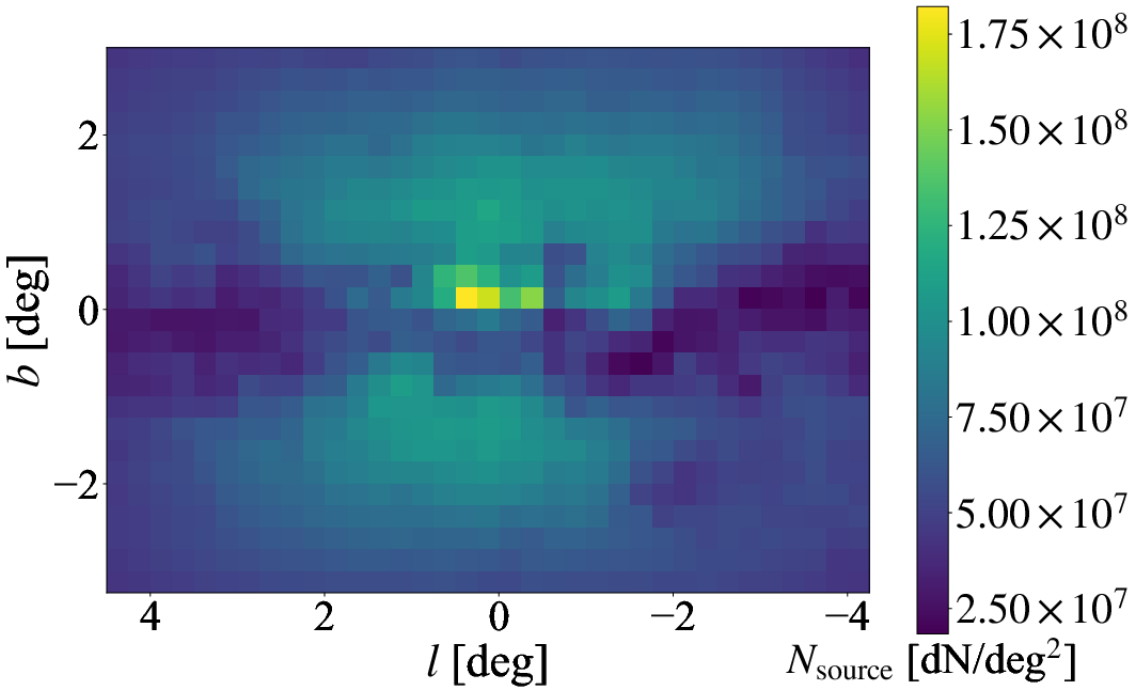

Figure 4.4: Map of star counts with $10.5 < H_s < 22$ mag, $N_{\rm source}(l, b)$, in our source catalogs generated by `genstars`. Most of stars in the region $|b| < 0.5°$ and $|l| < 1.5°$ belong to the NSD component, yielding high stellar density. However owing to the high extinction, the number of source is few in the Galactic center and the Galactic plane.

$f_{\rm sim} = 0.0032$ is the scaling factor that we specified to limit the number of output stars by `genstars`.

Star counts depend on the combination of stellar number density and extinction. Most of stars in the region $|b| < 0.5°$ and $|l| < 1.5°$ belong to the NSD component, yielding a relatively high stellar density. However, owing to high extinction, the number of sources is few in the Galactic center and the Galactic plane. Therefore, according to Figure 4.4, the mean number of stars in the region $-0.75 < b < 0.5$ is $\sim 5.3 \times 10^7$ stars per square degree, which is $\sim 23\%$ and $\sim 12\%$ lower than that in the region $-2.0 < b < -0.75$ and $-3.25 < b < -2.0$, respectively.

We also compare the bulge star counts by KGM with that by observation for validation. Figure 4.5 shows a comparison between luminosity functions in the Stanek window ($l, b = [0.25°, -2.15°]$) predicted by the KGM and as observed by the *Hubble Space Telescope* (*HST*) (Terry et al., 2020). Terry et al. (2020)

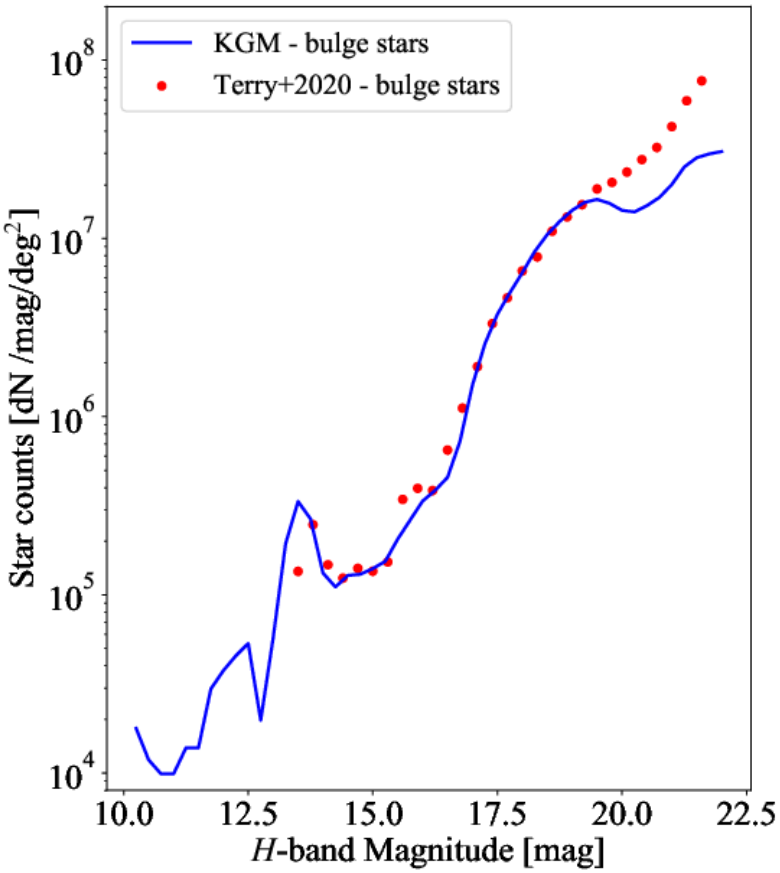

Figure 4.5: Comparison of star counts in Stanek window ($l, b = [0.25°, -2.15°]$) in KGM (blue line) for the bulge population as a function of H-band magnitude to those by HST observation in Terry et al. (2020) (red points). Stars with $H > 19.5$ mag are underestimated in the Galactic model.

distinguished between foreground stars and bulge stars by accurate measurement of the longitudinal proper motion. Although we should use same cut of the proper motion as Terry et al. (2020), here we plot the counts for stars labeled bulge stars in the output catalog by `genstars`.

Figure 4.5 shows that stars with $H \gtrsim 19.5$ mag are underestimated in KGM. However, this discrepancy is not expected to affect simulation results for two reasons. First, at the Galactic center and in the Galactic plane ($|l| < 2°, |b| < 1°$), owing to the high extinction A_H[5] $\sim 1.5 - 3.5$ compared to the extinction in the Stanek window $A_{H,\mathrm{stanek}} \sim 0.68$, the underestimated faint stars are expected to be almost undetectable by PRIME even if the magnification is high. Second, at

[5]We estimate A_H using the Surot et al. (2020)'s $E(J - K_s)$ map and the Nishiyama et al. (2009)'s extinction law.

fields away from the Galactic center (e.g. $|l| < 2^\circ, -2^\circ < b < -1^\circ$), although the extinction ($A_H \sim 0.4 - 1.0$) is almost the same as that at the Stanek window, we expect little effect on the total result because of the small percentage of detectable events with $H_S \gtrsim 19.5$ owing to the low detection efficiency for faint source stars.

4.4.2 Event Rate

The microlensing event rate, $\Gamma_{\rm source}(l, b)$, is the probability that a source star is magnified by a foreground lens star per unit time. The event rate per source is calculated via Monte Carlo integration of the event rate using source and lens catalogs as follows (Awiphan et al., 2016; Penny et al., 2013),

$$\begin{aligned}&\Gamma_{\rm source}(l, b)\\ &= \frac{\Omega_{\rm los}}{f_{\rm sim}\delta\Omega_S}\frac{1}{N_{\rm sim}}\sum^{\rm sources}\left(\frac{1}{f_{\rm sim}\delta\Omega_l}\sum_{D_L<D_S}^{\rm Lenses} 2\theta_{\rm E}\mu_{\rm rel}\right),\end{aligned} \tag{4.14}$$

where $\Omega_{\rm los}$ is the solid angle of each grid, and $\delta\Omega_S$ and $\delta\Omega_L$ are the solid angle of the source and lens catalogs, respectively. In our simulation, we use $\Omega_{\rm los} = \delta\Omega_S = \delta\Omega_L = 0.25^\circ \times 0.25^\circ$.

Figure 4.6 shows the KGM map of event rate per source, $\Gamma_{\rm source}(l, b)$, derived using our source and lens catalogs. According to Figure 4.6, at the NSD region ($|b| < 0.5^\circ, |l| < 1.5^\circ$) the event rate is highest among all fields. This is because $\Gamma_{\rm source}(l, b)$ is mainly determined by stellar density. The mean event rate per source in the region $-0.75 < b < 0.5$ is $\sim 2.5 \times 10^{-5}$, which is $\sim 15\%$ and $\sim 73\%$ higher than that in the region $-2.0 < b < -0.75$ and $-3.25 < b < -2.0$, respectively.

Figure 4.7 compares the model event rate values with the observational values by Mróz et al. (2019). Mróz et al. (2019) shows the optical depth and event rate maps by using the largest sample of 8000 events from the optical survey of OGLE-IV during $2010 - 2017$. Owing to the high extinction around the Galactic center, there is no measurement of event rate at $|b| < 1^\circ$ by OGLE. Outside of the Galactic plane, the two values of event rate are almost coincident, thus we conclude that there is no need of correction for the model event rate values as was done in Penny et al. (2019).

4.4.3 Detection efficiency for microlensing events

We estimate the detection efficiencies for microlensing events, $\epsilon_{\rm ML}(l, b)$ along each line of sight of the inner Galactic bulge. Using the detection criteria described in Section 4.3.4, detection efficiency of microlensing events, $\epsilon_{\rm ML}(l, b)$ is defined as the ratio of the number of detected events to the number of all simulated events and calculated as

$$\epsilon_{\rm ML}(l, b) = \frac{\Sigma_{i,\rm microlensing}\ 2\mu_{{\rm rel},i}\theta_{{\rm E},i}}{\Sigma_{i,\rm all}\ 2\mu_{{\rm rel},i}\theta_{{\rm E},i}}, \tag{4.15}$$

where each event i is weighted by its microlensing event rate ($\propto 2\mu_{{\rm rel},i}\theta_{{\rm E},i}$).

Figure 4.8 shows the mean detection efficiencies of microlensing events along each line of sight with 16, 32, 48, and 96 minute cadences. At the same observation

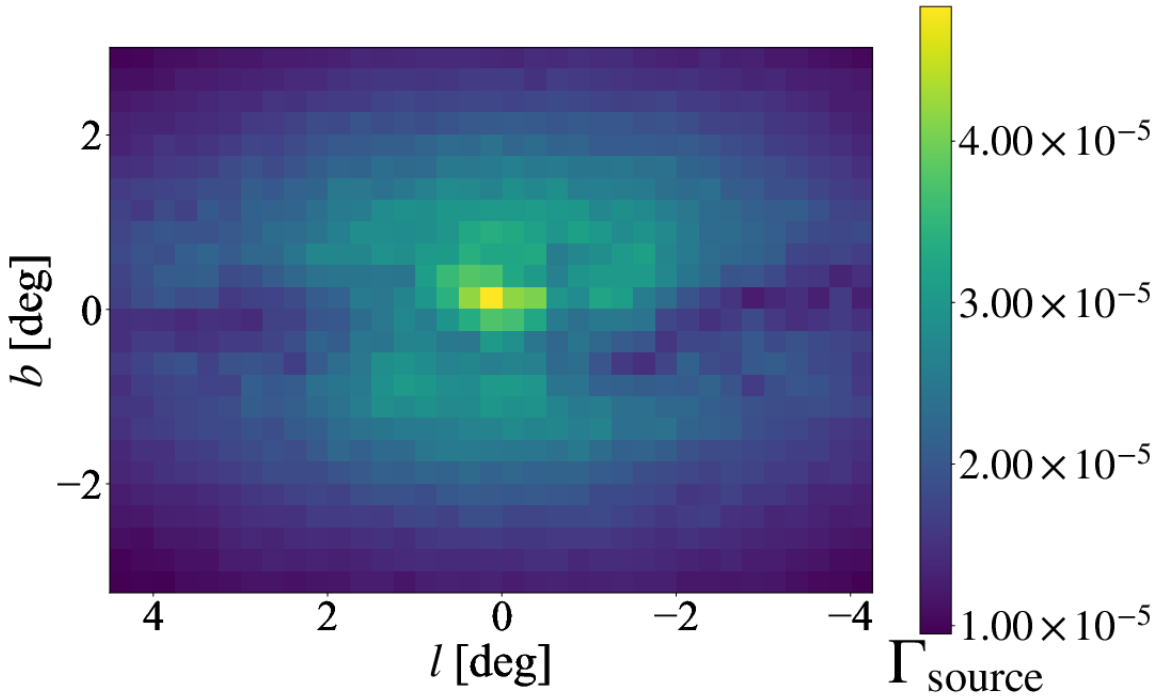

Figure 4.6: Map of event rate per source, $\Gamma_{\rm source}$, calculated using source and lens catalogs, generated by `genstars`. Event rate per source are mainly determined by the stellar density, so at the NSD region ($|b| < 0.5°, |l| < 1.5°$) the event rate is highest among other fields.

cadence, detection efficiency is lower at the Galactic center than away from the Galactic center. The mean number of detection efficiencies with a 16 minute cadence in the region $-0.75 < b < 0.5$ is ~ 0.07, which is $\sim 29\%$ and $\sim 43\%$ lower than that in the region $-2.0 < b < -0.75$ and $-3.25 < b < -2.0$, respectively. There are two reasons why the mean detection efficiency of microlensing events is lower at the Galactic center. The first reason is the large fraction of short $t_{\rm E}$ events at the Galactic center. The top panels in Figure 4.9 show $t_{\rm E}$ distributions for all simulated events (red histogram) and detected events (blue histogram) at two Galactic coordinates. The median value of $t_{\rm E}$ at $(l, b) = (0.125°, -0.125°)$, is ~ 5.1 days, which is smaller than ~ 9.7 days at $(l, b) = (0.125°, -2.625°)$, because the majority of events toward the former direction comprise a source and a lens located in the bulge, yielding the small lens-source relative parallax, $\pi_{\rm rel}$ and small angular Einstein ring radius $\theta_{\rm E}$ (Equations (4.1) and (4.4)). Microlensing events with short $t_{\rm E}$ are detected less efficiently by the survey as indicated by the green lines in Figure 4.9. Therefore the mean detection efficiency, $\epsilon_{\rm ML}$, at $(l, b) = (0.125°, -0.125°)$, is

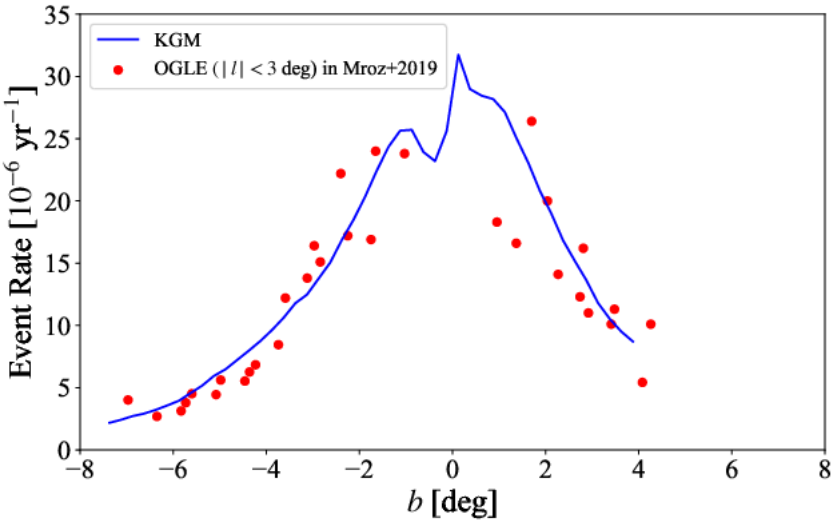

Figure 4.7: Comparison of the event rate per source calculated from the source and lens catalogs from `genstars` (blue line) with that measured in Mróz et al. (2019) (red points). Due to the high extinction around the Galactic plane, there is no measurement of event rate at $|b| < 1^\circ$ by OGLE. Outside of the Galactic plane, the two values of event rate are almost coincident.

lower than that at $(l, b) = (0.125^\circ, -2.625^\circ)$. The second reason is the large fraction of faint stars owing to the high extinction at the Galactic center. The top panels in Figure 4.10 show the luminosity functions for both the all simulated events (red histogram) and detected events (blue histogram) in the same Galactic coordinates as Figure 4.9. The estimated extinction values are $A_H \sim 4.4$ and $A_H \sim 0.7$ for at $(l, b) = (0.125^\circ, -0.125^\circ)$ and at $(l, b) = (0.125^\circ, -2.625^\circ)$, respectively. The detection efficiency as a function of H_S is lower for faint stars than for bright stars as indicated by the green lines in Figure 4.10. The fraction of faint sources with $H_S > 17.5$ in all events, which are lower $\epsilon_{\rm ML}$, is $\sim 30\%$ and $\sim 6\%$, at $(l, b) = (0.125^\circ, -0.125^\circ)$ and $(l, b) = (0.125^\circ, -2.625^\circ)$, respectively. Therefore, owing to high extinction, the large fraction of faint stars, whose detection efficiency is low, also results in low mean detection efficiency at the Galactic center.

Figure 4.8 also shows that, at the same field, the lower the cadence, the lower the detection efficiency. Compared to the mean detection efficiency in the same region with a 16 minute cadence, the detection efficiencies are $\sim 9\%$, 17%, 33% lower with 32, 48, 96 minute cadences, respectively.

In Figure 4.11, we plot the detection efficiency of microlensing events depending on the Einstein crossing time, $t_{\rm E}$. As expected, the detection efficiency becomes lower near the Galactic center and/or with lower cadence. It is difficult to detect microlensing events with $t_{\rm E} \lesssim$ 0.3, 0.6, 1, and 3 days when the observation cadence is 16, 32, 48, and 96 minutes, respectively.

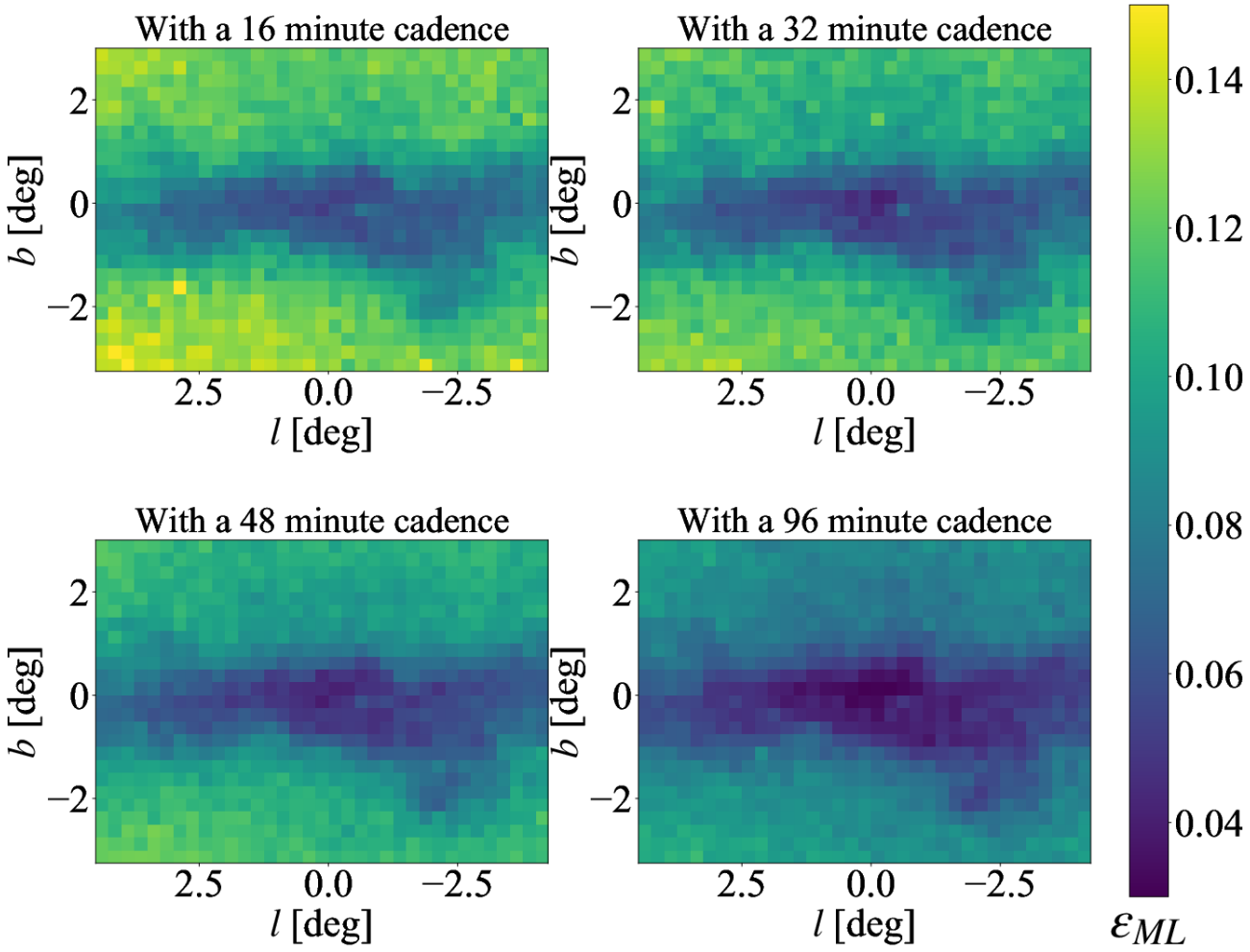

Figure 4.8: Mean detection efficiency of microlenisng events along each line of sight, $\epsilon_{\rm ML}(l, b)$. Each plot shows the detection efficiency for different cadences. With the same observation cadence, the detection efficiency is lower at the Galactic center than away from the Galactic center. See the text for an explanation of these trends. At the same field, the lower the observation cadence, the lower the detection efficiency.

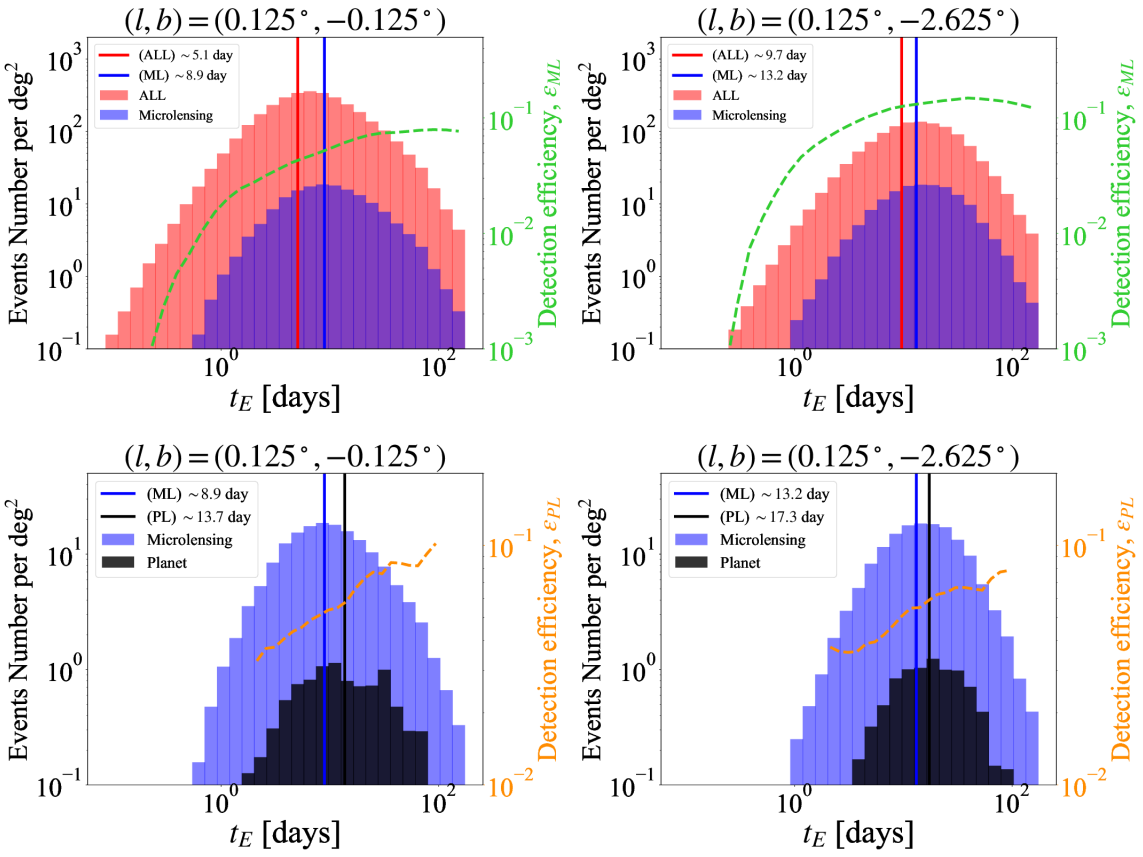

Figure 4.9: The Einstein ring crossing time, $t_{\rm E}$, distribution at $(l, b) = (0.125^\circ, -0.125^\circ)$ (left panels) and at $(l, b) = (0.125^\circ, -2.625^\circ)$ (right panels). Top panels show the distribution of all simulated events (red) and detected microlensing events (blue) with a 16 minute cadence by the assumed PRIME survey. Bottom panels show the distribution of detected microlensing events (blue) and detected planetary events (black). The vertical lines show the median value of each histogram. The dashed green and orange lines show the detection efficiency of microlensing events and planetary events depending on $t_{\rm E}$, respectively.

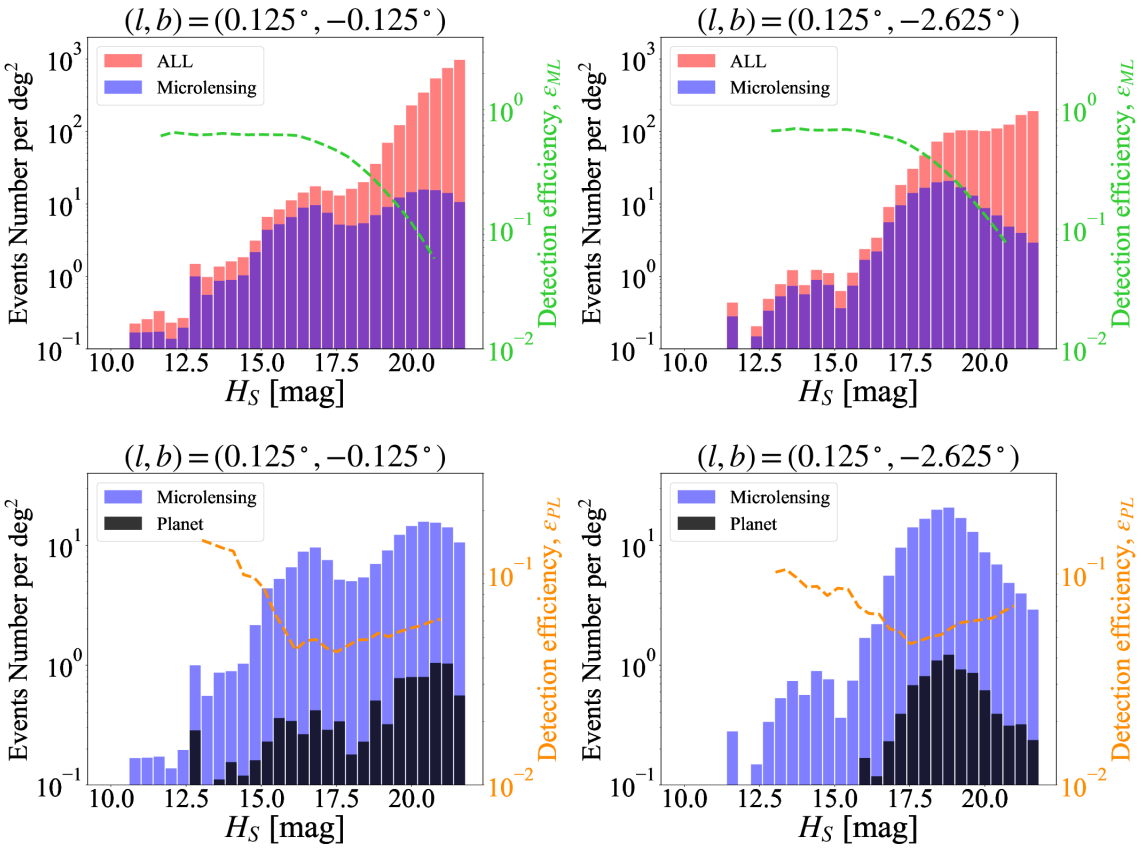

Figure 4.10: The source magnitude, H_S, distribution at $(l, b) = (0.125^\circ, -0.125^\circ)$ (left panels) and at $(l, b) = (0.125^\circ, -2.625^\circ)$ (right panels). Top panels show the distribution of all simulated events (red) and detected microlensing events (blue) with a 16 minute cadence. Bottom panels show the distribution of detected microlensing events (blue) and detected planetary events (black). The dashed green and orange lines show the detection efficiency of microlensing events and planetary events depending on H_S, respectively.

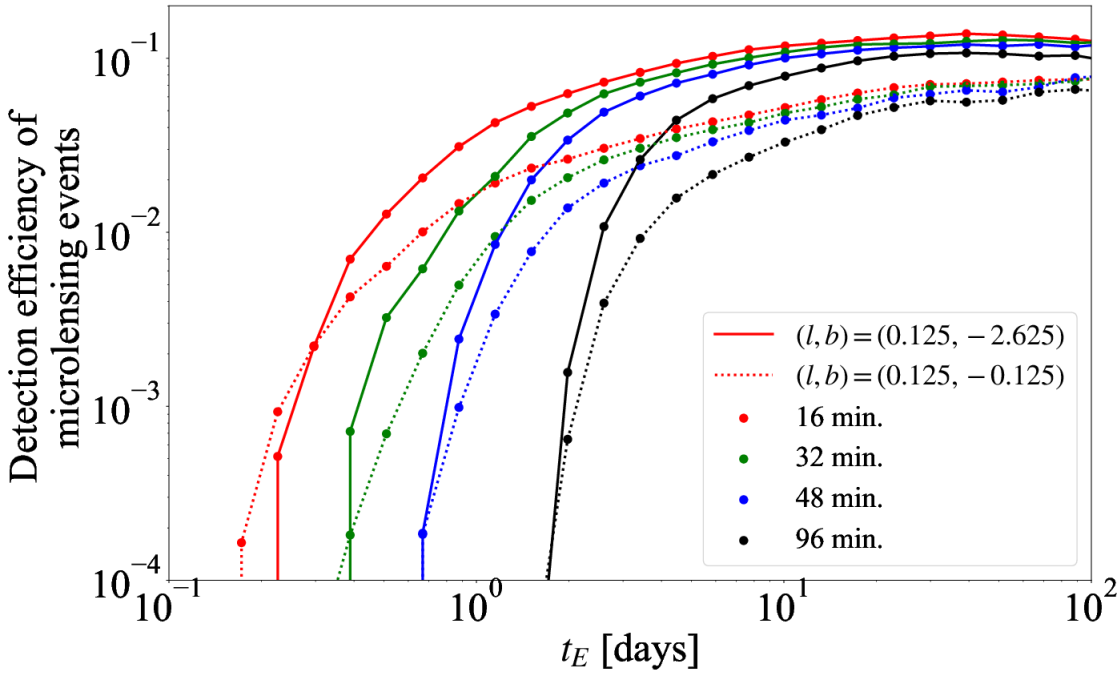

Figure 4.11: The detection efficiency of microlensing events depending on $t_{\rm E}$. The solid and dotted lines show the detection efficiency away from the Galactic center, $(l, b) = (0.125, -2.625)$, and at the Galactic center, $(l, b) = (0.125, -0.125)$, respectively. The detection efficiency with 16, 32, 48, and 96 minute cadences are shown in red, green, blue, and black, respectively.

4.4.4 The Number of Detected Microlensing events

Figure 4.12 shows the yields of microlensing events for each Galactic coordinate per square degree for one year, $N_{\rm ML}(l, b)$, calculated by Equation (4.11). According to Figure 4.12, the mean number of microlensing yields with a 16 minute cadence in the region $-0.75 < b < 0.5$ is ~ 93 events per square degree, which is $\sim 41\%$ and $\sim 18\%$ lower than that in the region $-2.0 < b < -0.75$ and $-3.25 < b < -2.0$, respectively. Compared to the microlensing yields in the same region with a 16 minute cadence, the yields are $\sim 10\%$, 18%, 35% lower with 32, 48, 96 minute cadences, respectively.

4.4.5 Detection efficiency for planetary signatures

We also estimate the detection efficiencies of the planetary signatures $\epsilon_{\rm PL}(l, b, a, M_p)$ along each line of sight. Following the detection criteria of planetary signatures described in Section 4.3.4, detection efficiency of a planetary signature is defined as the ratio of the number of detected planetary events to the number of detected

events as microlensing

$$\epsilon_{\rm PL}(l, b, a, M_p) = \frac{\Sigma_{i,\rm planet}\ 2\mu_{{\rm rel},i}\theta_{{\rm E},i}}{\Sigma_{i,\rm microlensing}\ 2\mu_{{\rm rel},i}\theta_{{\rm E},i}}. \tag{4.16}$$

Figure 4.13 shows the detection efficiency of planetary signatures, $\epsilon_{\rm PL}(M_p)$, as a function of planet mass, which are obtained by averaging over all 875 fields and are summed across semi-major axis, $0.3 < a < 30$ au. With a 16 minute cadence, the detection efficiencies of Jupiter mass planet, Neptune mass, and Earth mass planet are ~ 0.05, ~ 0.007, and ~ 0.0006, respectively. Compared to the detection efficiency with a 16 minute cadence, the detection efficiency is $\sim 15-20\%$, $\sim 30-50\%$, and $\sim 50-70\%$ lower with 32, 48, and 96 minute cadences, respectively. In addition, the degree of decrease in detection efficiency with observation cadence is greater for low-mass planets.

We note that detection efficiency of the planetary signature can be regarded as almost the same over all fields simulated, owing to the combination of $t_{\rm E}$ distributions and luminosity functions. Firstly, at the Galactic center, the fraction of short $t_{\rm E}$ events is larger than that away from the Galactic center. The bottom panels in Figure 4.9 show $t_{\rm E}$ distributions for both the detected microlensing events (blue histogram) and detected planetary events (black histogram) at two Galactic coordinates. The median values of $t_{\rm E}$ for microlensing events at $(l, b) = (0.125^\circ, -0.125^\circ)$, is ~ 8.9 days, which is smaller than ~ 13.2 days at $(l, b) = (0.125^\circ, -2.625^\circ)$. Planetary events with short $t_{\rm E}$ are detected less efficiently by the survey, see the lines in Figure 4.9 describing $\epsilon_{\rm PL}$, as well as the detection efficiency of microlensing events, $\epsilon_{\rm ML}$. Secondly, the fraction of bright stars at $(l, b) = (0.125^\circ, -0.125^\circ)$ is larger than that at $(l, b) = (0.125^\circ, -2.625^\circ)$. The bottom panels in Figure 4.10 show the luminosity functions for both the detected microlensing events (blue histogram) and detected planetary events (black histogram). The detection efficiency of planetary signatures, $\epsilon_{\rm PL}$ as a function of H_S changes little for faint stars with $H_S > 16$, but are higher for bright stars with $H_S < 16$ as indicated by the lines in Figure 4.10. The fraction of bright sources with $H_S < 16$ in microlensing events, which are higher $\epsilon_{\rm PL}$, is $\sim 20\%$ and $\sim 7\%$, at $(l, b) = (0.125^\circ, -0.125^\circ)$ and $(l, b) = (0.125^\circ, -2.625^\circ)$, respectively. Therefore, the $\epsilon_{\rm PL}$ difference depending on Galactic coordinates are minimized by the combination of the large fraction of short $t_{\rm E}$ events, which work to decrease mean detection efficiency, and the large fraction of bright stars, which work to increase mean detection efficiency, in microlenisng events at the Galactic center.

4.4.6 The Number of Detected Planets

We calculate the number of the detectable planets per square degree per year, $N_{\rm PL}(l, b)$, by Equation (4.12). We use the Cassan et al. (2012) mass function of planets beyond snow-line as modified by Penny et al. (2019), which shows planet frequency per decade of mass and semi-major axis by using planets detected via microlensing. Because Cassan et al. (2012) has no detection of a planet with a mass less than 5 $M_\oplus$, we decided to use a constant value, $\sim$ two planets per dex^2,

below 5 $M_\oplus$ following Henderson et al. (2014) and Penny et al. (2013, 2019). The mass function finally used can be stated as,

$$f_p[\log(a), \log(M_p)] \equiv \frac{d^2N}{d\log(a)d\log(M_p)}$$
$$= \begin{cases} 0.24 \text{ dex}^{-2} \left(\frac{M_p}{95M_\oplus}\right)^{-0.73} & \text{if } M_p \geq 5M_\oplus, \\ 2 \text{ dex}^{-2} & \text{if } M_p < 5M_\oplus. \end{cases} \tag{4.17}$$

Figure 4.14 shows the planet detection maps computed using Equation (4.12) along each line of sight. According to Figure 4.14, the mean number of planet yields with a 16 minute cadence in the region $-0.75 < b < 0.5$ is ~ 1.6 events per square degree, which is $\sim 41\%$ and $\sim 18\%$ lower than that in the region $-2.0 < b < -0.75$ and $-3.25 < b < -2.0$, respectively. Compared to the planet yields in the same region with a 16 minute cadence, the yields are $\sim 31\%$, 46%, 70% lower with 32, 48, 96 minute cadences, respectively.

The planet detection map with a 16 minute cadence (upper left panel in Figure 4.14) is used to determine the order of the observation fields in next section. The field numbers are ranked by high expectation number of planet detections summed across each PRIME FOV.

We investigate the impact of assuming other planet frequencies via microlensing as given in Suzuki et al. (2016) and Shvartzvald et al. (2016). Figure 21 in Penny et al. (2019) shows a comparison of modified planet frequency based on Cassan et al. (2012) to the latest measurements of mass-ratio function by microlensing surveys (Suzuki et al., 2016; Shvartzvald et al., 2016). They assumed a $0.5M_\odot$ host star to convert mass-ratio to planet mass. The frequencies of low-mass planets ($M_p \lesssim 30M_\oplus$) obtained in Suzuki et al. (2016) is lower than the modified planet frequency, which suggests lower yields of low-mass planets. However the frequency of Earth-mass planet is still not well understood owing to the lack of low-mass planets in the statistical analyses. The frequencies of high-mass planets ($3000 < M_p/M_\oplus < 10000$) obtained in Shvartzvald et al. (2016) is higher than the modified planet frequency, which suggests that the modified planet distributions underestimates planet yields for high-mass planets.

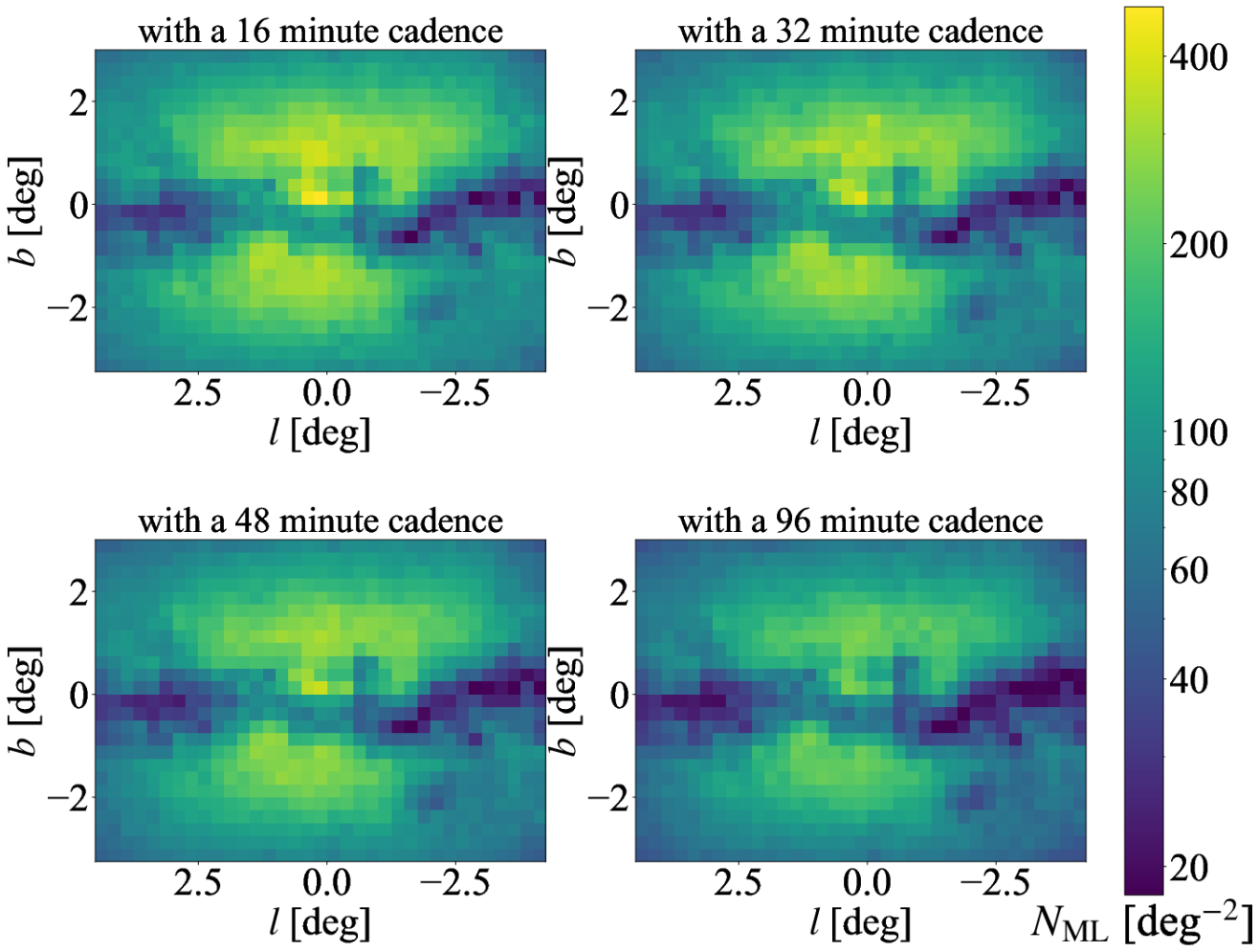

Figure 4.12: Microlensing detection maps along each line of sight. Each plot shows the number of detections with 16, 32, 48, and 96 minute cadences. This figure is obtained by multiplying star counts, N_{source}, (Figure 4.4), event rate, Γ_{source}, (Figure 4.6) and mean detection efficiency of microlenising events, ϵ_{ML}, (Figure 4.8).

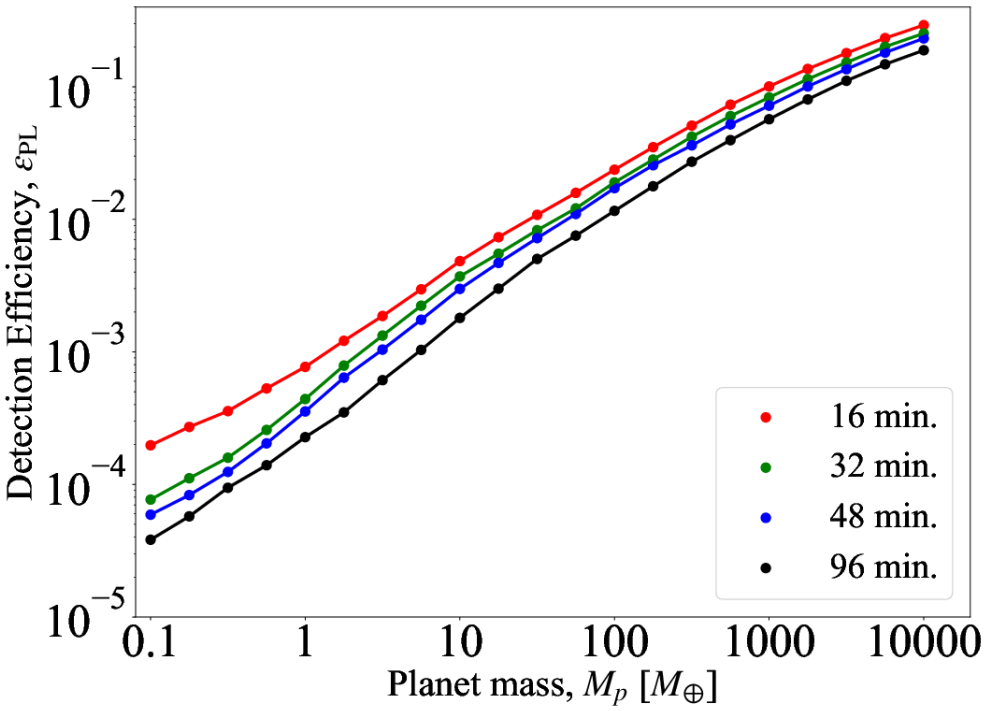

Figure 4.13: The detection efficiency of planetary signatures, $\epsilon_{\rm PL}(M_p)$ depending on planet mass, which are obtained by taking the average of all 875 fields and are summed across semi-major axis, $0.3 < a < 30$ au. Red, green, blue, and black color plots shows detection efficiency with 16, 32, 48, and 96 minute cadences, respectively.

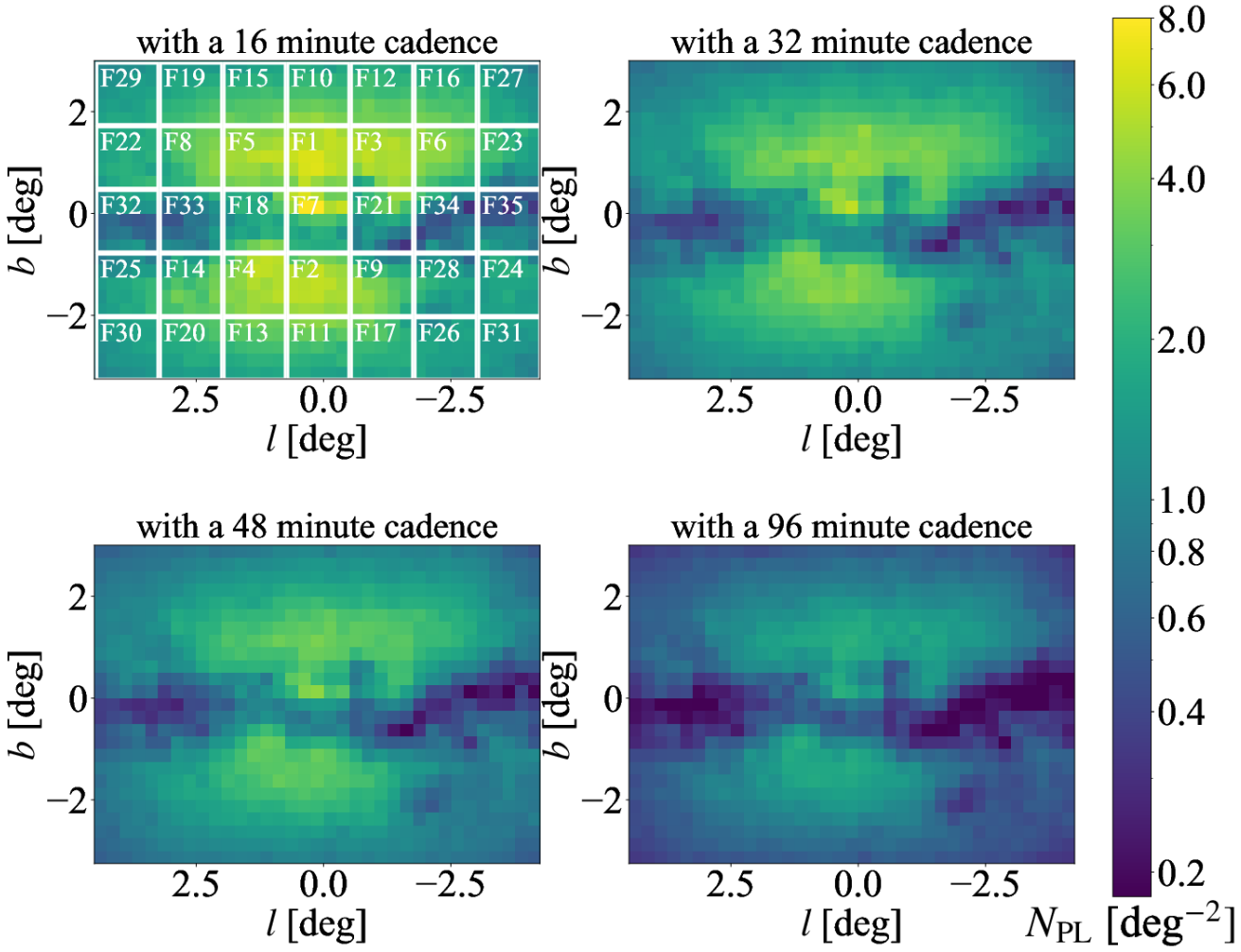

Figure 4.14: Planet detection maps along each line of sight. Each plot shows the number of detections with 16, 32, 48, and 96 minute cadences. This figure is obtained by multiplying the number of microlensing detections, $N_{\rm ML}(l, b)$, (Figure 4.12) and the mean detection efficiency of planets, $\epsilon_{\rm PL}$, which is obtained by the averaging over all fields, over mass of $0.1 < M_p < 10^5 M_\oplus$, and semi-major axis of $0.3 < a < 30$ au and corrected by a modified cool-planet frequency based on Penny et al. (2019). The planet detection map with a 16 minute cadence (upper left panel) is used to determine the order of the observation fields to in Section 4.5.1. Each white square shows a 1.45 deg^2 FOV field. The field numbers are ranked by the expected number of planet detections summed across each square.

4.5 Observation Strategies and yields

Now that we have the expected number of microlensing events and planets as a function of Galactic coordinate and observation cadence, we are finally ready for discussing the PRIME survey strategy. In this section, we define four observation strategies and calculate both microlensing yields and planet yields depending on each observation strategy.

4.5.1 Observation fields and strategies

We divide our simulation fields ($|b| \lesssim 2^\circ$, $|l| \lesssim 4^\circ$) into 35 observation fields according to the size of the PRIME FOV and calculate the total number of planets expected to be detected in each observation field. Then the observation field numbers are ranked in order of these total number of detections (upper left panel in Figure 4.14). Because the number of observation fields we can observe is determined by the observation cadence, we define four strategies as following and compare the planet yields among these four strategies:

S1 6 fields (F1–F6) with a 16 minute cadence

S2 12 fields (F1–F12) with a 32 minute cadence

S3 18 fields (F1–F18) with a 48 minute cadence

S4 18 fields (F1–F18) with a hybrid cadence (16min cadence for F1–F3, 48min cadence for F4–6, 96min cadence for the other 12 fields),

where we assumed that it takes 160 secs in total to observe a field (exposure + overheads) to calculate the cadence. Figure 4.15 shows all the 18 fields (F1–F18) considered here as well as which fields are observed by each strategy. As shown in the figure, the S1, S2, and S3 strategies each have different survey regions and monitor all the fields in each region equally. The S4 strategy has the same survey region as S3, but each field is monitored with different cadence. We call S4 a hybrid strategy.

We consider these different strategies because there is a trade-off between the number of fields and frequency of observations. On the one hand, an increase of the number of fields allows us to monitor more sources, which will yield a lot of microlensing events. On the other hand, a higher cadence observation has a higher sensitivity to low-mass planets, because the timescales of the planetary signature scales with $\sqrt{q}t_{\rm E}$. The typical timescales of planetary signatures for Jupiter-mass planets and Earth-mass planets are a few days and a few hours, respectively. Thus high cadence observations are required in order to detect Earth-mass planets, and it is unclear which strategy yields planet discoveries most efficiently including small mass planets without doing a simulation. However the following concerns caused by observations with a lower cadence are not considered in this study. Lower cadence observations make it more difficult to measure the source radius crossing time, $\theta_*(\equiv \rho t_{\rm E})$, and therefore $\theta_{\rm E}$. So it is more challenging to measure host and

Table 4.3: Best-estimate Planet Yields per year by the PRIME microlensing survey

Strategy	S1	S2	S3	S4	Uniform
Total field number	6	12	18	18	18
Area($\deg^2$)	8.7	17.5	26.2	26.2	26.2
Mass($M_\oplus$)					
$0.1 < M_p \leq 1.0$	1.8	1.3	1.3	1.7	1.6
$1.0 < M_p \leq 10$	8.7	9.5	9.2	9.0	8.4
$10 < M_p \leq 100$	13.0	14.9	16.0	15.0	13.8
$100 < M_p \leq 1000$	11.3	13.9	15.0	14.1	12.8
$1000 < M_p \leq 10000$	7.5	9.6	10.4	10.0	9.0
Total ($10^{-1} - 10^4 M_\oplus$)	42.4	49.1	51.8	49.8	45.6
Total Microlensing	~ 2300	~ 3400	~ 4100	~ 3900	~ 3400

planet masses either by a combination of $\theta_{\rm E}$ and $\pi_{\rm E}$ measurements (as in Muraki et al., 2011) or with the color dependent centroid shift (Bennett et al., 2006; Dong et al., 2009).

Note that this chapter is primarily concerned with the search for an optimal observation strategy with the goal of increasing planet yields to measure the planet frequency in the inner Galactic bulge. However we will discuss other observation strategies in Section 4.6.1, including a uniform survey that monitors a large contiguous area around the inner Galactic bulge, in order to measure the NIR event rate map to help optimize the choice of *Roman* microlensing survey fields.

4.5.2 Yields

Table 4.3 shows our estimation of the number of microlensing events and the number of planets detected by the PRIME microlensing survey assuming the Cassan et al. (2012) mass function as modified by Penny et al. (2019) (Equation 4.17) over a certain mass range. The total number of microlensing events detected are $\sim$ 2300, 3400, 4100, and 3900, for the S1, S2, S3, and S4 strategies, respectively. The impact of increasing the number of sources by observing more fields is more significant than the impact of decreasing the detection efficiencies by observing with lower cadence.

In Figure 4.16, we plot the planet detection rate per dex for four observation strategies, calculated by the sum of the semi-major axis over $0.3 < a < 30$ au and the sum of the survey area ($8.7 - 26.2$ $\deg^2$) shown in Table 4.3). In order to detect low mass planets, high cadence observations are required (S1), while in order to detect high mass planets, observing a larger number of fields is more important than observing with a higher cadence (S2 and S3). When we use a hybrid observation cadences (S4), it is possible to detect both low mass planets and high mass planets. The lower panel in Figure 4.16 shows the detection rates of each strategy relative to that of S4. As the result, we predict that PRIME will discover $42 - 52$ planets ($1 - 2$ planets with $M_p \leq M_\oplus$, $22 - 25$ planets with mass $1M_\oplus < M_p \leq 100M_\oplus$, $19 - 25$ planets $100M_\oplus < M_p \leq 10000M_\oplus$), per year depending on each observation strategy.

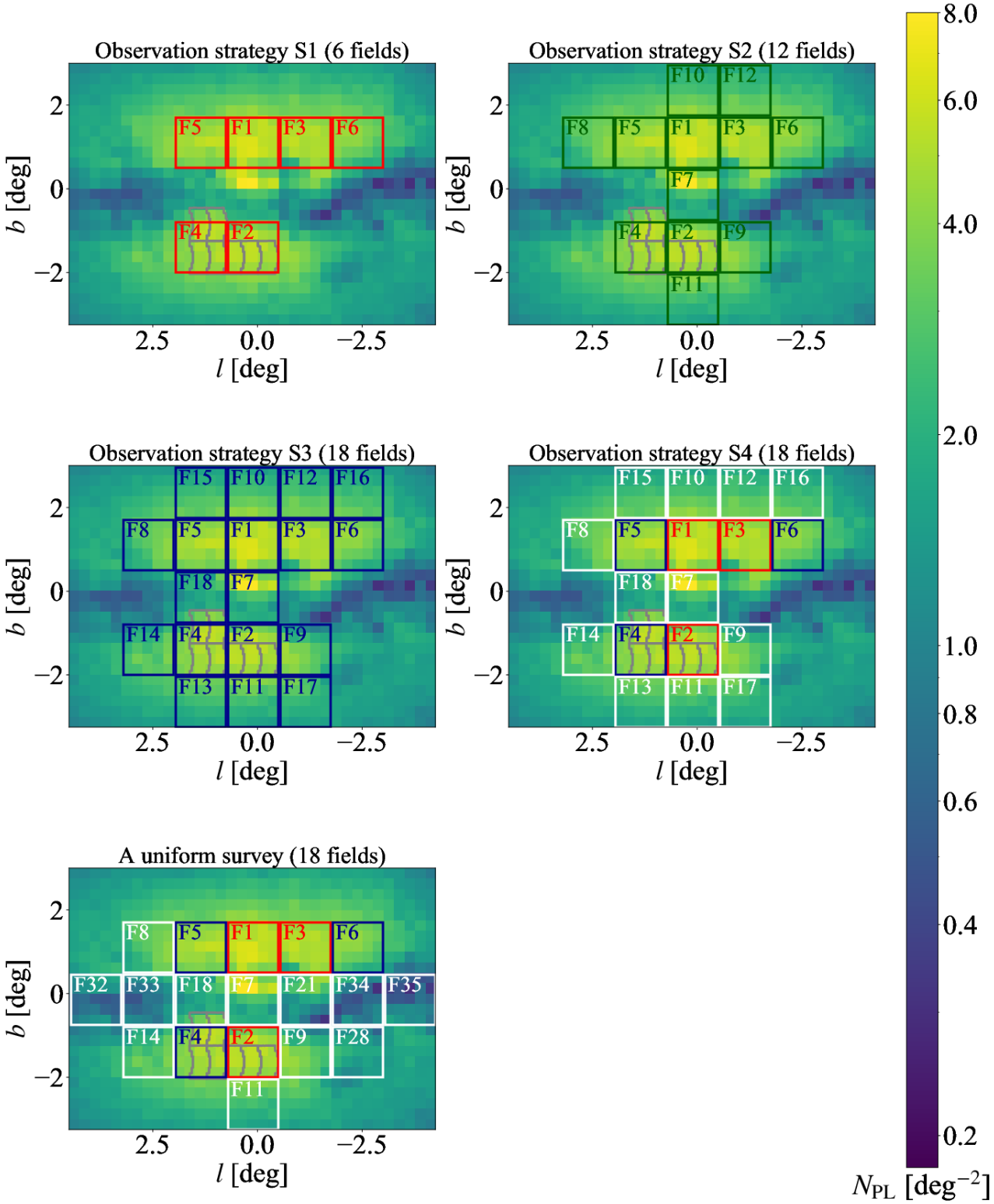

Figure 4.15: Field locations for the PRIME microlensing survey for each observation strategy considered in this work, plotted over the planet detection map with a 16 minute cadence. Top and middle panels show the observation strategies, S1–S4 described in Section 4.5.1. The bottom panel shows the spatially uniform survey including the Galactic center and the Galactic plane described in Section 4.6.1.

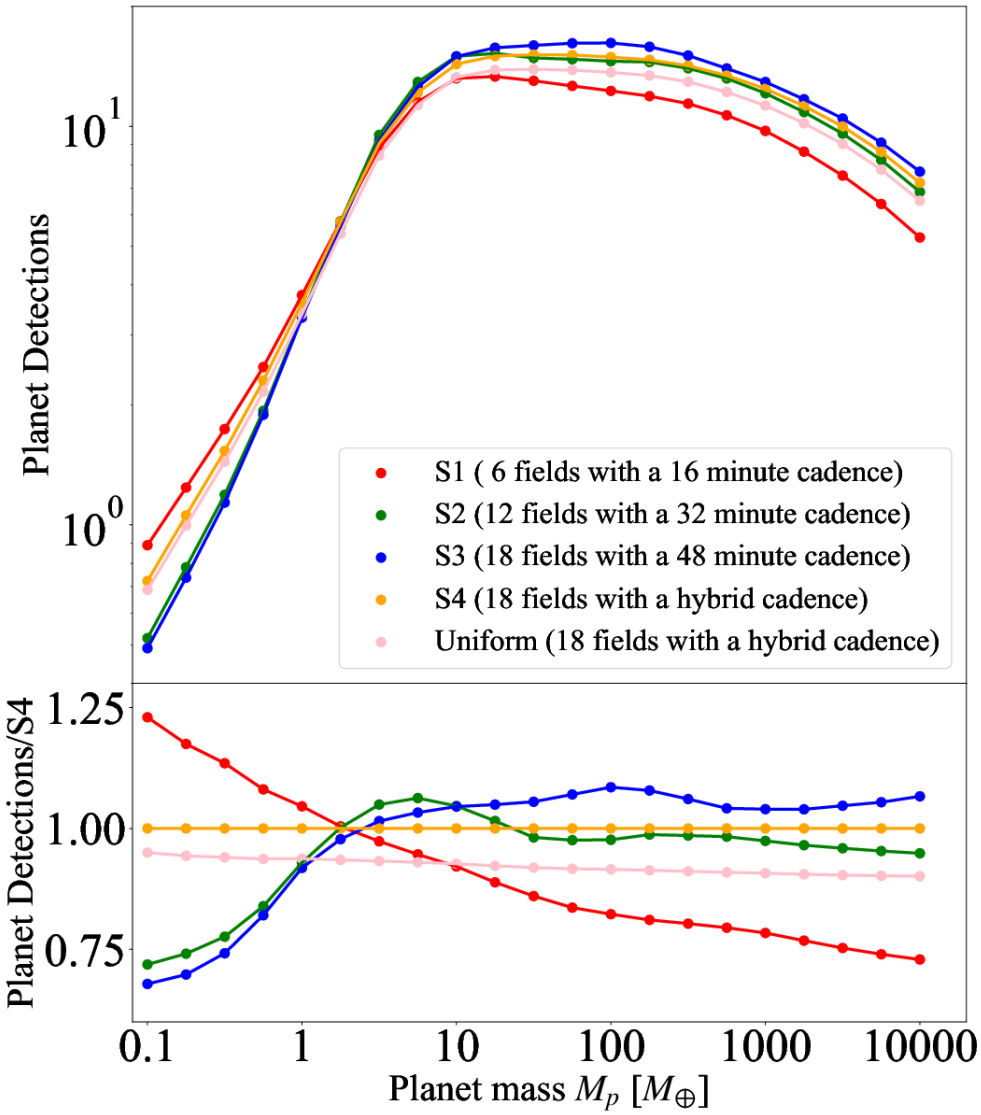

Figure 4.16: Upper panel shows the number of planet detections per dex as a function of planet mass, M_p. These plots are obtained by integrating over the semi-major axis $0.3 < a < 30$ au and over the survey area ($8.7 - 26.2$ deg^2) shown in Figure 4.15, assuming the Cassan et al. (2012) mass function as modified by Penny et al. (2019). The red, green, blue, and orange plots show the detection rate for the observation strategy S1, S2, S3, and S4 described in Section 4.5.1. The pink plot shows the detections when we conduct a spatially uniform survey described in Section 4.6.1. The lower panel shows the detections of each strategy relative to that of S4.

4.6 Discussion

4.6.1 How to decide the optimal survey strategy?

The final survey strategy will vary according to the interests of several sciences: to reveal the planet frequency around the Galactic center, to optimize the *Roman* microlenisng survey fields, to characterize the lens and planet parameters by follow-up observations. We will discuss each of these science interests in detail.

In this study, we focus on revealing the demography of cold planets down to Earth mass beyond the snow-line toward the inner Galactic bulge. In order to achieve that goal, it is required to optimize the observation strategy and to increase both the number of planets and the range of mass comparing four observation strategies, we find that it is possible to detect both low mass planets and high mass planets by an observation strategy with a hybrid observation cadence, S4. We predict that PRIME will discover up to ~ 3900 microlensing events and ~ 50 planets per year by using S4.

However another important goal of the PRIME is the optimization of the *Roman* microlensing survey fields by measuring the NIR microlenisng event rate map and $t_{\rm E}$ distributions. In order to achieve that goal, it is required to conduct a spatially uniform survey toward the inner Galactic bulge. We investigate how the planet yields change with the uniform survey strategy. The bottom panel in Figure 4.15 shows the considered field locations when we conduct a uniform survey including the Galactic center and the Galactic plane. Here, we use a hybrid observation cadence and the total number of fields is 18, which are the same as in observation strategy S4. Table 4.3 shows our estimation of the number of microlensing events and the planet detections. The result shows $\sim 6-10\%$ fewer planet discoveries depending on the planet mass and $\sim 13\%$ fewer microlensing discoveries compared to the observation strategy, S4. Therefore, the uniform survey not only allows for the detection of a relatively large number of planetary signals including low-mass planets to measure the planet frequency toward the Galactic inner bulge, but also allows for the measurement of event rates across the Galactic center and Galactic plane to help optimize *Roman*'s observation strategy..

NIR or optical follow-up observations will help to constrain the microlensing and physical parameters of planetary systems. In particular, color measurements of microlenisng events will enable us to determine $\theta_{\rm E}$, which constrains the lens mass and distance. Differences in extinction can affect field selection because they affect whether color measurements can be performed or not, but field selection by extinction in other bands is outside the scope this work.

4.6.2 Inner Galactic bulge survey by PRIME

In this study, we use KGM, which is a population synthesis model optimized for the inner Galactic bulge that includes a nuclear stellar disk model. As shown in Section 4.4.1, the luminosity function at the low mass stars is not in agreement with measurements. It is also known that there is the underestimation of extinction values in the Galactic central region which is shown in Koshimoto et al. (in prep).

Observations of the star counts, event rate, and detection efficiencies will drive improvements in Galactic models.

Although previous NIR observations towards the inner Galactic bulge such as the VVV survey have revealed detailed structure of the Galactic bar/bulge (e.g. Wegg & Gerhard, 2013; Wegg et al., 2015), the formation history and structure of our Galaxy is a long-standing challenge (Shen & Zheng, 2020). To constrain the dynamical history and evolution of Galaxy, accurate measurements of a stellar 6-D phase space distribution and stellar properties in the inner bulge region will be provided by the future time domain survey such as *Roman*, the *Japan Astrometry Satellite Mission for INfrared Exploration* (*JASMINE*; Gouda, 2012) and *GaiaNIR* (Hobbs et al., 2016, 2019). Prior to these surveys, a time domain survey with high cadence using PRIME will play an important role in providing new insights into the formation history and structure of our Galaxy. In addition to aspects of microlensing, the time domain data by the PRIME microlensing survey will provide useful information in studies of Galactic structure, through variable stars such as eclipsing binaries, pulsating RR Lyrae, and Cepheids (e.g. Pietrukowicz et al., 2020; Botan et al., 2021).

4.7 Summary

We present the expected microlensing and planet yields for four survey strategies using the PRIME instrument. In order to maximize the number of planet detections and the range of masses, we need to optimize the number of the observation fields and observation cadence, which are in a trade-off relationship. Assuming the an underlying planet population of one planet per square dex per star and the Cassan et al. (2012) mass function of planets beyond snow-line as modified by Penny et al. (2019), we predict that PRIME will discover $2300 - 4100$ microlensing events and $42 - 52$ planets per year depending on the observation strategy. In particular, the observation strategy with a hybrid observation cadence (S4) makes it possible to detect both low mass planets and high mass planets. By using S4, we predict that PRIME will discover up to ~ 3900 microlensing events and ~ 50 planets per year (~ 1.7 planets with $M_p \leq 1M_\oplus$, ~ 24 planets with mass $1M_\oplus < M_p \leq 100M_\oplus$, ~ 24 planets $100M_\oplus < M_p \leq 10000M_\oplus$). Besides, the spatially uniform survey not only allows for the detection of a relatively large number of planetary signals including low-mass planets, but also allows for the measurement of event rates across the Galactic center and Galactic plane.

Chapter 5

Summary and Conclusion

In this thesis, the following two studies were conducted to increase the number of planet samples including low-mass planets for future statistical analysis by the microlensing planets. It would be useful to clarify the overall picture of planetary distribution beyond the snow line and provide new constraints on planet formation models. It would also be useful in elucidating the dependency of planet frequency on the Galactic location in more detail.

Firstly, I report the analysis of the microlensing event OGLE-2018-BLG-1185, which was simultaneously observed from the ground telescopes and the *Spitzer* space telescope. The signal observed by *Spitzer* was small, but I could obtain space parallax likelihood distribution, which has the potential to constrain the mass and distance of the planetary system. So I conducted a Bayesian analysis with and without the space parallax constraint by *Spitzer* in order to estimate the probability distribution of the mass and distance of the planetary system. As the result of the Bayesian analysis with only ground-based constraint, the lens system is likely a super-earth with a mass of $m_p \sim 8.4 M_\oplus$ orbiting a late M-dwarf with a mass of $M_{\rm host} \sim 0.37 M_\odot$. On the other hand, the Bayesian analysis with space parallax constraint by *Spitzer* shows that the lens system is likely a super-earth with a mass of $m_p \sim 2.1 M_\oplus$ orbiting a low-mass star with a mass of $M_{\rm host} \sim 0.09 M_\odot$. Future high-resolution imaging observations with *HST* or ELT could distinguish between these two scenarios and help reveal the planetary system properties in more detail.

Secondly, I also present the results of our prediction of planet yields and the optimal survey strategy by the PRIME microlensing survey. The major goals of the PRIME microlensing survey are to measure the microlensing event rate in the inner Galactic bulge to help design the observing strategy for the exoplanet microlensing survey by *Roman* and to make a first statistical measurement of exoplanet demographics toward the inner Galactic bulge where optical observations are challenging owing to the high extinction. Here I conduct a simulation of the PRIME microlensing survey to estimate its planet yields and determine the optimal survey strategy, using a Galactic model optimized for the inner Galactic bulge. In order to maximize the number of planet detections and the range of planet mass, I compare the planet yields among four observation strategies. I predict that PRIME will detect planetary signals for $42-52$ planets ($1-2$ planets

with $M_p \leq 1M_\oplus$, $22-25$ planets with mass $1M_\oplus < M_p \leq 100M_\oplus$, $19-25$ planets $100M_\oplus < M_p \leq 10000M_\oplus$), per year depending on the chosen observation strategy. Besides, the spatially uniform survey not only allows for the detection of a relatively large number of planetary signals including low-mass planets but also allows for the measurement of event rates across the Galactic center and Galactic plane. Therefore, this strategy can achieve the two main goals of the PRIME microlensing survey together.

The first study found very low mass ratio planets and is an important sample for measuring the mass ratio function of planets on the low mass side in future statistical analyses. The second study was able to propose observational strategies that would allow the discovery of more than 10 times as many planets as conventional visible light observations, including the discovery of lower-mass planets. Both studies are expected to contribute not only to future microlensing statistical analysis, but also to future microlensing surveys with the *Roman* by understanding how to analyze space parallax and how to consider systematic errors on it, and by modifying the Galactic models.

Space parallax observations obtained from simultaneous observation between *Roman* and ground-based telescopes are expected to place limits on the masses of a great number of planets. It is the only method to measure masses of free-floating planets. Increasing the number of planetary systems for which we were able to measure mass and distance will allow us to discuss the statistical dependence of the planets on the Galactic environment and on the mass of their host stars. Therefore, it is important to understand as well as possible how to model space parallax and the effects of systematics on it.

Galactic models have played a crucial role in microlensing studies. Comparison of the predictions by the Galactic models with the result of microlensing observations has provided many insights into planetary distributions and galactic structure, such as the dependence of cold planet frequency on the Galactic components and location (Penny et al., 2016; Koshimoto et al., 2021b) and IMF (Wegg et al., 2017; Sumi et al., 2011). In addition, for planetary and single-lens events, where masses and distances cannot be measured, these physical parameters have been estimated by Bayesian estimation using the Galactic model as a prior probability. Comparison of the results of this simulation with future observations by the PRIME microlensing survey is expected to provide insight into the inner Galactic bulge that has not been obtained from previous optical microlensing surveys, thereby modifying the Galactic model. Thanks to its photometric accuracy, *Roman* is expected to detect higher-order effects (such as finite source effects and orbital parallax effects) and lens fluxes after the microlensing events are finished for many planetary events and single-lens events. However, mass estimates for some events and discussions of Galactic structure and dependencies of planet frequency on the Galactic location and host masses from *Roman* results will require comparison with Galactic models.

Appendix A

Appendix for OGLE-2018-BLG-1185b : A Low-Mass Microlensing Planet Orbiting a Low-Mass Dwarf

A.1 Constraints on the Blended Light & Discrepancy with Gaia

The blended light in this event is roughly four times brighter than the source. In principle, the blend could be the lens itself or a companion to either the lens or the source. If so, it could constrain the flux and proper motion of the lens or the proper motion of the source.

From the KMTNet images, we measure the astrometric offset between the source and the baseline object and find an offset of $0''.175$. This offset is larger than the astrometric uncertainties. Therefore, if it is a companion to the lens or source, it must be a very wide separation companion ($\sim$ 1000 au). However, the large separation also suggests that it could be an ambient star unrelated to the microlensing event.

We measure the proper motion of the baseline object based on 10 years of OGLE survey data and find $\boldsymbol{\mu}_{\rm base}({\rm RA, Dec}) = (-6.00\pm0.26, -4.25\pm0.16)$ mas yr^{-1}. Because the blend is much brighter than the source, its motion should dominate the measured $\boldsymbol{\mu}_{\rm base}$. The measured value is very consistent with typical proper motions for normal bulge stars, but not unreasonable for the proper motion of a disk star. Hence, it does not rule out the possibility that the blend is a wide-separation companion to the source or the lens, but it also shows that the blend could easily be an unrelated bulge star.

For completeness, we note that the OGLE measurement of the proper motion of the baseline object is inconsistent with the reported Gaia proper motion of the nearest Gaia source (4062756831332827136; Gaia Collaboration et al., 2016). Gaia EDR3 (Gaia Collaboration et al., 2021) reports there is a G = 20.1 mag star $0''.177$ from the OGLE coordinates for the baseline star (17:59:10.26 -27:50:06.3). The

reported proper motion of this source is $\boldsymbol{\mu}(\mathrm{RA}, \mathrm{Dec}) = (-12.173 \pm 1.247, -9.714 \pm 0.870)$ mas yr^{-1}, which is an outlier relative to the typical proper motions for stars in this field. Gaia DR2 (Gaia Collaboration et al., 2018) reports an only slightly less extreme proper motion of $\boldsymbol{\mu}(\mathrm{RA}, \mathrm{Dec}) = (-8.475 \pm 2.234, -4.039 \pm 1.985)$ mas yr^{-1}. The nature of this discrepancy is unknown, but because the Gaia proper motion is highly unusual (and the OGLE proper motion is typical), and the Gaia measurement varies significantly between DR2 and EDR3, this suggests a problem with the Gaia measurement.

References

Alard, C. 2000, Astronomy and Astrophysics, Suppl. Ser., 144

Alard, C., & Lupton, R. H. 1998, Astrophys. J., 503

Albrow, M. D., Horne, K., Bramich, D. M., et al. 2009, Mon. Not. R. astron. Soc., 397

Alcock, C., Allsman, R. A., Alves, D., et al. 1995, Astrophys. J., 454

—. 1997, Astrophys. J., 486

Awiphan, S., Kerins, E., & Robin, A. C. 2016, Mon. Not. R. astron. Soc., 456

Bachelet, E., Specht, D., Penny, M., et al. 2022, Astron. Astrophys., 664

Baraffe, I., Chabrier, G., Barman, T. S., Allard, F., & Hauschildt, P. H. 2003, Astron. Astrophys., 402

Batista, V., Beaulieu, J. P., Bennett, D. P., et al. 2015, Astrophys. J., 808

Batista, V., Gould, A., Dieters, S., et al. 2011, Astron. Astrophys., 529

Batista, V., Beaulieu, J. P., Gould, A., et al. 2014, Astrophys. J., 780

Bennett, D. P. 2010, Astrophys. J., 716

Bennett, D. P., Anderson, J., Bond, I. A., Udalski, A., & Gould, A. 2006, Astrophys. J., 647

Bennett, D. P., Anderson, J., & Gaudi, B. S. 2007, Astrophys. J., 660

Bennett, D. P., & Rhie, S. H. 1996, Astrophys. J., 472

—. 2002, Astrophys. J., 574

Bennett, D. P., Bond, I. A., Udalski, A., et al. 2008, Astrophys. J., 684

Bennett, D. P., Anderson, J., Beaulieu, J. P., et al. 2010, arXiv e-prints

Bennett, D. P., Bhattacharya, A., Anderson, J., et al. 2015, Astrophys. J., 808

Bennett, D. P., Bhattacharya, A., Beaulieu, J.-P., et al. 2020, Astron. J., 159

Bensby, T., Yee, J. C., Feltzing, S., et al. 2013, Astron. Astrophys., 549

Bensby, T., Feltzing, S., Gould, A., et al. 2017, Astron. Astrophys., 605

Bhattacharya, A., Bennett, D. P., Anderson, J., et al. 2017, Astron. J., 154

Bhattacharya, A., Beaulieu, J. P., Bennett, D. P., et al. 2018, Astron. J., 156

Bland-Hawthorn, J., & Gerhard, O. 2016, Ann. Rev. Astron. Astrophys., 54

Bond, I. A., Abe, F., Dodd, R. J., et al. 2001, Mon. Not. R. astron. Soc., 327

Bond, I. A., Udalski, A., Jaroszyński, M., et al. 2004, Astrophys. J., 606

Bond, I. A., Bennett, D. P., Sumi, T., et al. 2017, Mon. Not. R. astron. Soc., 469

Boss, A. P. 1997, Science, 276

—. 2006, Astrophys. J., 643

Botan, E., Saito, R. K., Minniti, D., et al. 2021, Mon. Not. R. astron. Soc., 504

Boyajian, T. S., van Belle, G., & von Braun, K. 2014, Astron. J., 147

Bozza, V. 2010, Mon. Not. R. astron. Soc., 408

Bozza, V., Bachelet, E., Bartolić, F., et al. 2018, Mon. Not. R. astron. Soc., 479

Bramich, D. M. 2008, Mon. Not. R. astron. Soc., 386

Bramich, D. M., Horne, K., Albrow, M. D., et al. 2013, Mon. Not. R. astron. Soc., 428

Brown, T. M., Baliber, N., Bianco, F. B., et al. 2013, Publ. Astron. Soc. Pac., 125

Burke, C. J., Christiansen, J. L., Mullally, F., et al. 2015, Astrophys. J., 809

Calchi Novati, S., Gould, A., Udalski, A., et al. 2015a, Astrophys. J., 804

Calchi Novati, S., Gould, A., Yee, J. C., et al. 2015b, Astrophys. J., 814

Calchi Novati, S., Skowron, J., Jung, Y. K., et al. 2018, Astron. J., 155

Calchi Novati, S., Suzuki, D., Udalski, A., et al. 2019, Astron. J., 157

Cardelli, J. A., Clayton, G. C., & Mathis, J. S. 1989, Astrophys. J., 345

Cassan, A. 2008, Astron. Astrophys., 491

Cassan, A., Kubas, D., Beaulieu, J. P., et al. 2012, Nature, 481

Charbonneau, D., Brown, T. M., Latham, D. W., & Mayor, M. 2000, Astrophys. J., 529

Choi, J. Y., Shin, I. G., Park, S. Y., et al. 2012, Astrophys. J., 751

Chung, S.-J., Han, C., Park, B.-G., et al. 2005, Astrophys. J., 630

Claret, A., & Bloemen, S. 2011, Astron. Astrophys., 529

Clarkson, W., Sahu, K., Anderson, J., et al. 2008, Astrophys. J., 684

Curiel, S., Ortiz-León, G. N., Mioduszewski, A. J., & Sanchez-Bermudez, J. 2022, Astron. J., 164

Dominik, M. 1999, Astron. Astrophys., 349

Dong, S., Gould, A., Udalski, A., et al. 2009, Astrophys. J., 695

Eggen, O. J., Lynden-Bell, D., & Sandage, A. R. 1962, Astrophys. J., 136

Emerson, J., & Sutherland, W. 2010, The Messenger, 139, 2

Erdl, H., & Schneider, P. 1993, Astron. Astrophys., 268, 453

Feldmeier, A., Neumayer, N., Seth, A., et al. 2014, Astron. Astrophys., 570

Fukui, A., Gould, A., Sumi, T., et al. 2015, Astrophys. J., 809

Fukui, A., Suzuki, D., Koshimoto, N., et al. 2019, Astron. J., 158

Gaia Collaboration, Prusti, T., de Bruijne, J. H. J., et al. 2016, Astron. Astrophys., 595

Gaia Collaboration, Brown, A. G. A., Vallenari, A., et al. 2018, Astron. Astrophys., 616

—. 2021, Astron. Astrophys., 649

Gaudi, B. S. 1998, Astrophys. J., 506

González Hernández, J. I., & Bonifacio, P. 2009, Astron. Astrophys., 497

Gouda, N. 2012, in Astronomical Society of the Pacific Conference Series, Vol. 458, Galactic Archaeology: Near-Field Cosmology and the Formation of the Milky Way, ed. W. Aoki, M. Ishigaki, T. Suda, T. Tsujimoto, & N. Arimoto, 417

Gould, A. 1992, Astrophys. J., 392

—. 1994, Astrophys. J., 421

—. 1995, Astrophys. J., 446

—. 2000, Astrophys. J., 542

—. 2004, Astrophys. J., 606

—. 2019, Journal of Korean Astronomical Society, 52

Gould, A., Carey, S., & Yee, J. 2014, Galactic Distribution of Planets from Spitzer Microlens Parallaxes, Spitzer Proposal ID #11006

—. 2016, Galactic Distribution of Planets Spitzer Microlens Parallaxes, Spitzer Proposal ID #13005

Gould, A., Gaudi, B. S., & Han, C. 2003, Astrophys. J., 591

Gould, A., & Loeb, A. 1992, Astrophys. J., 396

Gould, A., Yee, J., & Carey, S. 2015a, Galactic Distribution of Planets From High-Magnification Microlensing Events, Spitzer Proposal ID #12013

—. 2015b, Degeneracy Breaking for K2 Microlens Parallaxes, Spitzer Proposal ID #12015

Gould, A., Yee, J., Carey, S., & Shvartzvald, Y. 2018, The Galactic Distribution of Planets via Spitzer Microlensing Parallax, Spitzer Proposal ID #14012

Gould, A., & Yee, J. C. 2012, Astrophys. J., 755

—. 2013, Astrophys. J., 764

Gould, A., Udalski, A., An, D., et al. 2006, Astrophys. J., 644

Gould, A., Udalski, A., Monard, B., et al. 2009, Astrophys. J., 698

Gould, A., Dong, S., Gaudi, B. S., et al. 2010, Astrophys. J., 720

Gould, A., Ryu, Y.-H., Calchi Novati, S., et al. 2020, Journal of Korean Astronomical Society, 53

Gould, A., Jung, Y. K., Hwang, K.-H., et al. 2022, arXiv e-prints

Griest, K., & Hu, W. 1993, Effect of Binary Sources on the Search for Massive Astrophysical Compact Halo Objects via Microlensing: Erratum, Astrophysical Journal v.407, p.440

Griest, K., & Safizadeh, N. 1998, Astrophys. J., 500

Hardy, S. J., & Walker, M. A. 1995, Mon. Not. R. astron. Soc., 276

Hayashi, C. 1981, Progress of Theoretical Physics Supplement, 70

Hayashi, C., Nakazawa, K., & Nakagawa, Y. 1985, in Protostars and Planets II, ed. D. C. Black & M. S. Matthews, 1100–1153

Henderson, C. B., Gaudi, B. S., Han, C., et al. 2014, Astrophys. J., 794

Henry, G. W., Marcy, G. W., Butler, R. P., & Vogt, S. S. 2000, Astrophys. J., 529

Hirao, Y., Bennett, D. P., Ryu, Y.-H., et al. 2020, Astron. J., 160

Hobbs, D., Høg, E., Mora, A., et al. 2016, arXiv e-prints

Hobbs, D., Brown, A., Høg, E., et al. 2019, arXiv e-prints

Holtzman, J. A., Watson, A. M., Baum, W. A., et al. 1998, Astron. J., 115

Holz, D. E., & Wald, R. M. 1996, Astrophys. J., 471

Ida, S., & Lin, D. N. C. 2004, Astrophys. J., 604

—. 2005, Astrophys. J., 626

Johnson, S. A., Penny, M., Gaudi, B. S., et al. 2020, Astron. J., 160

Jung, Y. K., Gould, A., Zang, W., et al. 2019a, Astron. J., 157

Jung, Y. K., Gould, A., Udalski, A., et al. 2019b, Astron. J., 158

Kato, D., Nagashima, C., Nagayama, T., et al. 2007, , 59

Kennedy, G. M., & Kenyon, S. J. 2008, Astrophys. J., 673

Kenyon, S. J., & Hartmann, L. 1995, Astrophys. J. Suppl. S., 101

Kerins, E., Robin, A. C., & Marshall, D. J. 2009, Mon. Not. R. astron. Soc., 396

Kim, D. J., Kim, H. W., Hwang, K. H., et al. 2018a, Astron. J., 155

Kim, H.-W., Hwang, K.-H., Shvartzvald, Y., et al. 2018b, arXiv e-prints

Kim, S.-L., Lee, C.-U., Park, B.-G., et al. 2016, Journal of Korean Astronomical Society, 49

Konacki, M., Torres, G., Jha, S., & Sasselov, D. D. 2003, Nature, 421

Kondo, I., Sumi, T., Bennett, D. P., et al. 2019, Astron. J., 158

Kondo, I., Yee, J. C., Bennett, D. P., et al. 2021, Astron. J., 162

Koshimoto, N. 2022, nkoshimoto/genstars: A Tool for Stellar Population Synthesis toward the Galactic Bulge, v1.0.0, Zenodo

Koshimoto, N., Baba, J., & Bennett, D. P. 2021a, Astrophys. J., 917

Koshimoto, N., & Bennett, D. P. 2020, Astron. J., 160

Koshimoto, N., Bennett, D. P., Suzuki, D., & Bond, I. A. 2021b, Astrophys. J., 918

Koshimoto, N., Shvartzvald, Y., Bennett, D. P., et al. 2017, Astron. J., 154

Kubas, D., Beaulieu, J. P., Bennett, D. P., et al. 2012, Astron. Astrophys., 540

Lambrechts, M., Lega, E., Nelson, R. P., Crida, A., & Morbidelli, A. 2019, Astron. Astrophys., 630

Lee, C. H., Riffeser, A., Seitz, S., & Bender, R. 2009, Astrophys. J., 695

Lissauer, J. J. 1993, Ann. Rev. Astron. Astrophys., 31

Lissauer, J. J., & Stewart, G. R. 1993, in Protostars and Planets III, ed. E. H. Levy & J. I. Lunine, 1061

Mao, S., & Paczynski, B. 1991, Astrophys. J., 374

Mayor, M., & Queloz, D. 1995, Nature, 378

Minniti, D., Lucas, P. W., Emerson, J. P., et al. 2010, New Astronomy, 15

Mróz, P., Udalski, A., Skowron, J., et al. 2017, Nature, 548

—. 2019, Astrophys. J. Suppl. S., 244

Muraki, Y., Han, C., Bennett, D. P., et al. 2011, Astrophys. J., 741

Nataf, D. M., Gould, A., Fouqué, P., et al. 2013, Astrophys. J., 769

Navarro, M. G., Minniti, D., & Contreras-Ramos, R. 2018, Astrophys. J., 865

Navarro, M. G., Minniti, D., Pullen, J., & Ramos, R. C. 2020, Astrophys. J., 889

Nayakshin, S., Dipierro, G., & Szulágyi, J. 2019, Mon. Not. R. astron. Soc., 488

Nishiyama, S., Tamura, M., Hatano, H., et al. 2009, Astrophys. J., 696

Nucita, A. A., Licchelli, D., De Paolis, F., et al. 2018, Mon. Not. R. astron. Soc., 476

Ormel, C. W., & Klahr, H. H. 2010, Astron. Astrophys., 520

Ortolani, S., Renzini, A., Gilmozzi, R., et al. 1995, Nature, 377

Paczynski, B. 1986, Astrophys. J., 304

Penny, M. T., Gaudi, B. S., Kerins, E., et al. 2019, Astrophys. J. Suppl. S., 241

Penny, M. T., Henderson, C. B., & Clanton, C. 2016, Astrophys. J., 830

Penny, M. T., Kerins, E., Rattenbury, N., et al. 2013, Mon. Not. R. astron. Soc., 434

Pietrukowicz, P., Udalski, A., Soszyński, I., et al. 2020, Acta Astronomica, 70

Poleski, R., & Yee, J. C. 2019, Astronomy and Computing, 26

Poleski, R., Zhu, W., Christie, G. W., et al. 2016, Astrophys. J., 823

Poleski, R., Skowron, J., Mróz, P., et al. 2021, Acta Astronomica, 71

Pollack, J. B., Hubickyj, O., Bodenheimer, P., et al. 1996, Icarus, 124

Refsdal, S. 1966, Mon. Not. R. astron. Soc., 134

Reid, M. J., & Brunthaler, A. 2004, Astrophys. J., 616

Robin, A. C., Marshall, D. J., Schultheis, M., & Reylé, C. 2012, Astron. Astrophys., 538

Robin, A. C., Reylé, C., Derrière, S., & Picaud, S. 2003, Astron. Astrophys., 409

Ryu, Y. H., Yee, J. C., Udalski, A., et al. 2018, Astron. J., 155

Safronov, V. S. 1972, Evolution of the protoplanetary cloud and formation of the earth and planets.

Sahlmann, J., Lazorenko, P. F., Ségransan, D., et al. 2013, Astron. Astrophys., 556

Sako, T., Sekiguchi, T., Sasaki, M., et al. 2008, Experimental Astronomy, 22

Schechter, P. L., Mateo, M., & Saha, A. 1993, Publ. Astron. Soc. Pac., 105

Schneider, P., & Weiss, A. 1986, Astron. Astrophys., 164, 237

Searle, L., & Zinn, R. 1978, Astrophys. J., 225

Shan, Y., Yee, J. C., Udalski, A., et al. 2019, Astrophys. J., 873

Sharma, S., Bland-Hawthorn, J., Johnston, K. V., & Binney, J. 2011, Astrophys. J., 730

Sharma, S., Bland-Hawthorn, J., Binney, J., et al. 2014, Astrophys. J., 793

Shen, J., & Zheng, X.-W. 2020, Research in Astronomy and Astrophysics, 20

Shin, I. G., Udalski, A., Yee, J. C., et al. 2018, Astrophys. J., 863

Shvartzvald, Y., Bryden, G., Gould, A., et al. 2017a, Astron. J., 153

Shvartzvald, Y., Maoz, D., Udalski, A., et al. 2016, Mon. Not. R. astron. Soc., 457

Shvartzvald, Y., Yee, J. C., Calchi Novati, S., et al. 2017b, Astrophys. J., 840

Shvartzvald, Y., Calchi Novati, S., Gaudi, B. S., et al. 2018, Astrophys. J., 857

Sormani, M. C., Sanders, J. L., Fritz, T. K., et al. 2022, Mon. Not. R. astron. Soc., 512

Spergel, D., Gehrels, N., Baltay, C., et al. 2015, arXiv e-prints

Stanek, K. Z., Udalski, A., SzymaŃski, M., et al. 1997, Astrophys. J., 477

Street, R. A., Udalski, A., Calchi Novati, S., et al. 2016, Astrophys. J., 819

Sumi, T., Abe, F., Bond, I. A., et al. 2003, Astrophys. J., 591

Sumi, T., Bennett, D. P., Bond, I. A., et al. 2010, Astrophys. J., 710

Sumi, T., Kamiya, K., Bennett, D. P., et al. 2011, Nature, 473

Sumi, T., Bennett, D. P., Bond, I. A., et al. 2013, Astrophys. J., 778

Surot, F., Valenti, E., Gonzalez, O. A., et al. 2020, Astron. Astrophys., 644

Suzuki, D., Bennett, D. P., Sumi, T., et al. 2016, Astrophys. J., 833

Suzuki, D., Bennett, D. P., Ida, S., et al. 2018, Astrophys. J., 869

Terry, S. K., Barry, R. K., Bennett, D. P., et al. 2020, Astrophys. J., 889

Tsapras, Y., Street, R. A., Hundertmark, M., et al. 2019, Publ. Astron. Soc. Pac., 131

Udalski, A. 2003, Acta Astronomica, 53

Udalski, A., Szymanski, M., Kaluzny, J., et al. 1994a, Acta Astronomica, 44

Udalski, A., Szymański, M. K., & Szymański, G. 2015a, Acta Astronomica, 65

Udalski, A., Szymanski, M., Stanek, K. Z., et al. 1994b, Acta Astronomica, 44

Udalski, A., Yee, J. C., Gould, A., et al. 2015b, Astrophys. J., 799

Udalski, A., Ryu, Y. H., Sajadian, S., et al. 2018, Acta Astronomica, 68

Vandorou, A., Bennett, D. P., Beaulieu, J.-P., et al. 2020, Astron. J., 160

Verde, L., Peiris, H. V., Spergel, D. N., et al. 2003, Astrophys. J. Suppl. S., 148

Wegg, C., & Gerhard, O. 2013, Mon. Not. R. astron. Soc., 435

Wegg, C., Gerhard, O., & Portail, M. 2015, Mon. Not. R. astron. Soc., 450

—. 2017, Astrophys. J., 843

Witt, H. J., & Mao, S. 1995, Astrophys. J., 447

Woolf, N. J. 1982, Ann. Rev. Astron. Astrophys., 20

Wyrzykowski, Ł., Rynkiewicz, A. E., Skowron, J., et al. 2015, Astrophys. J. Suppl. S., 216

Wyrzykowski, Ł., Mróz, P., Rybicki, K. A., et al. 2020, Astron. Astrophys., 633

Yee, J. C., Udalski, A., Sumi, T., et al. 2009, Astrophys. J., 703

Yee, J. C., Gould, A., Beichman, C., et al. 2015, Astrophys. J., 810

Yee, J. C., Zang, W., Udalski, A., et al. 2021, Astron. J., 162

Yoo, J., DePoy, D. L., Gal-Yam, A., et al. 2004, Astrophys. J., 603

Zang, W., Penny, M. T., Zhu, W., et al. 2018, Publ. Astron. Soc. Pac., 130

Zang, W., Dong, S., Gould, A., et al. 2020a, Astrophys. J., 897

Zang, W., Shvartzvald, Y., Wang, T., et al. 2020b, Astrophys. J., 891

Zang, W., Yang, H., Han, C., et al. 2022a, Mon. Not. R. astron. Soc., 515

Zang, W., Shvartzvald, Y., Udalski, A., et al. 2022b, Mon. Not. R. astron. Soc., 514

Zang, W., Jung, Y. K., Yang, H., et al. 2022c, arXiv e-prints

Zhu, W., Udalski, A., Novati, S. C., et al. 2017, Astron. J., 154

Acknowledgments

I would like to express my sincere appreciation to Professor Takahiro Sumi for his invaluable support and guidance. He provided me with a wealth of advice and showed me the way whenever I became stuck in my research and application documents. Furthermore, he provided me with valuable experiences and opportunities, such as microlensing observation in New Zealand and participating in the installation of the PRIME telescope at the South African Astronomical Observatory (SAAO). He consistently encouraged and supported all of my endeavors. His words of encouragement served as a constant source of emotional support. My five years of research have been greatly enriched and fulfilling thanks to him.

I would like to express my appreciation to Dr. David P. Bennett, who provided me with countless invaluable suggestions about my research during our weekly meetings. His advice was extremely helpful and informative, as it encompassed a wealth of knowledge about the microlensing method and exoplanets. It is thanks to his guidance that I have been able to progress my research to the point of publishing three papers. It was a great pleasure to get your advice for my research and discuss with him in person at some conferences.

I would like to express my heartfelt gratitude to Dr. Jennifer C. Yee, who provided me with invaluable assistance in drafting the paper on the microlensing event with *Spitzer* data, and with whom I had numerous engaging discussions. I have respected you as a person and researcher since we met in person at the Microlensing Workshop in NY in 2019 and worked on a project together. I am also thankful for her affording me the great opportunity to make a decision until the very end.

A special gratitude I give to Professor Emeritus, Hiroshi Shibai for his thoughtful guidance. I still try to discipline myself by his teachings in terms of research and non-research.

A special gratitude I give to Associate Professor, Kento Masuda, for his constructive suggestions on my research. He was very insightful and I learned a lot from him in my papers and application documents. I also appreciate the many incisive points he made as a member of the Ph.D. dissertation review committee.

A special gratitude I give to Associate Professor, Daisuke Suzuki, for continuous support and thoughtful guidance throughout my research. He took any of my opinions sincerely and worked with me to come up with a solution.

I am also grateful to secretaries in Osaka University, Ayae Yamamoto, Hiroko Joe, and Kumiko Mori for their support. Thanks to them, I was able to go on overseas visits smoothly and concentrate on my research.

I would like to thank Professor Hironori Matsumoto, Professor Sho Sasaki, and Associate Professor Yoshiyuki Inoue, who are the members of the Ph.D. dissertation review committee for their sharp and appropriate advice. They helped me to improve my doctoral dissertation.

I am grateful to the following organizations for their financial support during my research life. I appreciate the financial support from the Japan Society for the Promotion of Science (JSPS) over the past three years. A special thank you to the Hayakawa funding for their support of my trip to SAAO to install PRIME telescope. I also thank SUPER-IRNET for their support of my trip to SAAO to install PRIME-Cam. Thanks to these supports, I was able to have many experiences in the course of my research, including international conferences and the installation of PRIME telescope and PRIME-Cam.

I would like to express my appreciation to all members of MOA and PRIME. A special gratitude I give to Naoki Koshimoto, who gave me a lot of advice and discussions. I learned from him how to conduct an discussion. He helped me many times to clarify my thoughts when I was stuck in my research. I would like to express my appreciation to Masayuki Nagakane, who taught me how to start a research and how to proceed in a concrete way. He also showed me all kinds of things in detail during my first observation in NZ. I would like to express my appreciation to Yuki Hirao, who gave me advice on presenting at conferences. I would like to express my appreciation to Yuki K. Satoh, who taught me a lot about astrobiology and galaxies as well as exoplanet science. I would like to express my appreciation to Rintaro Kirikawa, whose attitude towards his research and projects made me want to do my best too.

I am also grateful to Nicholas J. Rattenbury, who correct my English many times and gave me useful comments for our paper. I am also grateful to Ian Bond for great support for my research and for the many discussions on the PRIME pipeline and MOA photometry.

A special gratitude I give to Stela Ishitani Silva, Aikaterini Vandorou, Aparna Bhattacharya, Clément Ranc, Greg Olmschenk and Sean K. Terry. Although, it's been a long time since I've attended an international conference face-to-face and I was feeling nervous, they helped me to make the conferences very enjoyable and productive at Microelnsing Conference in Paris and at Exoplanets IV in Las Vegas in 2022.

I would also like to thank all those who supported me during my total three months observations at Mt.John Observatory in NZ. I am also grateful to Paul J. Tristriam, who worked with me to solve problems with my observations. I am also grateful to Nigel Frost for his support in NZ. I am also grateful to members of Dark Sky Project, Mei-san, Aki-san, Keicy, Keke-san, and Daniel. They helped me enjoy Mt. John to the fullest and made me come to love with NZ.

I would also like to thank all those who supported me during my total two and a half months stay in SAAO. I am also grateful to members of Nishimura factory, Mr. Seki, Mr. Uemura, Ms. Kajitani and Dr. Otani, and Mr. Okumura, who also assisted us in our daily life at SAAO, in addition to assembling the PRIME telescope. I am also grateful to NASA members for staying hard exciting two weeks with us. I am grateful to Alexander Kutyrev, who answered a lot of my

simple questions. He shared a wealth of knowledge about near-infrared detectors and near-infrared observations with us. I am also grateful to Gregory Mosby, who had so many discussions to create a line-fitting pipeline for PRIME together. He imparted a lot of knowledge to me, having no knowledge of near-infrared detectors at all. I am also grateful to Eric Lyness, who continued to be sincere when I had problems with the Goddard software. I am also grateful to Joseph Durbak, who was always diligent and polite when I asked him about the detector and software, no matter how busy he was. I am also grateful to accommodation staffs in SAAO, who supported our lives and cooked our meals.

I would also like to thank all members in our laboratory who helped me on a daily basis. I am also grateful to Rikako Ono and Haruno Suematsu, who were my strongest allies and were always there for me. I am also grateful to Shohei Goda, Masayuki Ido, Morito Saiki, Takahiro Tsuboi, Yuzuru Tanaka, Hikaru Shoji, Tsubasa Yamawaki, Soichi Kadono, Taiga Toda, Hibiki Yama, Arisa Okamura, Ryusei Hamada, and Kansuke Yamashita. Thanks to them, I was able to relax and enjoy my research life. They were all very interesting people, as I would expect from Osaka.

Finally, I would like to show my greatest appreciation to my many friends and to my dear family. Thank them for all the positive things they say at all times. Without them, I certainly could not have submitted this doctoral dissertation. Once again, thank you so much to all who have helped me during my research.